AN EXPERIMENTAL STUDY OF TURBULENT BOUNDARY LAYERS OVER TRUNCATED CONE ROUGHNESS

by
Kristofer Michal Womack

A dissertation submitted to Johns Hopkins University in conformity with the requirements for the degree of Doctor of Philosophy.

Baltimore, Maryland
February 2021

Abstract

Fluid dynamic flow prediction remains a challenge relevant to many engineering applications. The truncated cone roughness shape, in particular, models both geophysical topography for wind and weather prediction and barnacles for ship propulsion optimization. To investigate flow in these important applications, an experimental study was conducted on rough-wall, turbulent boundary layer flow with differently arranged truncated cone roughness elements. Varying planform densities of roughness elements in regular square staggered patterns and in random arrangements were investigated. Velocity statistics were measured via two-component laser Doppler velocimetry and stereo particle image velocimetry. In order to accurately determine wall-shear stress from velocity profile measurements, the total shear stress balance was analyzed and reformulated using several well-established semi-empirical relations. Application of the proposed analysis to turbulent smooth- and rough-wall experimental data show friction velocity is determined with accuracy comparable to force balances (about $1 - 4\%$). Recent morphometric and statistical drag prediction methods

ABSTRACT

were evaluated against experimentally determined roughness length, which is related to surface drag. Observed differences between regular and random surface flow parameters were due to the presence of secondary flows which manifest as high momentum pathways (HMPs) and low momentum pathways (LMPs) in the streamwise velocity. Contrary to expectation, these secondary flows were present over the random surfaces and not present over the regular surfaces. Previously identified roughness topography thought to generate and sustain HMPs and LMPs were not present. It is suggested that, once initiated, flow heterogeneity in the form of alternating high and low momentum pathways may be sufficient for secondary flow prolongation over homogeneous roughness. Due to the secondary flows, local turbulent boundary layer profiles did not scale with local wall shear stress but appeared to scale with local turbulent shear stress above the roughness canopy. Additionally, quadrant analysis showed distinct changes in the populations of ejection and sweep events in HMPs and LMPs.

Advisors: Charles Meneveau and Michael P. Schultz

Secondary Reader: Dennice F. Gayme

Acknowledgments

I am deeply grateful to numerous people and organizations who have given me the opportunity to study these past several years. This dissertation would not have been possible without their support.

I thank Bethany, my wife, for sacrificing her time to take care of our daughter, Eleanor, for her support in the daily things that freed me to give more to this effort, and for her support for my decision to pursue a doctoral degree even though it promised sacrifices for our family.

I thank Mike Schultz and Charles Meneveau, my advisors. They have been the best mentors, teachers, and professionals. They gave me the opportunity to study at Johns Hopkins University and to research at the United States Naval Academy. Then, they supported me through the whole process, despite the challenges, delays, and mistakes. It has been a privilege to work with them.

I thank several organizations for comprehensive support. The United States Department of Defense and Office of Naval Research provided tuition and stipend funding through the Nation Defense Science and Engineering Graduate

ACKNOWLEDGMENTS

Fellowship program (2015-2018). The United States Naval Academy provided facilities, machine shop, hydromechanics laboratory, computing, and library support, and Johns Hopkins University provided computing resources and additional tuition and stipend funding. The Office of Naval Research provided additional funding for my advisor, Professor Schultz, and the experimental effort. The National Science Foundation (CBET-1738918) provided partial support for my advisor, Professor Meneveau. The United States Naval Academy and Johns Hopkins University enhanced this work with an outstanding community committed to academic excellence.

I thank Julio Barros and Elizabeth Murphy, my lab mates for teaching me how to use the equipment and guiding me through the initial difficulties of starting doctoral level research in an unfamiliar field. I thank Ralph Volino for insightful discussions, stereo PIV data and analysis, and help editing papers. I thank the United States Naval Academy Hydromechanics Laboratory and Machine Shop staffs, especially Mike Stanbro, Dan Rhodes, Brandon Stanley and Nick Hlavaty, for their work building the test plates and tunnel modifications.

I thank Dennice Gayme, my reader. She has engaged in many helpful discussion over the years by listening intently during research group updates, thinking critically about the challenges, and providing new insights. I thank my professors, especially Tamer Zaki, for patient teaching and encouragement.

I thank my friends at Johns Hopkins, Jasim Sadique, Xiang Yang, Adam

ACKNOWLEDGMENTS

Sierakowski, Dan Willen, Perry Johnson, Joel Bretheim, Carl Shapiro, Louis Martinez, José Elsas, and Aditya Aiyer for their teaching, help, encouragement, and assistance. I thank my classmates, Nick Doeller, Subhra Koley, and Karuna Agarwal for their help and friendship through the coursework.

I thank my friends, Joshua Young, Billy Hurley, and Joey Tomassoni, for their encouragement, advise, and support.

I thank my family, Harry and Angel, my parents, and Dustyn, Trayce, and Jonathan, my brothers and sister, for motivation, encouragement, and support. I thank my favorite cousin, Tailor, for always listening, helping, and encouraging.

Lastly, I thank God for the opportunity and ability to complete this work and for providing for me in every way.

Dedication

To my wife, Bethany, who is most worthy of my love.

To my daughter, Eleanor, who brightens my life.

Contents

Abstract **ii**

Acknowledgments **iv**

List of Tables **xii**

List of Figures **xiii**

1 Introduction **1**

2 Comprehensive shear stress analysis of turbulent boundary layer profiles **6**

2.1 Introduction 6

2.2 Method 12

2.2.1 Rescaled mean momentum balance equation 13

2.2.1.1 Determining the friction velocity gradient 17

2.2.1.2 Determining the velocity gradient profile 24

2.2.1.3 Test on DNS data from smooth-wall turbulent boundary layers 29
2.2.1.4 Test on experimental data from smooth-wall turbulent boundary layers 31
2.2.1.5 Test on experimental data from rough-wall boundary layers 32
2.2.2 Determining roughness length and zero-plane displacement 33
2.2.3 Practical implementation: iterative method 35
2.3 Applications to various experimental data sets 37
2.3.1 Boundary layers over rough sand-grain surfaces 37
2.3.2 Boundary layers over smooth walls 43
2.3.3 Boundary layers over arrays of wall attached staggered cubes 44
2.3.4 Boundary layers over arrays of LEGO blocks 51
2.3.5 Friction velocity sensitivity 56
2.4 Summary 59
2.4.1 Key assumptions 59
2.4.2 Results and comparisons with other methods 60
2.5 Conclusions 62

3 Turbulent boundary layers over truncated cone roughness 64

3.1 Introduction 64

3.2 Experimental details 71
3.2.1 Facility 71
3.2.2 Roughness morphology 72
3.2.3 Laser Doppler velocimetry measurements 76
3.2.4 Stereoscopic particle image velocimetry measurements . . 78
3.3 Spatial-averaged results 80
3.3.1 Spatial-averaged boundary layer profile results 80
3.3.2 Differences in spatial-averaged staggered and random surface profiles 93
3.4 Secondary flow structures and their characteristics 97
3.4.1 Evidence of secondary flow structures 98
3.4.2 Momentum pathway surface roughness correlations 107
3.4.3 Momentum pathway sustainment 115
3.4.4 Momentum pathway local boundary layer parameters and statistics 117
3.4.5 Momentum pathway Reynolds shear stress quadrant analysis 124
3.5 Conclusions 129

4 Conclusions **134**

A Adaption of the Macdonald et al. model to truncated cones **136**

CONTENTS

Vita **157**

List of Tables

2.1 Friction velocity data for experimental sand-grain flow profiles . 43
2.2 Friction velocity data for experimental smooth-wall flow profiles . 45
2.3 Friction velocity data for experimental staggered cube flow profiles 47
2.4 Friction velocity data for experimental staggered cube flow profiles assuming FPG 51
2.5 Friction velocity data for experimental LEGO block flow profiles . 55
2.6 Parameter variations for univariate and trivariate sensitivity analysis 57

3.1 Test surface statistics 75
3.2 Experimental profile parameters for spatial-averaged LDV measurements 83

List of Figures

2.1 Skin friction law 22
2.2 Scaled boundary layer profiles developing over increasing fetch . 26
2.3 Equation (2.3) for DNS smooth-wall ZPG flow 30
2.4 Equation (2.3) for experimental smooth-wall ZPG flow 31
2.5 Equation (2.3) for experimental sand-grain surface ZPG flow . . . 34
2.6 Flowchart of the iterative process for solving u_τ, y_0, and d 36
2.7 Comparison of data and fits for experimental sand-grain flow profiles 39
2.8 RMS errors for fits to experimental sand-grain flow profiles . . . 40
2.9 Comparison of data and fits for experimental smooth-wall flow profiles 44
2.10 Comparison of data and fits for experimental staggered cube flow profiles 46
2.11 RMS errors for fits to experimental staggered cube flow profiles . 47
2.12 Comparison of data and fits for experimental staggered cube flow profiles assuming FPG 50
2.13 Comparison of data and fits for experimental LEGO block flow profiles 53
2.14 RMS errors for fits to experimental LEGO block flow profiles . . . 54
2.15 Scatter plots showing u_τ, y_0, and d trivariate sensitivity 58
2.16 Bar plots showing univariate sensitivity of u_τ 58
2.17 Friction velocities from multiple total shear stress approaches . . 61

3.1 Test surfaces 73
3.2 Planform and frontal density illustration 76
3.3 Truncated cone dimensions 77
3.4 Profile locations over the staggered surface repeating unit 78
3.5 Profile locations over the random surfaces 79
3.6 c_f as a function of θ/y_0 for all surfaces 84
3.7 Mean streamwise velocity profiles in inner scaling 85

3.8 Turbulent shear stress profiles in inner scaling 86
3.9 Normalized roughness length, y_0/k, as a function of λ_p 88
3.10 Normalized zero-plane displacement, d/k, as a function of λ_p . . . 93
3.11 Outer-normalized S78 and R78 local profiles 94
3.12 Staggered and random surface profiles in inner-normalized mean streamwise velocity defect form 95
3.13 Plots of wake strength, Π, as a function of planform density, λ_p, and roughness function, ΔU^+ 96
3.14 Mean streamwise velocity contours on a smooth wall surface . . . 98
3.15 Mean streamwise velocity contour over all random surfaces . . . 99
3.16 Mean streamwise velocity spatial standard deviation for all surfaces 101
3.17 R78 mean streamwise velocity contours at three streamwise locations 102
3.18 R78 mean streamwise velocity and Reynolds shear stress contours from three independent test runs 103
3.19 Stereo PIV data plots 106
3.20 Correlation coefficients between streamwise velocity and topography 112
3.21 Random surface topographical correlations with HMPs and LMPs (continued figure) 113
3.21 Random surface topographical correlations with HMPs and LMPs (continued figure) 114
3.22 Random surfaces local friction velocity correlations with HMPs and LMPs 119
3.23 Profile data for all local R78 profiles inner-normalized with local wall shear stress 121
3.24 Profile data for all local R78 profiles inner-normalized with local near-wall turbulent shear stress 122
3.25 Contour plots of Reynolds shear stress quadrant data from LDV measurements 127

Chapter 1

Introduction

The fluid dynamic boundary layer is the thin volume of fluid that is directly affected by a solid surface. Boundary layers occur frequently in both nature and engineering, however there are still many aspects of boundary layer behavior that are not well understood. Most boundary layers are turbulent, meaning that they are generally an unstable mix of multi-scale vortices or "eddies." The turbulent nature of many fluid flows is what gives fluid dynamics its immense complexity and why so many flow characteristics are not yet completely understood.

In addition to being turbulent, most boundary layers develop over rough surfaces as opposed to surfaces with negligible imperfections. Rough-wall turbulent boundary layers have been studied extensively for nearly the last century[57;17;71;36], however the flow over many surfaces remains untested. The

central difficulty is the boundlessly varying surface morphologies which exist in nature and engineering applications. Though arduous, advancements in fluid dynamic experiments and modeling have steadily provided increased understanding and continue to further engineering capabilities[13].

One important roughness shape that has seen only limited study in the literature is the truncated cone, an idealized shape that occurs frequently in both nature and engineering applications. In geophysical applications, truncated cones can represent an idealized hill or low-mountain roughness element. The surface-atmosphere interaction is an important aspect in many weather models[6]. Also, demand for wind energy has significantly accelerated in recent decades. Many wind farm power models require inflow information to predict power outputs or compute optimal configurations[82]. The data gained from truncated cone research may prove useful to increasingly complex weather and wind energy models.

Truncated cones are also an idealized barnacle shape. Barnacle biofouling is of great interest to the shipping industry and United States Navy due to the increased hydrodynamic drag and increased cost. In one study, Schultz et al.[75] estimated that the excess cost for one DDG-51 class (mid-sized) ship was $1 million per year. In 2020, the United States Navy had 67 active DDG-51 ships in this class and a total of 299 ships[70]. It is reasonable to estimate that the additional total cost was likely between $100-300 million per year, and

Schultz et al.[75] state that the primary additional cost was associated with fuel consumption increases due to fouling. Most efforts to minimize this cost have attempted to prevent or slow the growth of biofouling organisms. While this has helped, it has not eliminated the biofouling problem.

To mitigate the additional fuel costs, the Naval Ships' Technical Manual[54] instructs that hull cleaning shall occur when over 20% of the hull is covered in calcareous (barnacle) fouling. While barnacle fouling has been studied since at least the 1930s by Kempf[36], the 20% coverage requirement seemed to be obsolete given more recent data. Hall et al.[27], Macdonald et al.[44], Hagishima et al.[26], Leonardi and Castro[41], and Yang et al.[100] all reported data which indicates that cube roughness shows a peak in drag between 15-20% coverage density. These data then suggest that hull cleaning was occurring at the peak and that hull cleaning procedures could be based on other cost factors since the highest fuel cost penalties were already imposed.

These studies, however, focused on cube roughness surfaces. Kempf[36] conducted a study with varying densities of real barnacles and found that peak drag occurred at about 75% coverage. However, 94% of the peak value was attained by 25% coverage since most of the increase in drag was in the first 25% coverage. More recently, Sadique[69] provided a computational fluid dynamic study with staggered and aligned truncated cones. The data suggested a peak in drag around 35%, however the study only provided data at five densities (5,

10, 20, 35, and 79%) giving low confidence to the density of the peak drag.

Analytical and statistical drag models present another opportunity for barnacle drag prediction. Analytical models such as Macdonald et al.[44] and Yang et al.[100] accurately model the cube data. However, they are sensitive to the coefficient of drag which is not well known for barnacles or truncated cones. Schultz et al.[76] reported a coefficient on drag of 0.52 for a real barnacle, and Sadique[69] (see table 3.2) reported 0.21 for a modeled barnacle differing by a factor of more than 2 from Schultz et al.[76]. Additionally, these analytical models were optimized for regular cube roughness and were not designed and tested for the irregular arrangements in which barnacles usually grow. Lastly, statistical drag models have progressed over the last few decades and may perform more accurately on irregular surfaces. Chung et al.[13] provides a recent review of drag prediction models but concludes that an equation that predicts drag in all cases remains elusive. Their study highlighted the need for additional data to develop new models or test and refine existing ones. These limitations together suggest that it is unwise to fully trust the results from existing analytical and statistical models without additional data.

The work presented here provides an experimental truncated cone roughness data set which informs drag models with more realistic roughness shapes and arrangements for atmospheric and ship-hull boundary layer prediction. In order to accomplish this, sixteen test plates were designed with truncated cones

varying in density and arrangement from 10 to 78%. Truncated cones on eight test plates were arranged in a square staggered pattern, and the same eight densities were arranged in a random distribution on the remaining test plates. Turbulent boundary layer flow developing over these surfaces was measured with laser Doppler velocimetry and stereo particle image velocimetry systems.

The dissertation is organized into three remaining chapters. Chapter 2 presents a novel technique for more accurately analyzing rough-wall turbulent boundary layers which is utilized in the following chapter. Then, chapter 3 presents the results of the truncated cone experiments. Finally, chapter 4 presents conclusions and recommendations for following studies.

Chapter 2

Comprehensive shear stress analysis of turbulent boundary layer profiles

2.1 Introduction

The most important physical quantity characterizing wall-bounded turbulent boundary layers is the skin friction drag. The topic of experimental determination of skin friction drag is closely linked to fundamental understanding of the total momentum balance in turbulent boundary layers. Much has been learned over a long history of research on these related topics and reviews of various skin friction determination techniques can be found in Winter[95], Haritonidis[28],

Klewicki et al.[37], and Walker[89].

The most widely used analysis techniques to determine skin friction are based on measurements of the streamwise mean velocity profile at various heights above the surface. The data are then compared to the assumed log-law equation[15] in order to estimate the friction velocity, roughness function, and zero-plane displacement. The log-law equation reads

$$U^+ \equiv \frac{U}{u_\tau} = \frac{1}{\kappa} \ln \left[\frac{(y-d)u_\tau}{\nu} \right] + A - \Delta U^+. \tag{2.1}$$

In this equation U is the mean streamwise velocity, κ is the Kármán constant, and A is the log-law intercept for smooth walls. The unknown scaling parameter is the friction velocity, u_τ, and the $+$ superscript indicates normalization by u_τ. Here, d is a shift in the effective origin of the log-law due to the roughness, and the roughness function, ΔU^+, models a change in the mean flow velocity due to the roughness. When roughness is present, both d and ΔU^+ are non-zero and unknown as well. Case-by-case comparisons of these parameters remain an important way to describe differences among turbulent boundary layers. However, these parameters are difficult to determine accurately based on a single mean velocity profile due to the number of unknowns and possible dependencies between them.

Clauser was the first to use equation (2.1) to determine these parameters by

fitting mean velocity profiles to the equation. He developed a graphical log-law fitting method for determining friction velocity and roughness function known as the Clauser chart method[15]. Perry and Joubert[59] extended this method for rough walls to include the shift in effective origin in what Perry and Li[60] later termed the modified Clauser chart method.

There are clear shortcomings to these log-law fitting approaches. Perry and Joubert[59] and Castro[9] note that many different combinations of friction velocity, roughness function, and effective origin can give equally good fits to experimental data. Also, Wei et al.[92] have shown that specific assumptions about the value of the Kármán constant and the fitting procedure used can often mask subtle dependencies on other variables such as the Reynolds number, Re. Nonetheless, many researchers still use fitting procedures due to the lack of a better alternative. To address the shortcomings of the fitting procedures, many researchers measure additional quantities in an attempt to reduce the number of unknowns for fitting.

The most important unknown is the friction velocity, u_τ, because it relates directly to the surface drag. Direct measurement of wall shear stress, which is related to friction velocity by $u_\tau \equiv \sqrt{\tau_w/\rho}$, is possible using a force balance among other methods. Sensitive floating element force balances have been successfully employed in many experiments such as Krogstad and Efros[40], Baars et al.[4], and Ferreira et al.[19]. However, these balances are usually expensive, normally

require careful surface preparation and alignment, and typically only measure wall shear stress at a single downstream location in the experimental facility. These significant challenges limit the wide-spread experimental application of force balances, even at laboratories where they are available.

Friction velocity determination methods that require only fluid velocity measurements are necessary since direct, force balance measurement is not always feasible. Additionally, fluid velocity measurement methods can serve as cross verification of direct measurement results. The traditional total shear stress method assumes that the total shear stress near the wall is composed of only two significant components: the viscous shear stress and Reynolds shear stress. This method was in common use by the mid-1980's and is still used presently[42;74;89]. However, discrepancies between expected and measured results were noted early on. Initial investigations by Li et al.[42] and Raupach et al.[65] concluded that discrepancies were due to measurement limitations inherent in the hot-wire equipment utilized. Later studies by Cheng and Castro[12] and Cheng et al.[11], which compared direct measurement methods and laser Doppler velocimetry flow measurements, reasonably attributed the discrepancy to unmeasured fluid dynamic effects.

Several recent studies have attempted to quantify these previously unaccounted fluid dynamic effects including Fukagata et al.[24], Mehdi and White[47], Mehdi et al.[48], and Volino and Schultz[88]. These shear stress methods attempt

to quantify additional measurable shear stress terms by using the Reynolds-averaged, streamwise momentum equation for two-dimensional flows. These methods require additional fluid velocity measurements or assumptions for unknown or uncertain information. For example, Mehdi and White[47] and Mehdi et al.[48] are able to calculate friction velocity based on the measured streamwise mean velocity and Reynolds shear stress profiles. However, they find that the method is sensitive to unknown and noisy data near the wall. They overcome this limitation by assuming a shape for the total shear stress profile and by smoothing the measured data. Volino and Schultz[88] derive a transformed version of the Reynolds-averaged, streamwise momentum equation for two-dimensional flows. They are then able to calculate friction velocity based on the measured streamwise velocity and Reynolds shear stress profiles. However, multiple streamwise profile locations are required because some significant terms are affected by streamwise gradients.

The complexity of these methods, the required high and often impractical experimental accuracy, and the lack of required data pose a barrier for common adoption. Left with a difficult problem, recent studies by Reynolds and Castro[67] and Placidi and Ganapathisubramani[61] have concluded that traditional total shear stress methods require an evidence-based adjustment of approximately 12% in order to match direct (force balance) wall stress measurements.

The present study aims to develop a more complete understanding of each

of the terms in the momentum equation and to approximate missing terms using well-established semi-empirical relations and non-dimensionalizations. These insights enable the development of a more comprehensive shear stress method that improves the agreement with direct wall stress measurements and circumvents the need for empirical *a posteriori* adjustments to the wall stress calculated with fluid velocity and shear stress profile measurements. The proposed comprehensive shear stress method requires no more data than traditional total shear stress methods and aims to describe the turbulent shear stress throughout much of the boundary layer. Increased utility with less data is accomplished by extending the Volino and Schultz[88] equation and supplementing it with semi-empirically justified assumptions about the streamwise development of a boundary layer.

It is shown that coupling this new friction velocity equation with log-law fitting provides an accurate method for determining friction velocity in nominally zero pressure gradient boundary layers. The accuracy of the method is demonstrated on several recent data sets including Cheng and Castro[12] which is often cited for demonstrating this discrepancy between traditional total shear stress methods and direct measurements. The proposed new method reasonably accounts for the discrepancy by demonstrating the effect of a small favorable pressure gradient caused by a fixed tunnel cross-section on turbulent shear stress and avoids the need for empirical adjustment of experimental data. The

improved accuracy in friction velocity determination demonstrates the importance of including as many of the terms affecting the mean momentum balance as possible.

Section 2.2 describes the reformulated momentum balance in developing boundary layers, written in inner variables, and tests the accuracy of the proposed form using various shear stress data sets. Also, an iterative method to combine this analysis with the log-law equation for the mean velocity is described. The comprehensive shear stress method is then applied to several recent experimental data sets in section 2.3 to demonstrate the performance of the proposed method of analysis, leading to more accurate friction velocity determination. Results are summarized in section 2.4, and conclusions regarding the proposed method are presented in section 2.5.

2.2 Method

The present approach is based on two equations which can be fit to the mean streamwise velocity profile and the Reynolds shear stress profile in zero or nominally zero pressure gradients. The two equations each have dependencies on friction velocity and roughness function which allow iterative convergence to a unique result for friction velocity, roughness function, and zero-plane displacement.

The first equation is an extension to the Volino and Schultz [88] equation which allows calculation of friction velocity. Section 2.2.1 presents the derivation of this extended Volino and Schultz equation which calculates friction velocity, u_τ, maintains the advantages of the original method, and expands its applicability by adding dispersive shear stress and allowing calculation of streamwise gradients from a single two-component profile. The second equation is the log-law equation for the mean velocity. Section 2.2.2 describes the fitting of the log-law equation. Roughness function and zero-plane displacement are calculated by a two-parameter fit of the overlap region of the boundary layer mean velocity profile. Section 2.2.3 summarizes the comprehensive shear stress method and the iterative approach combining both equations.

2.2.1 Rescaled mean momentum balance equation

For steady, two-dimensional flow with constant properties, the integral form of the Reynolds-averaged and spatially-averaged streamwise momentum

equation is

$$\frac{\tau_w}{\rho} - \left(\nu\frac{\partial\langle U\rangle}{\partial y} - \langle\overline{u'v'}\rangle - \langle\tilde{u}\tilde{v}\rangle\right) + \frac{1}{\rho}\frac{d\langle P\rangle}{dx}y - \langle U\rangle\int_0^y \frac{\partial\langle U\rangle}{\partial x}dy + 2\int_0^y \langle U\rangle\frac{\partial\langle U\rangle}{\partial x}dy + \int_0^y \frac{\partial\left\langle\overline{u'^2}\right\rangle}{\partial x}dy = 0, \quad (2.2)$$

when integrated from the wall to any arbitrary height, y. Here, x and y are the streamwise and wall-normal directions, and U and V are the time-averaged streamwise and wall-normal velocities. τ_w is the wall shear stress, ρ is the density, ν is the kinematic viscosity, P is the pressure, $-\overline{u'v'}$ is the Reynolds shear stress, and $\overline{u'^2}$ is the streamwise Reynolds normal stress. The overbars denote time averaging, and the angle brackets denote spatial averaging. The primes denote time fluctuating components from the Reynolds decomposition, $u = U + u'$, and tildes denote spatially fluctuating components from a further spatial average decomposition, $U = \langle U\rangle + \tilde{u}$.

For boundary layer profiles, spatial averaging of multiple data points at the same wall-normal distance, y, can be advantageous. The most common context for such averaging is particle image velocimetry where time-averaged statistics from a two-dimensional vector field may be further spatially averaged into a single better converged one-dimensional profile. Examples of this approach can be found in Nakagawa and Hanratty[53], Wu and Christensen[97], and Placidi and Ganapathisubramani[61]. Additionally, spatial averaging may be important for

hot-wire or laser Doppler velocitmetry measurements as well. Cheng and Castro [12] and Cheng et al. [11] studied several urban-like roughnesses. They measured several cross-wire anemometry profiles over a single repeating unit for each surface. The spatially-averaged profile was then a more representative profile which could be considered homogeneous on scales larger than the repeating unit itself for each surface.

Equation (2.2) can be used to calculate τ_w directly as was done successfully by Brzek et al. [8] in a zero pressure gradient (ZPG) boundary layer. However, Volino and Schultz [88] noted that its accuracy depends largely on the ability to accurately measure the streamwise gradient terms. This is difficult given experimental constraints and uncertainties in most circumstances. To mitigate this challenge, Volino and Schultz [88] transformed the equation to wall coordinates in the wall-normal, y-direction, only and separate the streamwise gradient terms into various groups. They use the standard definitions for non-dimensional terms

$$y^+ = \frac{yu_\tau}{\nu}, U^+ = \frac{U}{u_\tau}, \overline{u'v'}^+ = \frac{\overline{u'v'}}{u_\tau^2}, \overline{u'^2}^+ = \frac{\overline{u'^2}}{u_\tau^2}, \frac{1}{\rho}\frac{dP}{dx} = -\frac{KU_e^3}{\nu},$$

$$K = \frac{\nu}{U_e^2}\frac{dU_e}{dx}, \text{ and } \frac{c_f}{2} = \left(\frac{u_\tau}{U_e}\right)^2,$$

where U_e is the freestream velocity, K is the acceleration parameter, and c_f is the skin friction. Equation (2.2) can be rewritten in the transformed variables

as follows:

$$
\begin{aligned}
-\left\langle \overline{u'v'} \right\rangle^{+} - \left\langle \tilde{u}\tilde{v} \right\rangle^{+} = \\
1 - \underbrace{\frac{\partial \langle U \rangle^{+}}{\partial y^{+}}}_{I} - \underbrace{\frac{K}{(c_f/2)^{3/2}} y^{+}}_{II} \\
+ \underbrace{\left[\frac{K}{\sqrt{c_f/2}} + \frac{\nu}{U_e\,(c_f/2)} \frac{d\sqrt{c_f/2}}{dx} \right] \int_0^{y^{+}} \langle U \rangle^{+2} dy^{+}}_{III} \\
+ \underbrace{\frac{\nu}{U_e \sqrt{c_f/2}} \left(2 \int_0^{y^{+}} \langle U \rangle^{+} \frac{\partial \langle U \rangle^{+}}{\partial x} dy^{+} - \langle U \rangle^{+} \int_0^{y^{+}} \frac{\partial \langle U \rangle^{+}}{\partial x} dy^{+} \right)}_{IV} \\
+ \underbrace{\left[\frac{K}{\sqrt{c_f/2}} + \frac{\nu}{U_e\,(c_f/2)} \frac{d\sqrt{c_f/2}}{dx} \right] \left(y^{+} \left\langle \overline{u'^2} \right\rangle^{+} + \int_0^{y^{+}} \left\langle \overline{u'^2} \right\rangle^{+} dy^{+} \right)}_{V} \\
+ \underbrace{\frac{\nu}{U_e \sqrt{c_f/2}} \int_0^{y^{+}} \frac{\partial \left\langle \overline{u'^2} \right\rangle^{+}}{\partial x} dy^{+}}_{VI} .
\end{aligned}
\tag{2.3}
$$

Equation (2.3) is the extended Volino and Schultz equation and differs from that of Volino and Schultz[88] in that the spatial averaging operators, $\langle \cdots \rangle$, and the dispersive stress term, $-\langle \tilde{u}\tilde{v} \rangle^{+}$, are included here. The dispersive stress term arises because of the spatial averaging and becomes significant when time-averaged velocities vary significantly over the area being spatially averaged.

Terms in equation (2.3) are ordered according to their relative significance in the near-wall region as in Volino and Schultz[88]. For turbulent smooth-wall

data from Morrill-Winter et al.[51], Volino and Schultz[88] found that term I was the only significant term from the wall to $y/\delta = 0.04$, term II is zero for ZPG flow, terms I and III are the only significant terms up to $y/\delta = 0.2$, and terms I, III, and IV provided a good fit to data up to $y/\delta = 0.4$. In the above ranges, wall-normal distance was normalized by boundary layer thickness, δ. Terms V and VI are derived from the Reynolds normal stress term and have been found to be insignificant[88].

The goal of the derivation presented next is to extend the usefulness of equation (2.3) to experiments where data from only a single streamwise location is available. This requires that terms with streamwise gradients are reformulated so that they may be calculated indirectly using only the velocity profile data from a single streamwise location, rather than directly by using multiple profiles as in Volino and Schultz[88]. The derivation that follows will consider only nominally ZPG boundary layers. Additionally, terms V and VI have been found to be insignificant and will subsequently be neglected[88].

2.2.1.1 Determining the friction velocity gradient

Term III contains the streamwise friction velocity gradient, $\frac{d}{dx}\sqrt{c_f/2}$, or equivalently, $\frac{d}{dx}(u_\tau/U_e)$. This term is of primary concern because Volino and Schultz[88] have shown it is significant for determining u_τ from data between approximately $0.04 \leq y/\delta \leq 0.2$. This is also the region where there is the best

chance of accurately determining u_τ from equation (2.3) because experimental Reynolds shear stress measurements are more accurate outside of the immediate vicinity of the wall and because experimental errors which may build up in the integrals of terms III and IV are minimized. A convenient reformulation of this term is possible through the skin friction law and the momentum integral equation (MIE) by extending work of Clauser[15], Rotta[68], and Castro[9]. The derivation is more easily completed using an alternate form of equation (2.1) (expressed with the roughness length) and the wake function:

$$U^+ \equiv \frac{U}{u_\tau} = \frac{1}{\kappa} \ln\left(\frac{y}{y_0}\right) + \frac{\Pi}{\kappa} W\left(\frac{y}{\delta}\right). \tag{2.4}$$

Roughness length, y_0, is related to ΔU^+ by

$$\Delta U^+ = A + \frac{1}{\kappa} \ln\left(\frac{y_0 u_\tau}{\nu}\right). \tag{2.5}$$

In velocity-defect form, equation (2.4) is

$$\frac{U_e - U}{u_\tau} = -\frac{1}{\kappa} \ln\left(\frac{y}{\delta}\right) + \frac{\Pi}{\kappa}\left(2 - W\left(\frac{y}{\delta}\right)\right). \tag{2.6}$$

The addition of the wake function, $W(y/\delta)$, to model the outer flow was first proposed by Coles[18]. The wake function is normalized so that the wake strength parameter, Π, accurately characterizes the strength of the wake relative to other

turbulent boundary layers. This study will use the most common definition of the boundary layer thickness, δ, namely the wall-normal distance where velocity reaches 99% of the freestream velocity (so that $U(\delta) = 0.99U_e$). Coles [18] does not utilize this definition of δ but rather defines it based on normalizing conditions for the wake function. Therefore, Coles' δ is about 10% to 30% larger than the 99% δ depending upon the specific wake function. Additionally, Coles [18] hypothesized that $W(y/\delta)$ is a universal function. This allowed him to define Π by the normalizing conditions as well. In an effort to avoid the assumption of a universal wake function in this work, Π will be defined by the wake function's maximum departure from equation (2.4) so that

$$\Pi = \frac{\kappa}{2} \max \left[U^+(y) - \frac{1}{\kappa} \ln \left(\frac{y}{y_0} \right) \right]. \tag{2.7}$$

This approach also avoids the wake strength's definition being tied to any single definition of boundary layer thickness while the maximum deviation typically still occurs very near the 99% δ (so that $W_{\max}(y/\delta \approx 1) = 2$).

Assuming that equations (2.4) and (2.6) accurately model a turbulent boundary layer velocity profile in an overlap region, Clauser [15] and Rotta [68] both show that a skin friction law is derived from substituting equation (2.4) into equation (2.6). The result is

$$\frac{U_e}{u_\tau} = \frac{1}{\kappa} \ln \left(\frac{\delta}{y_0} \right) + \frac{2\Pi}{\kappa}. \tag{2.8}$$

Equation (2.8) is the skin friction law but is not yet expressed in more customary terms with the local skin friction coefficient, c_f, and momentum thickness. In order to do that, recall that $c_f/2 \equiv (u_\tau/U_e)^2$ and shape factor, $H \equiv \delta^*/\theta$, where δ^* is the displacement thickness and θ is the momentum thickness.

If the definition of displacement thickness is applied to equation (2.6), δ^* is related to δ by

$$\frac{\delta^*}{\delta}\frac{U_e}{u_\tau} = \frac{\delta^*}{\delta}\sqrt{\frac{2}{c_f}} = \frac{1+\Pi\left[2-\int_0^\delta W d\left(y/\delta\right)\right]}{\kappa} \approx \frac{1+\Pi}{\kappa}. \tag{2.9}$$

Coles[18] imposed $\int_0^1 W d(y/\delta) = 1$ as one of the wake function normalization criteria and derived the final expression on the right with exact equivalence. Here, $\int_0^1 W d(y/\delta) = 1$ is assumed (rather than imposed) for the standard definition of δ, which for ZPG boundary layer flows is of sufficient accuracy for present purposes. With these relations, the skin friction law, (2.8), can be rewritten as in Castro[9] according to

$$\sqrt{\frac{2}{c_f}} = -\frac{1}{\kappa}\ln\left(\frac{1}{H}\sqrt{\frac{c_f}{2}}\right) + \frac{1}{\kappa}\ln\left(\frac{\theta}{y_0}\right) + K_\Pi, \tag{2.10}$$

where $K_\Pi = 2\Pi/\kappa - (1/\kappa)\ln\left[(1+\Pi)/\kappa\right]$. Castro further showed that this expression can be rearranged to

$$\frac{\theta}{y_0} = \frac{s-I}{s^2}e^{\kappa(s-K_\Pi)}, \tag{2.11}$$

where $s = \sqrt{2/c_f}$ and I is Clauser's integral parameter (defined as G in Clauser[15]). It is defined as

$$I = \int_0^\infty \left(\frac{U_e - U}{u_\tau}\right)^2 dy \Bigg/ \int_0^\infty \frac{U_e - U}{u_\tau} dy = \frac{H-1}{H}\sqrt{\frac{2}{c_f}}. \tag{2.12}$$

I can be calculated from the measured velocity profile using equation (2.12). However, to test the validity of the expression, it is convenient to assume a particular functional shape for the wake function, $W(y/\delta)$, so that I can be expressed as a function of Π only. Castro[9] showed that $I(\Pi) = (2 + 3.2\Pi + 1.522\Pi^2)/[\kappa(1+\Pi)]$ for Coles' wake function. Using this expression for I, it is then possible to plot equation (2.11) together with experimental data to test its validity because $\sqrt{c_f/2}$ remains a function of only θ/y_0 and Π.

Figure 2.1 shows $\sqrt{c_f/2}$ versus θ/y_0, as determined implicitly via equation (2.11) with $\Pi = 0.55$ and $\Pi = 0.70$, plotted together with recent experimental data. For the plotted curves, $I(\Pi)$ is calculated using Castro's expression for Coles' wake function, but it can be shown that the particular choice of ZPG wake function has minimal effect on the plotted curve. The experimental data show that equation (2.11) models a wide variety of surfaces quite well, from smooth to various types of rough surfaces. For instance, data from Morrill-Winter et al.[51] are from smooth surfaces, Squire et al.[80] are from sand-grain surfaces, Placidi and Ganapathisubramani[61] are from LEGO® block surfaces, and Castro[9] are

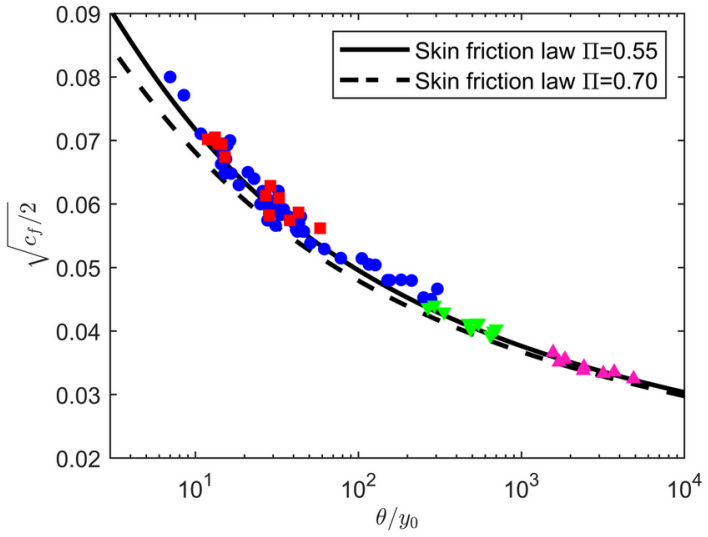

Figure 2.1: Skin friction law modeled by equation (2.11) with experimental data from multiple sources. Blue circles (●) indicate Castro[9] mesh, cubes, rectangular blocks, and sand-grain surfaces, magenta up triangles (▲) indicate Morrill-Winter et al.[51] smooth-wall surfaces, green down triangles (▼) indicate Squire et al.[80] P36 sandpaper surfaces, and red squares (■) indicate Placidi and Ganapathisubramani[61] LEGO® block surfaces.

from mesh, cubes, rectangular blocks, and sand-grain surfaces.

Figure 2.1 also shows that $\Pi = 0.55$ appears to model the data more closely than $\Pi = 0.70$. This is expected at lower skin frictions but interesting at higher skin frictions. Since higher skin frictions are generally those with more aggressive roughness which generally have larger wake strengths[35], one would expect the experimental data to match the $\Pi = 0.70$ curve more closely at higher skin frictions. This deviation from the expectation may be due to the assumption $\int_0^1 W d(y/\delta) = 1$ which led to the approximate expression of equation (2.9) being used in the subsequent derivation. The authors have tried various definitions of δ to evaluate the integral explicitly, however none of these efforts yielded

a better agreement to the experimental data in figure 2.1. If this is true, it may be best to assume a value of $\Pi = 0.55$ in equation (2.11) regardless of the actual measured value from equation (2.7). However, the deviation may also be due to the small favorable pressure gradient imposed by the fixed cross-section tunnels used in both Castro[9] and Placidi and Ganapathisubramani[61]. This small favorable pressure gradient would tend to reduce the wake strength causing these data points to potentially follow a lower wake strength curve. Due to the ambiguity, the present work uses Π calculated by equation (2.7) rather than an assumption at each step in the solution process. There is one exception explicitly documented for comparison in figure 2.5.

The ultimate goal of this derivation is to calculate the friction velocity gradient, $\frac{d}{dx}\sqrt{c_f/2}$. Now that a clear relationship between $\sqrt{c_f/2}$ and θ/y_0 has been demonstrated (note that equation (2.11) defines an implicit equation for $s = \sqrt{c_f/2}$ as function of θ/y_0), it remains to link θ with x. For ZPG boundary layers, the classical momentum integral analysis yields such a link, namely $c_f/2 = d\theta/dx$ (see also Castro[9]). It follows that

$$\frac{d\sqrt{c_f/2}}{dx} = \frac{\frac{d}{ds}\sqrt{c_f/2}}{dx/ds} = -\frac{e^{-\kappa(s-K_\Pi)}}{y_0 s^2}\left[1 + (s-I)\left(\kappa - \frac{2}{s}\right)\right]^{-1}, \tag{2.13}$$

where $\frac{d}{ds}\sqrt{c_f/2} = -1/s^2$ and $dx/ds = s^2\, d\theta/ds$ have been used.

Equation (2.13) shows that $\frac{d}{dx}\sqrt{c_f/2} = f\,(s,\, y_0,\, \Pi,\, I)$ and provides a condition

relating these quantities that will be used as part of an iterative process. Initially, u_τ and y_0 (and therefore s from U_e/u_τ, Π from equation (2.7), and I from equation (2.12)) may be unknown, but an initial guess of approximate values for these quantities may be obtained from the measured velocity profile and then further refined iteratively as described in section 2.2.3.

2.2.1.2 Determining the velocity gradient profile

Term IV from equation (2.3) contains the streamwise velocity gradient profile, $\partial\langle U\rangle^+/\partial x|_{y^+}$. By making evidence-based assumptions about the streamwise development of the boundary layer, it is possible to evaluate this term from a single mean velocity profile. Empirical evidence supporting the steps to follow are provided from studies such as Castro[9], Sillero et al.[78], Morrill-Winter et al.[51], and Squire et al.[80]. Starting from equation (2.4) and taking a derivative with respect to x yields

$$\left.\frac{\partial\langle U\rangle^+}{\partial x}\right|_{y^+} = \frac{1}{\kappa}\frac{\partial}{\partial x}\left[\ln\left(\frac{y}{y_0}\right)\right]_{y^+} + \frac{W}{\kappa}\frac{\partial\Pi}{\partial x} + \frac{\Pi}{\kappa}\frac{\partial}{\partial x}\left[W\left(\frac{y}{\delta}\right)\right]_{y^+}. \tag{2.14}$$

The first term can be neglected by recognizing that $y/y_0 = y^+/y_0^+$ and hence that $\frac{\partial}{\partial x}[\ln(y/y_0)]_{y^+} = 0$ if $\partial y_0^+/\partial x = 0$. From equation (2.5), the latter condition is equivalent to assuming that ΔU^+ and A are independent of x, which is consistent with the empirical evidence that a set of normalized profiles separated

by a streamwise distance over a homogeneous surface collapses in the log-law region once the flow is fully developed. This can be seen also in figure 2.2a on both smooth and rough-wall data sets. Thus the streamwise gradient of the logarithmic term, $\frac{\partial}{\partial x}[\ln(y/y_0)]_{y^+}$, can be neglected.

The second term in equation (2.14) is discussed next. Careful examination of currently available sources yielded no theory or experimental fit which allows the magnitude of $\partial\Pi/\partial x$ to be calculated accurately for a generic boundary layer. It is clear from Sillero et al.[78] that this term is positive at low Reynolds number and becomes negligible in fully developed smooth-wall turbulent boundary layers above about $Re_\theta \gtrsim 6000$. It should also be negligible for any fully rough turbulent boundary layer.

The remaining term contains $\partial W/\partial x$. The strategy for evaluating this term with a mean streamwise velocity profile from only one streamwise location is to link it with $d\theta/dx$ through the chain rule. Defining $\eta = y/\delta$, the derivative becomes

$$\frac{\partial}{\partial x}\left[W\left(\frac{y}{\delta}\right)\right]_{y^+} = \frac{dW}{d\eta}\frac{\partial}{\partial x}\left[\frac{y^+}{\delta^+}\right]_{y^+} = \frac{dW}{d\eta}\left(\frac{-y^+}{\delta^{+2}}\right)\frac{\partial \delta^+}{\partial x}$$
$$= \left(-\frac{y^+}{\delta^{+2}}\right)\left(\frac{u_\tau}{\nu}\frac{d\delta}{d\theta}\frac{d\theta}{dx} + \frac{\delta}{\nu}\frac{du_\tau}{dx}\right)\frac{dW}{d\eta}. \quad (2.15)$$

The relation, $c_f/2 \equiv (u_\tau/U_e)^2$, can be substituted to obtain a result consistent with the terms of equation (2.3). Also, an additional relation is required for

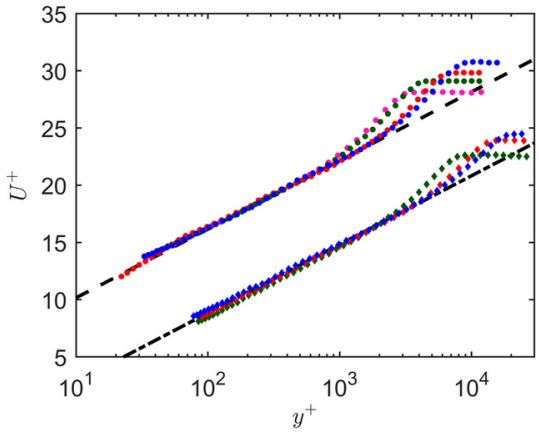

(a) Inner scaling

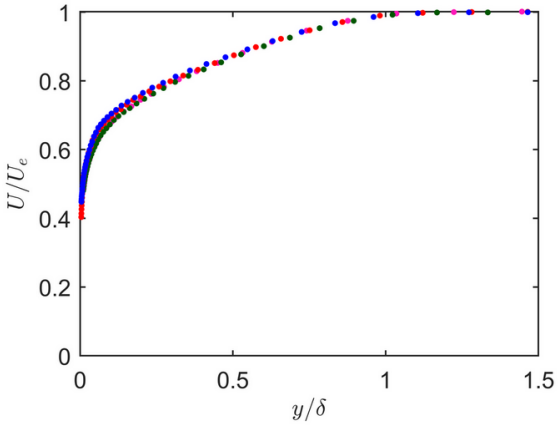

(b) Outer scaling (smooth-wall)

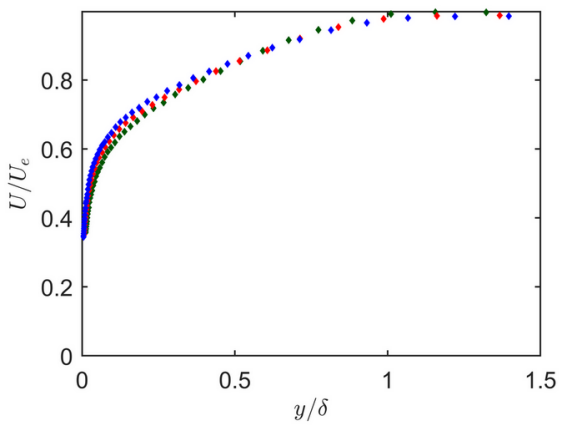

(c) Outer scaling (rough-wall)

Figure 2.2: Scaled boundary layer profiles developing over increasing fetch. Circles (●) are from Morrill-Winter et al.[51] smooth surface, and diamonds (⧫) are from Squire et al.[80] sandpaper surface. Profile locations are: magenta at $x = 4.5\,\text{m}$, green at $x = 7.0\,\text{m}$, red at $x = 11.9\,\text{m}$, and blue at $x = 18.0\,\text{m}$. Black dashed line is the smooth-wall log-law, and black dash-dot line is the rough-wall log-law.

$d\delta/d\theta$. An approximation of this term can be found by noting that the plots seen in figures 2.2b and 2.2c of streamwise velocity profiles in the form of U/U_e versus y/δ from Morrill-Winter et al.[51] and Squire et al.[80] nearly collapse under this scaling. These velocity profiles are separated by a streamwise distance of approximately 20δ. A δ-scale differential streamwise distance would be expected to show even better collapse. This gives evidence that the integral $\int_0^\infty U/U_e(1-U/U_e)d\eta$ is approximately constant. Noting

$$\int_0^\infty \frac{U}{U_e}\left(1-\frac{U}{U_e}\right)d\left(\frac{y}{\delta}\right) = \frac{1}{\delta}\int_0^\infty \frac{U}{U_e}\left(1-\frac{U}{U_e}\right)dy = \frac{\theta}{\delta} \approx C, \tag{2.16}$$

it may be concluded that δ/θ is approximately constant and thus equal to $d\delta/d\theta$. The momentum thickness grows proportionally with the boundary layer thickness for a fully developed boundary layer. This is consistent with often cited derivations from Schlichting[72] in which a $1/7$ power-law model was used to derive $\theta/\delta = 7/72$. The difference here is that, instead of assuming a velocity profile model, the data from the measured profile can be used to approximate the ratio. Momentum and boundary layer thickness are again assumed to grow proportionally over a differential streamwise distance, and the measured δ/θ is substituted for $d\delta/d\theta$.

The above substitutions result in the final expression

$$\left.\frac{\partial\langle U\rangle^+}{\partial x}\right|_{y^+} = -\frac{\Pi y}{\kappa\delta}\left[\frac{1}{\theta}\frac{d\theta}{dx} + \sqrt{\frac{2}{c_f}}\frac{d\sqrt{c_f/2}}{dx}\right]\frac{dW}{d\eta}$$
$$= -\frac{\Pi y^+}{\kappa}\left[\frac{1}{\theta}\frac{d\theta}{dx} + \sqrt{\frac{2}{c_f}}\frac{d\sqrt{c_f/2}}{dx}\right]\frac{\partial W}{\partial y^+}. \quad (2.17)$$

The first term in brackets captures the effect of boundary layer growth (note that equation (2.15) requires that W scales with δ), and the second term arises because the vertical length-scale changes as u_τ changes with fetch. The magnitude of these two terms can be easily compared for ZPG flows adding some insight. The bracketed part of the equation is equivalently

$$\left[\frac{1}{\theta}\frac{d\theta}{dx} + \sqrt{\frac{2}{c_f}}\frac{d\sqrt{c_f/2}}{dx}\right] = \frac{1}{\theta}\frac{d\theta}{dx} + \frac{1}{2}\left(\frac{d\theta}{dx}\right)^{-1}\frac{d^2\theta}{dx^2}. \quad (2.18)$$

Using the well known scaling $\theta \sim x^{4/5}$ for turbulent boundary layers, the first term in the brackets is about eight times larger than the second and has an opposite sign. The changing length-scale has an order of magnitude smaller effect on the derivative when compared to the the boundary layer's growth.

The ZPG MIE is $d\theta/dx = c_f/2$ and can be substituted for $d\theta/dx$ in equation (2.17). Thus, with $\partial\langle U\rangle^+/\partial x|_{y^+}$ expressed in terms of Π, θ, $c_f = 2s^2$ and $\frac{d}{dx}\sqrt{c_f/2} = f(s,y_0,\Pi,I)$, the integration over y^+ required to evaluate term IV can be performed.

2.2.1.3 Test on DNS data from smooth-wall turbulent boundary layers

The present analysis and approximations described in the prior sections are used to evaluate the terms of equation (2.3), and the resulting profiles are compared with data from from DNS of Sillero et al.[78]. This database provides detailed statistics for ZPG smooth-wall turbulent boundary layers from Re_θ of 4000 to 6500 in increments of 500. Figure 2.3 shows the terms of equation (2.3) calculated from the $Re_\theta = 6000$ profile statistics. The study's published u_τ was used to normalize all values. The Reynolds shear stress, $-\overline{u'v'}^+$, is the only non-zero term on the left hand side of equation (2.3) since there was no spatial averaging required for this study. The left hand side of equation (2.3) is plotted in the figure with black diamonds. The right hand side terms of equation (2.3) which were calculated directly from multiple streamwise profiles are plotted in the figure with different dashed line styles. Profiles at Re_θ of 5500, 6000, and 6500 were used to calculate the streamwise gradients using a second order accurate central difference numerical method at constant y^+. The right hand side terms of equation (2.3) which were calculated indirectly using the present techniques described in this study for a single streamwise profile are plotted with solid lines with markers. Equation (2.13) requires κ and y_0 as parameters. $\kappa = 0.41$ and $A = 5.1$ were assumed, and $y_0 = (\nu/u_\tau)e^{-\kappa A}$ was used as appropriate for a smooth wall.

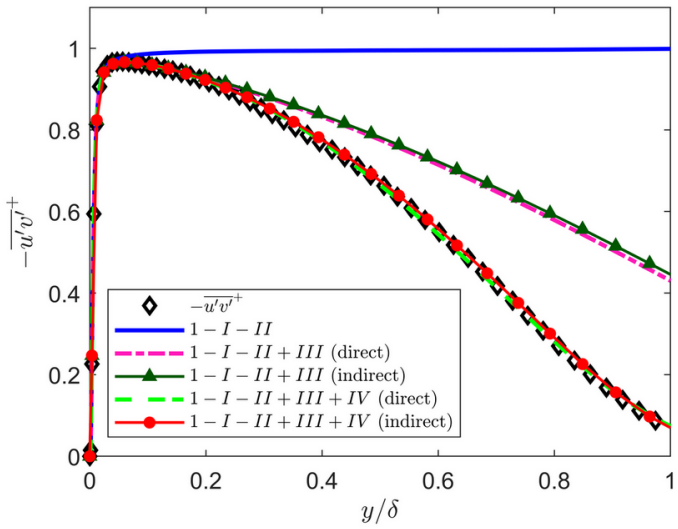

Figure 2.3: Terms of equation (2.3) as indicated in the legend for turbulent smooth-wall ZPG DNS of Sillero et al.[78] at $Re_\theta = 6000$. Black diamonds ($\Diamond$) are measured Reynolds shear stress. Dashed curves utilize directly calculated streamwise gradient terms. Solid curves with markers utilize the present method for indirectly calculating streamwise gradient terms.

Figure 2.3 shows the terms calculated with the two methods show excellent agreement with each other and the measured Reynolds shear stress data. Other pairs of κ and A found in the literature could have been selected and would have resulted in a small but observable difference in figure 2.3. $\kappa = 0.41$ and $A = 5.1$ were selected because they gave the best visual fit to the log-law region velocity data (not shown). This gives good confidence that the assumptions used to derive the indirect formulas for streamwise gradient terms were sound at least when applied to these data.

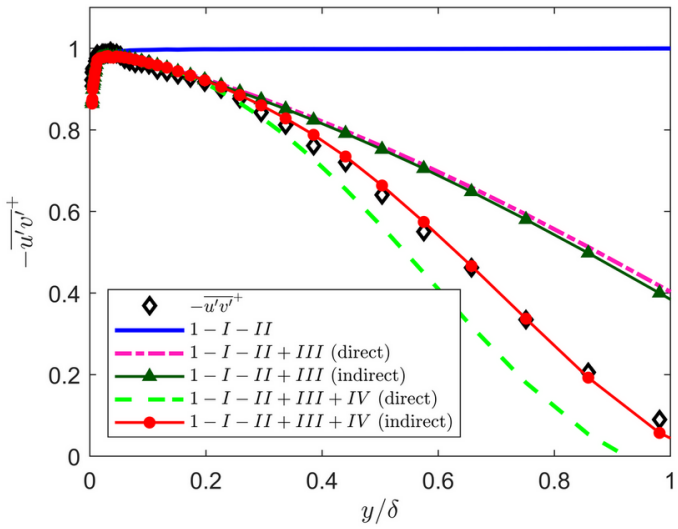

Figure 2.4: Terms of equation (2.3) as indicated in the legend for turbulent smooth-wall ZPG flow of Morrill-Winter et al.[51] at $Re_\tau = 6080$. Black diamonds ($\Diamond$) are measured Reynolds shear stress. Dashed curves utilize directly calculated streamwise gradient terms. Solid curves with markers utilize the present method for indirectly calculating streamwise gradient terms.

2.2.1.4 Test on experimental data from smooth-wall turbulent boundary layers

Next, the accuracy of the proposed approximations to the various terms in the momentum balance are tested on the smooth-wall ZPG experimental data of Morrill-Winter et al.[51]. The data set was acquired in the High Reynolds Number Boundary Layer Wind Tunnel (HRN-BLWT) at the University of Melbourne. The profiles shown in figure 2.4 are from $x = 11.9\,\text{m}$ with $U_e = 15.3\,\text{m/s}$.

Solid lines with markers show the present method. $\kappa = 0.384$ and $A = 4.17$ provided a close visual fit to the log-law region velocity data (not shown) and are common in experiments from the HRN-BLWT. Terms I and II are the same as in

Volino and Schultz[88] and fit the measured Reynolds shear stress data very well through $y/\delta = 0.04$. Adding term III, the fit to data is very good through $y/\delta = 0.2$. Adding term IV, both the direct and present methods fit the data well through $y/\delta = 0.3$. Above $y/\delta = 0.3$, the direct method slightly underestimates the shear stress while the present method shows good agreement to the measured shear stress data throughout the entire boundary layer.

2.2.1.5 Test on experimental data from rough-wall boundary layers

Figure 2.5 shows the direct and indirect methods of calculating equation (2.3) for data from Squire et al.[80] with a ZPG turbulent boundary layer developing over a P36 grit sandpaper surface in the HRN-BLWT at the University of Melbourne. The profiles shown in figure 2.5 are from $x = 15$ m with $U_e = 17.4$ m/s. Both the direct and the present method fit the measured Reynolds shear stress data well through $y/\delta = 0.2$ with terms I, II, and III included. The direct method maintains a good fit through the entire boundary layer when also including term IV. The present method overestimates the Reynolds shear stress above $y/\delta = 0.2$. This seems to be due to an underestimation of the friction velocity gradient magnitude in term III by equation (2.13). Red open circles show the result if term III is calculated assuming $\Pi = 0.55$ in equation (2.13) rather than calculating Π from equation (2.7) (as was suggested for some circumstances

in section 2.2.1.1). A better fit to the data is observed with this assumption, and both the direct and present methods yield a close fit to the measured data through the entire boundary layer.

The overall very good agreement between total shear stress profiles determined using the proposed single profile approach and measured shear stress data confirms that the approach may be used to accurately estimate the friction velocity from profiles at a single downstream position. It bears recalling that the essential assumption underlying the approach is a universal collapse of data as shown in figure 2.1 as well as some secondary assumptions, namely that W scales with δ and $d\delta/d\theta = \delta/\theta$ and that normal turbulent stress and $\partial\Pi/\partial x$ contributions are negligible.

2.2.2 Determining roughness length and zero-plane displacement

Rough walls add the need to determine the roughness length, y_0, and zero-plane displacement, d. As has been done by Placidi and Ganapathisubramani [61] among others who have determined friction velocity independently, roughness length and zero-plane displacement can be determined by fitting the log-law equation (2.4) with measured mean streamwise velocity data in the log-law region. If a two-parameter fit of equation (2.4) is required, a convenient way

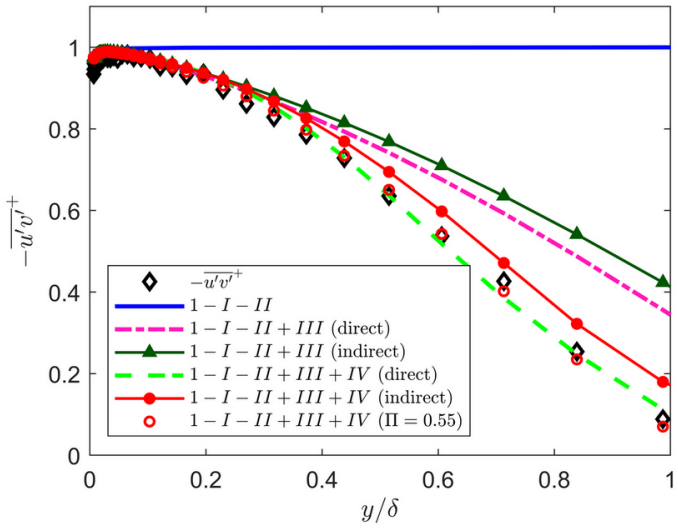

Figure 2.5: Terms of equation (2.3) as indicated in the legend for turbulent sand-grain surface ZPG flow of Squire et al.[80] at $Re_\tau = 13140$. Black diamonds ($\Diamond$) are measured Reynolds shear stress. Dashed curves utilize directly calculated streamwise gradient terms. Solid curves with markers utilize the present method for indirectly calculating streamwise gradient terms. Red open circles ($\circ$) utilize the present method and calculate term III assuming $\Pi = 0.55$ in equation (2.13).

to do this is to use a linear regression solver on a linear form of equation (2.4), $e^{\kappa U/u_\tau} = (1/y_0)y - d/y_0$. The left hand side is known (or estimated if u_τ is unknown). If m and b are solutions for slope and intercept respectively, then $y_0 = 1/m$ and $d = -b/m$.

If y_0 or d is known or can be reasonably assumed, then a one-parameter fit to equation (2.4) may yield more accurate results. For example, Squire et al.[80] assumed that d was at the midpoint of the sand-grain valleys and peaks and then performed a one-parameter fit for y_0.

It is also possible to use the log-law equation to determine y_0 for smooth-wall boundary layers and apply the present method to smooth surfaces. It should be noted that y_0 has no physical meaning for smooth walls. However, the relations presented prove useful in applying the present method to smooth walls. By assuming $d = 0$ and $\Delta U^+ = 0$ and equating equations (2.1) and (2.4), smooth-wall y_0 can be calculated by the explicit formula $y_0(u_\tau) = (\nu/u_\tau)e^{-\kappa A}$. As can be seen, smooth-wall y_0 is not constant since it is still dependent on u_τ.

2.2.3 Practical implementation: iterative method

When friction velocity is initially unknown, it may be determined through equations (2.3) and (2.4) through an iterative method. The process is illustrated

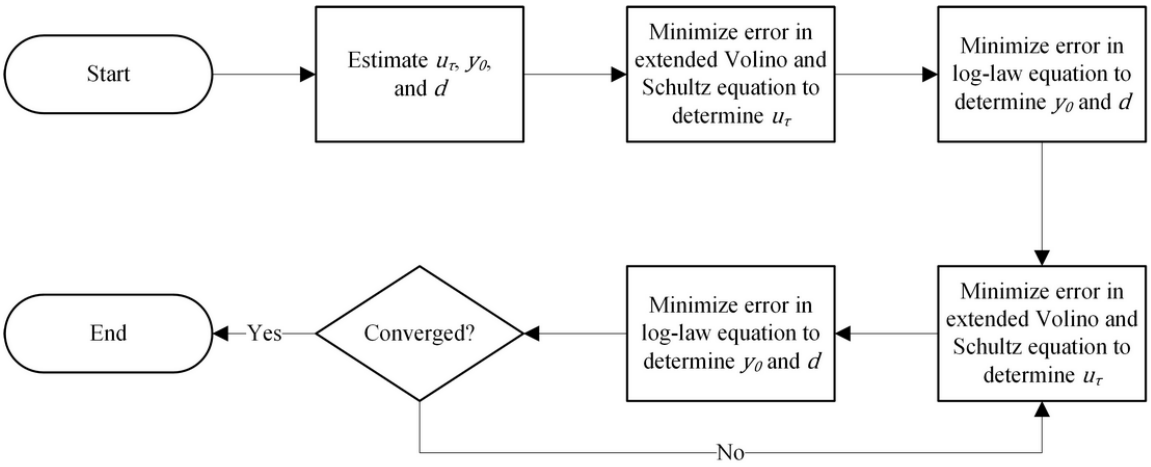

Figure 2.6: Flowchart of the iterative process for solving u_τ, y_0, and d. The extended Volino and Schultz equation refers to (2.3), and the log-law equation refers to (2.4).

in a flowchart in figure 2.6. An initial estimate of the friction velocity, roughness length, and zero-plane displacement is required since both equations have dependencies in all three variables. Then, equation (2.3) is used to determine u_τ with the estimated y_0 and d by minimizing the error in equation (2.3) (note that u_τ enters in all of the terms) as explained in more detail when presenting applications below. Equation (2.3) is not highly sensitive to errors in y_0 and d, so determining u_τ with this equation first is the best way to reduce error in the initial estimate. However, since u_τ is determined only semi-independently from equation (2.3), iterations are required to refine the solution. Next, equation (2.4) is used to determine y_0 and d with the calculated u_τ from the previous step. Then, solution refinement proceeds iteratively between equations (2.3) and (2.4) until a specified stopping criteria is met. The stopping criteria for the

experimental data sets shown in section 2.3 were three significant digits for u_τ and y_0 or 10 iterations. Most data sets converged within a few iterations.

2.3 Applications to various experimental data sets

In this section the analysis of terms in the momentum balance equation (which was presented in the prior section and led to the iterative method to determine the friction velocity based on single-location mean velocity and Reynolds shear stress profiles) is used to determine boundary layer parameters for various experimental data sets. Where required, κ and A were assumed to be 0.384 and 4.17 respectively throughout section 2.3. The resulting friction velocities are compared to direct measurements using force balances or to prior published values.

2.3.1 Boundary layers over rough sand-grain surfaces

The comprehensive shear stress boundary layer analysis method was applied to the sand-grain boundary layer data from Squire et al.[80]. This study recorded detailed fluid profile statistics with a cross-wire anemometry probe at multiple

Reynolds numbers. The study also utilized a drag balance for independently measuring friction velocity directly at three of the Reynolds numbers tested. The present method is used to analyze turbulent boundary layer data with only the fluid measurements and without the friction velocity data from the force balance at the three Reynolds numbers profiled above the drag balance location. Figure 2.7 shows the present method's result for the sand-grain surface with $Re_\tau = 6770$. Figure 2.7a shows the mean streamwise velocity profile versus wall-normal distance, and figure 2.7b shows the Reynolds shear stress data versus wall-normal distance, in inner and outer scaling respectively. The outer-scaled wall-normal distance, ψ, is calculated by

$$\psi = \frac{y - d}{\delta - d}. \tag{2.19}$$

Evidence from Volino and Schultz[88] showed that reasonable estimates of flow below the nearest velocity data to the wall can be used to improve results. The estimated velocities only affect the integral terms in equation (2.3). In the following results, a cubic interpolation is used to estimate mean streamwise velocity between the nearest data point and an assumed zero velocity at $y = d$. Flow below $y = d$ is assumed to be a negligible portion of the integrals, which is consistent with evidence from Volino and Schultz[88]. This is not proposed as a universal method for interpolation but works well for better estimating the

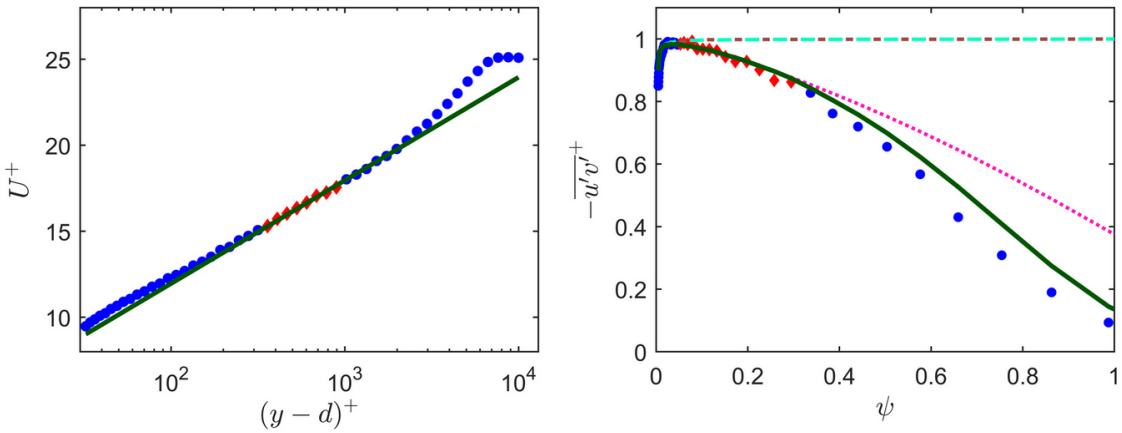

(a) Mean velocity **(b)** Shear stress

Figure 2.7: Comparison of data and fits from the proposed method for mean velocity (2.7a) and shear stress (2.7b) profiles from Squire et al.[80] at $Re_\tau = 6770$. Blue circles (●) are measured data, and red diamonds (♦) are fitted data. Fit to (2.4) performed on data between $0.07 < \psi_{(k)} < 0.15$, and fit to (2.3) performed on data between $0.05 < \psi_{(k)} < 0.30$. Green lines show (2.4) in figure 2.7a and (2.3) in figure 2.7b. Dotted or dashed line styles show components of (2.3): brown dash-dot line is $1 - I$, cyan dashed line is $1 - I - II$, and magenta dotted line is $1 - I - II + III$.

integral terms of equation (2.3).

Having presented the results from the method as applied to the data, some details about the iterative procedure are presented next. Initial estimates for u_τ, y_0, and d may be used with equations (2.3) and (2.4) to start the iterative process shown in figure 2.6 for solving the unknowns. To illustrate the process, root mean square (RMS) error plots in the variable parameter space are shown in figure 2.8. The RMS error for equation (2.3) is calculated as usual according

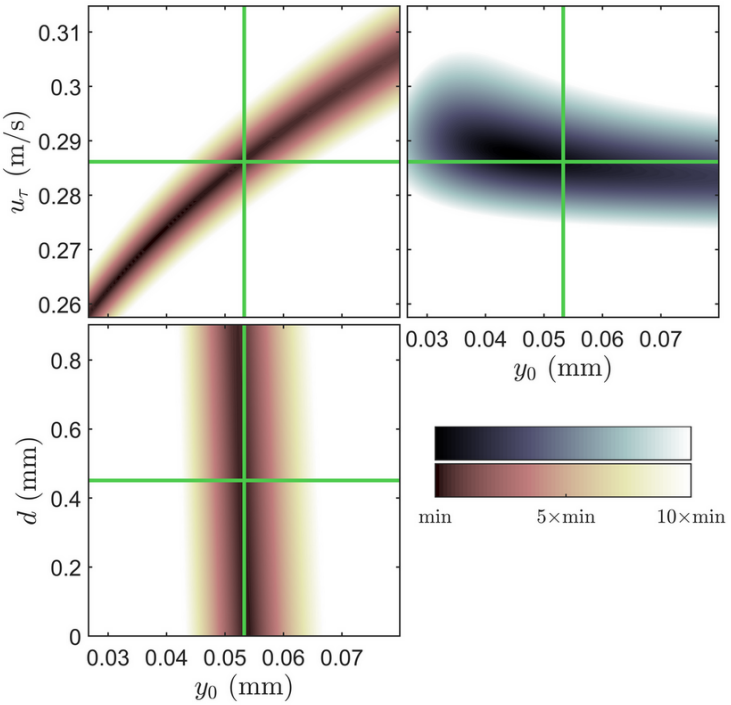

Figure 2.8: Contour plots of RMS errors of fits to experimental data for boundary layer flow over sand-grain surface at $Re_\tau = 6770$ from Squire et al.[80]. Left plots show the mean velocity RMS errors between equation (2.4) and experimental data in the range $0.07 < \psi_{(k)} < 0.15$ calculated as shown in equation (2.21). The upper right plot shows the RMS error between equation (2.3) and experimental data in the range $0.05 < \psi_{(k)} < 0.30$ calculated as shown in equation (2.20). The green lines show the converged values for u_τ, y_0, and d on the plots.

to

$$\text{RMS error} = \sqrt{\frac{1}{n}\sum_{k=1}^{n}\left[-\left\langle\overline{u'v'}\right\rangle^{+}_{(k)} - \left\langle\tilde{u}\tilde{v}\right\rangle^{+}_{(k)} - (1 - I - II + III + IV)_{(k)}\right]^2}, \tag{2.20}$$

where the summation is over the n experimental data points between $0.05 < \psi_{(k)} < 0.30$. The plot on the upper right of figure 2.8 shows the RMS error in the $u_\tau - y_0$ plane and indicates that the RMS error is much more sensitive to changes in u_τ than changes in y_0 in the fitted region. The process of solving equation (2.3) for u_τ effectively solves for the minimum on a vertical line of this plot since y_0 is assumed as given in this step of the process. This plot also helps illustrate that the error minimization from the comprehensive shear stress profile is well suited for solving u_τ accurately.

The upper and lower left plots show RMS error for equation (2.4) for the experimental data between $0.07 < \psi_{(k)} < 0.15$ calculated by

$$\text{RMS error} = \sqrt{\frac{1}{n}\sum_{k=1}^{n}\left[\frac{\left\langle U\left(y_{(k)}\right)\right\rangle}{u_\tau} - \frac{1}{\kappa}\ln\left(\frac{y_{(k)} - d}{y_0}\right)\right]^2}. \tag{2.21}$$

The lower left plot is the RMS error in the $d - y_0$ plane which is the solution plane of interest for this step in the process. The range of d on the vertical axis encompasses the total height of the sand-grain roughness from valleys to peaks. This is the total possible range for d in accordance with the physical definition

proposed by Jackson[33]. The plot shows a strong dependence on y_0 but very weak dependence on d in this range. For some experimental data sets including this case, a two-parameter fit of equation (2.4) can result in non-physical values of d which should fall between the peaks and valleys of the roughness. Therefore, in some cases it may be more advantageous to assume a reasonable d. For the case of figure 2.7 and the other two cases in table 2.1, d was assumed to be the midpoint between peaks and valleys of the sand-grain surface as was assumed by Squire et al.[80] and Morrill-Winter et al.[52]. Then a numerical solver was used to minimize equation (2.21) with y_0 only, which solves for the minimum error on a horizontal line of the lower left plot of figure 2.8 rather than the absolute minimum error as a two-parameter fit would.

Iteration between solving equation (2.3) for u_τ and solving equation (2.4) for y_0 converges to a unique solution because of the different sensitivities in the $u_\tau - y_0$ plane shown in the two upper plots of figure 2.8. Iteration progresses until the process converges to a unique solution. The green lines show the converged values for u_τ, y_0, and d for the case of figure 2.7.

Table 2.1 contains the three cases from Squire et al.[80] where fluid profiles were measured directly over the HRN-BLWT drag balance. Table 2.1 shows that the results from the present method of determining friction velocity agree with the direct drag balance measurements within $\pm 1\%$. This agreement is well within the experimental uncertainties and shows the present method to

Re_τ	Drag balance (m/s)	Present method (m/s)	Percent difference
6770	0.288	0.286	-0.47%
12300	0.488	0.490	0.41%
17190	0.698	0.693	-0.67%

Table 2.1: Squire et al.[80] published drag balance friction velocity and the present method's calculated friction velocity by fitting data between $0.05 < \psi_{(k)} < 0.30$ to equation (2.3) and fitting data between $0.07 < \psi_{(k)} < 0.15$ to equation (2.4)

be a reliable analysis technique when only fluid dynamic measurements are available at a single streamwise location.

2.3.2 Boundary layers over smooth walls

Next, the present method is applied to the smooth-wall fluid profile data from Morrill-Winter et al.[51]. Determining y_0 and d from the log-law equation (2.4) in the flowchart of figure 2.6 is replaced with the explicit formula $y_0(u_\tau) = (\nu/u_\tau)e^{-\kappa A}$ and with $d = 0$ as described in section 2.2.2. Figure 2.9 shows fits of equations (2.3) and (2.4) for the smooth-wall ZPG flow at $Re_\tau = 1951$.

Table 2.2 shows friction velocity results for a range of Reynolds numbers from the HRN-BLWT smooth-wall cases. The present method calculates u_τ within $\pm 1\%$ of the published values from a single profile of fluid dynamic measurements for all cases analyzed. While this study did not utilize a drag balance for friction velocity, Morrill-Winter et al.[51] used the composite fit method from Chauhan et al.[10] which has been validated extensively. The very good agreement of

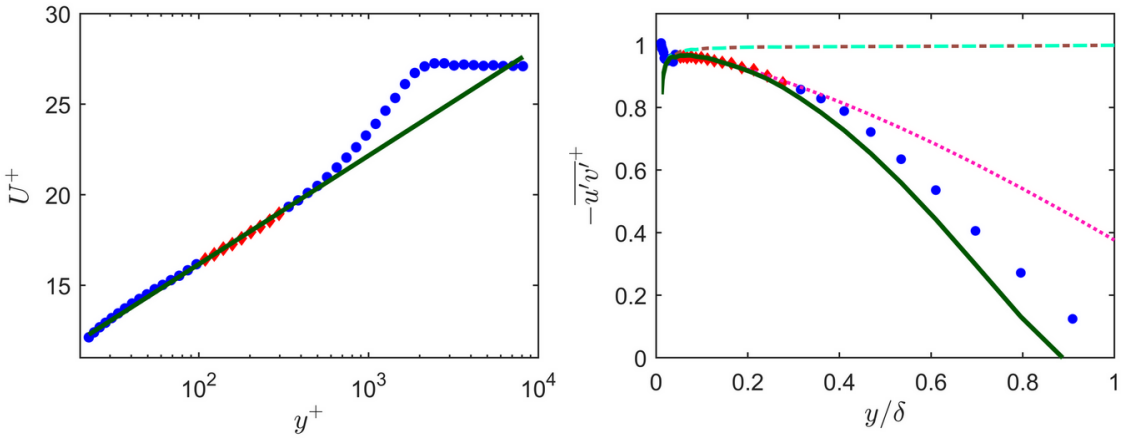

(a) Mean velocity **(b)** Shear stress

Figure 2.9: Comparison of data and fits from the proposed method for mean velocity (2.9a) and shear stress (2.9b) profiles from Morrill-Winter et al.[51] at $Re_\tau = 1951$. Blue circles (●) are measured data, and red diamonds (♦) are fitted data. Fit to equation (2.4) performed on data between $0.07 < y_{(k)}/\delta < 0.15$, and fit to equation (2.3) performed on data between $0.05 < y_{(k)}/\delta < 0.30$. Green lines show equation (2.4) in figure 2.9a and equation (2.3) in figure 2.9b. Dotted or dashed line styles show components of equation (2.3): brown dash-dot line is $1 - I$, cyan dashed line is $1 - I - II$, and magenta dotted line is $1 - I - II + III$.

results in figure 2.9 and table 2.2 again show the present method to be a very accurate analysis technique and the indirect methods for calculating streamwise gradients in equation (2.3) to be reliable.

2.3.3 Boundary layers over arrays of wall attached staggered cubes

The present method is also demonstrated for boundary layer data from Cheng and Castro[12] for flow over an array of wall attached cubes. Cross-wire

Re_τ	Published value (m/s)	Present method (m/s)	Percent difference
1951	0.368	0.370	0.53%
2622	0.356	0.357	0.22%
2928	0.541	0.543	0.41%
3770	0.519	0.517	-0.40%
3844	0.340	0.341	0.16%
5593	0.334	0.336	0.55%
6080	0.512	0.510	-0.39%
7894	0.497	0.497	0.04%

Table 2.2: Morrill-Winter et al.[51] published friction velocities and the present method's calculated friction velocities by fitting data between $0.05 < \psi_{(k)} < 0.30$ to equation (2.3) and fitting data between $0.07 < \psi_{(k)} < 0.15$ to equation (2.4)

anemometry profiles were recorded at multiple locations over a repeating unit for five different cases. Spatially-averaged profiles from the $20\,$mm staggered cube array with 25% planform surface density are shown here in figure 2.10 with fits from equations (2.3) and (2.4). Since the profiles shown are spatially averaged, the dispersive shear stress term is non-zero and included although it is small enough to be considered negligible. RMS error plots for these fits are shown in figure 2.11. Equation (2.4) is fit for data between $0 < \psi_{(k)} < 0.22$ which is equivalent to the published range used for this fit by Cheng and Castro[12]. Equation (2.3) was fit between $0.15 < \psi_{(k)} < 0.30$. Additionally, this test case had a single $20\,$mm brass cube which was instrumented with 21 pressure taps on the windward and leeward sides of the cube to directly measure pressure drag. In the fully rough regime, the pressure drag is very nearly the total surface drag. The same geometry was also tested in Cheng et al.[11] with both

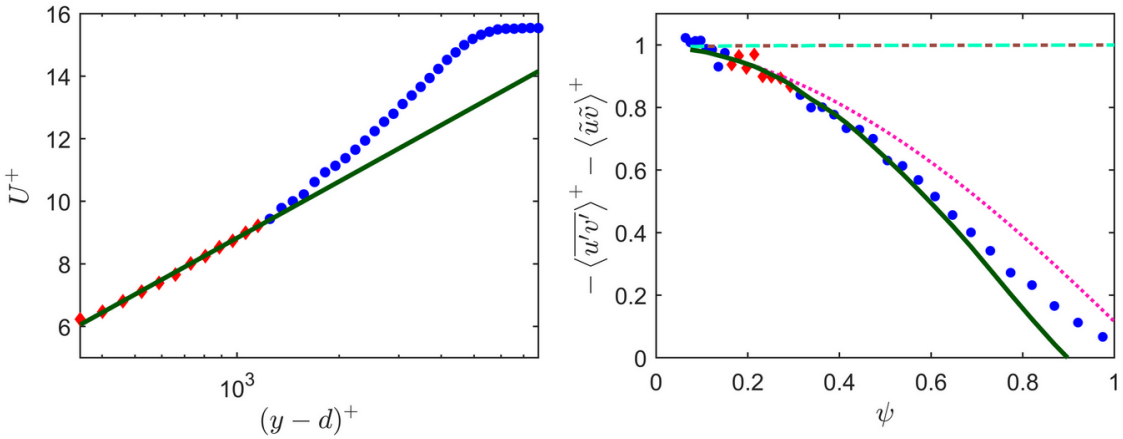

(a) Mean velocity **(b)** Shear stress

Figure 2.10: Comparison of data and fits from the proposed method for mean velocity (2.10a) and shear stress (2.10b) profiles from Cheng and Castro[12] for flow over staggered $20\,\text{mm}$ cubes. Blue circles (●) are measured data, and red diamonds (♦) are fitted data. Fit to equation (2.4) performed on data between $0 < \psi_{(k)} < 0.22$, and fit to equation (2.3) performed on data between $0.15 < \psi_{(k)} < 0.30$. Green lines show equation (2.4) in figure 2.10a and equation (2.3) in figure 2.10b. Dotted or dashed line styles show components of equation (2.3): brown dash-dot line is $1 - I$, cyan dashed line is $1 - I - II$, and magenta dotted line is $1 - I - II + III$.

the pressure-tapped cube and a floating element drag balance which will allow additional comparison for the friction velocity results.

As is evident from the results in table 2.3, the present comprehensive shear stress method does not seem any better than earlier approaches. The difference between the present method and the direct measures is still approximately $8 - 11\%$. Additionally, even though equation (2.3) seems to fit the shear stress data below $\psi < 0.5$ in figure 2.10b, there are visual discrepancies in the slope particularly in the near-wall region, $\psi < 0.25$, where the equation should be the most accurate (due to less experimental error in the integral terms). This

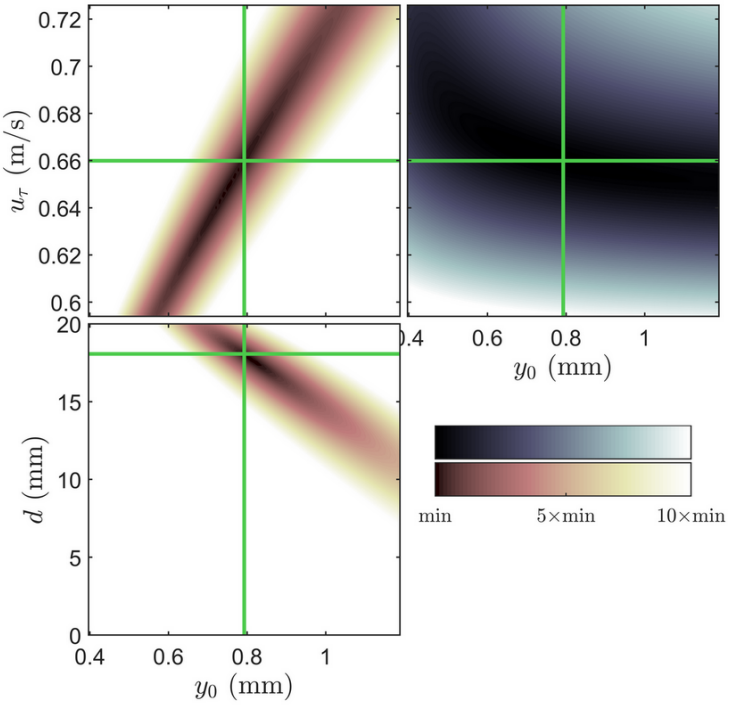

Figure 2.11: Contour plots of RMS errors of fits to experimental data for boundary layer flow over staggered cubes from Cheng and Castro[12]. Left plots show the mean velocity RMS errors between equation (2.4) and experimental data in the range $0 < \psi_{(k)} < 0.22$ calculated as shown in equation (2.21). The upper right plot shows the RMS error between equation (2.3) and experimental data in the range $0.15 < \psi_{(k)} < 0.30$ calculated as shown in equation (2.20). The green lines show the converged values for u_τ, y_0, and d on the plots.

Friction velocity method	$\frac{u_\tau}{U_e}$	Percent difference from PT	Percent difference from FE
Pressure tapped cube form drag (PT)	0.0718	0.0%	1.5%
Floating element drag balance (FE)	0.0707	-1.5%	0.0%
Published traditional total shear stress	0.0640	-10.9%	-9.6%
Comprehensive shear stress (present)	0.0644	-10.3%	-8.9%

Table 2.3: Differences between published friction velocities and the present method's calculated friction velocity assuming ZPG. Hot-wire profiles for the present method were from Cheng and Castro[12]. Published friction velocities are from Cheng et al.[11].

difference tends to lower the fitted value of friction velocity in agreement with other fluids based methods and is no closer to the direct measurements.

The key problem with the results in table 2.3 is the discrepancy between the direct measurement methods and total shear stress methods (including the present method as applied above). In study after study, the traditional total shear stress methods seem to under-predict the friction velocity which has resulted in considerable discussion in the literature, such as in Cheng et al.[11], Claus et al.[14], and Ferreira et al.[19]. The discussions persist to this date because, to the authors' knowledge, this empirical discrepancy has not been quantified by physical equations. Additionally, studies by Reynolds and Castro[67] and Placidi and Ganapathisubramani[61] both cite Cheng and Castro[12] and Cheng et al.[11] for evidence-based corrections to the friction velocity which they determine from traditional total shear stress methods.

One of the possibilities noted by Cheng et al.[11] and Ferreira et al.[19] is that a small favorable pressure gradient (FPG) may cause this effect on the Reynolds shear stress. The University of Surrey and University of Southampton tunnels where these studies were conducted are considered nominally zero pressure gradient. However, both tunnels have a fixed cross-sectional area which imposes a small favorable pressure gradient due to boundary layer growth. From reported boundary layer growth in Cheng et al.[11] and the tunnel dimensions, it can be estimated that the acceleration parameter was approximately $K =$

2×10^{-8}. This acceleration parameter is small (but non-zero) and in the range of values from the similarly-sized fixed cross-section tunnel in Placidi and Ganapathisubramani[63].

Therefore, in evaluating term IV, $d\theta/dx$ may be replaced with the full MIE shown by

$$\frac{d\theta}{dx} = \frac{c_f}{2} - \left(\frac{2\theta}{\delta} + \frac{\delta^*}{\delta}\right)\left(\frac{U_e\delta}{\nu}\right)K \tag{2.22}$$

to solve $\partial\langle U\rangle^+/\partial x|_{y^+}$ from equation (2.17). Also, for term III, equation (2.13) may still be used to solve $\frac{d}{dx}\sqrt{c_f/2}$. The evidence from Castro[9] indicates that equation (2.13) still holds for small FPG boundary layers. Castro[9] shows a plot of c_f versus $(x - x_0)/y_0$. Equation (2.13) is derived from the curve in Castro's plot, and most (if not all) of the experimental data on the plot are from fixed cross-section tunnels with small FPGs.

Figure 2.12 shows Cheng and Castro[12] cross-wire anemometry data with fits from equations (2.3) and (2.4) using the present method. Equation (2.3) is now calculated for a small FPG which assumes $K = 2 \times 10^{-8}$. Equation (2.3) now agrees with the turbulent shear stress data well through $\psi < 0.4$. Furthermore, it matches the slope below $\psi < 0.25$ where it had not previously. Comparing figures 2.10b and 2.12b, the effect on the terms of equation (2.3) is readily seen. Term II, a purely pressure dependent term, was zero in figure 2.10 but about half of the total shear stress throughout the boundary layer in figure 2.12. Additionally, the magnitude of both terms III and IV were reduced due to the

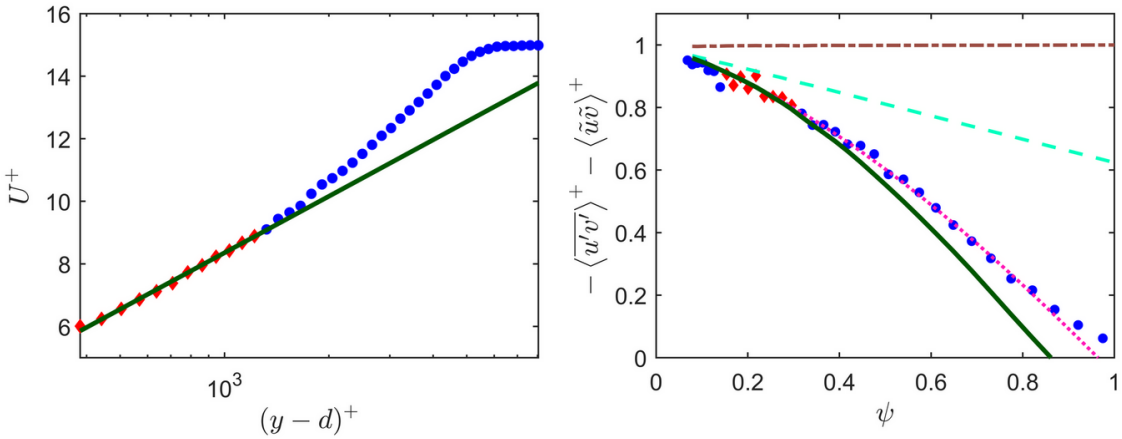

(a) Mean velocity **(b)** Shear stress

Figure 2.12: Comparison of data and fits from the proposed method for mean velocity (2.12a) and shear stress (2.12b) profiles from Cheng and Castro[12] for flow over staggered $20\,\text{mm}$ cubes. Blue circles (●) are measured data, and red diamonds (♦) are fitted data. Fit to equation (2.4) performed on data between $0 < \psi_{(k)} < 0.22$, and fit to equation (2.3) performed on data between $0.15 < \psi_{(k)} < 0.30$. Green lines show equation (2.4) in figure 2.12a and equation (2.3) in figure 2.12b. Dotted or dashed line styles show components of equation (2.3): brown dash-dot line is $1 - I$, cyan dashed line is $1 - I - II$, and magenta dotted line is $1 - I - II + III$. Equation (2.3) is calculated assuming a small FPG with $K = 2 \times 10^{-8}$.

positive K in term III and equation (2.22). The overall effect from the pressure gradient flattened the turbulent shear stress profile throughout the boundary layer by reducing the inertial terms and increasing the pressure-dependent terms.

Table 2.4 compares results from the present method now assuming a small favorable pressure gradient. The present result is now 7% lower than the pressure tapped cube and 6% lower than the floating element drag balance. This is encouraging because the comprehensive shear stress method is now within the

Friction velocity method	$\frac{u_\tau}{U_e}$	Percent difference from PT	Percent difference from FE
Pressure tapped cube form drag (PT)	0.0718	0.0%	1.5%
Floating element drag balance (FE)	0.0707	-1.5%	0.0%
Published traditional total shear stress	0.0640	-10.9%	-9.6%
Comprehensive shear stress (present)	0.0668	-7.0%	-5.6%

Table 2.4: Differences between published friction velocities and the present method's calculated friction velocity assuming small FPG with $K = 2 \times 10^{-8}$. Hot-wire profiles for the present method were from Cheng and Castro [12]. Published friction velocities are from Cheng et al. [11].

10% published uncertainty of the pressure tapped cube measurements in Cheng et al. [11]. The floating element drag balance does not appear to have published information regarding experimental uncertainty. It may be assumed that the uncertainty is at least 3% which would be in line with other floating element drag balances used in a similar tunnel by Placidi and Ganapathisubramani [61] and Ferreira et al. [19]. Additionally, the uncertainty in the present method is unknown especially given that K was estimated with limited information. Given these uncertainties the present method appears to be an improvement to prior single fluid profile measurement approaches.

2.3.4 Boundary layers over arrays of LEGO® blocks

Placidi and Ganapathisubramani [61],[62] tested twelve fully rough surfaces with

different repeating patterns of LEGO® blocks. The studies were nominally zero pressure gradient and reported that $K < 5 \times 10^{-8}$. The authors published the data set online in Placidi and Ganapathisubramani[63] which included calculated pressure gradients. The study published u_τ values from direct measurement with a force balance, and y_0 and d were found with a least square regression of the log-law equation using the friction velocity measured from the force balance. The drag balance in this study was based on the design documented in Krogstad and Efros[40] and is expected to be more accurate than the one in Cheng et al.[11].

Turbulent boundary layer data plotted in figure 2.13 were recorded by particle image velocimetry over the surface geometry named LP2 at $Re_\tau = 7642$. Figure 2.13 shows fits to the particle image velocimetry data for equations (2.3) and (2.4). Placidi and Ganapathisubramani[63] published $K = 4.3 \times 10^{-8}$ for this case. Equation (2.4) was fitted to velocity data between $0.07 < \psi_{(k)} < 0.15$ in figure 2.13a, and equation (2.3) was fitted to shear stress data between $0.15 < \psi_{(k)} < 0.30$ in figure 2.13b.

All six surfaces from Placidi and Ganapathisubramani[61] with constant frontal density (LP1 - LP6) were analyzed with the present method assuming both a ZPG and a small FPG. In some cases, it was necessary to fix the range of possible d to within the roughness height due to the physical interpretation of d described in Jackson[33]. Placidi and Ganapathisubramani[61] also noted this was necessary for some cases in their analysis. Results are included in table

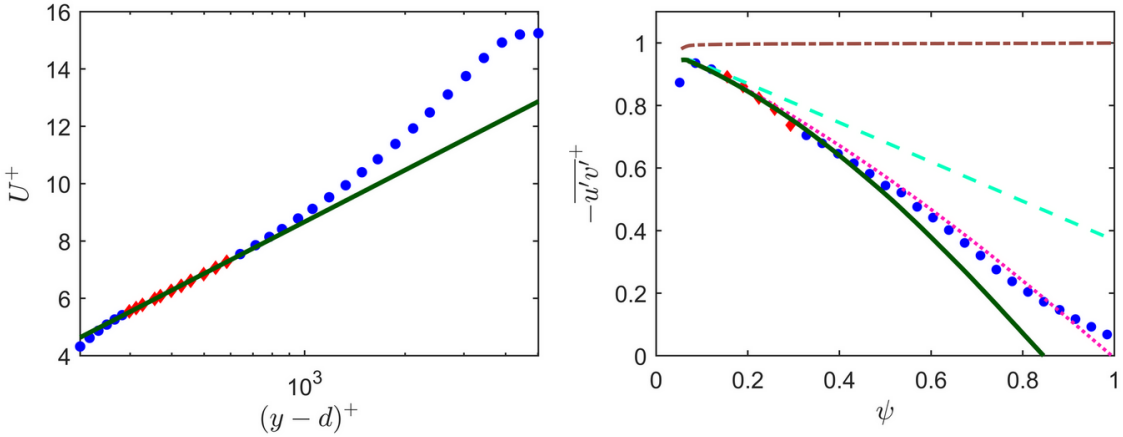

(a) Mean velocity **(b)** Shear stress

Figure 2.13: Comparison of data and fits from the proposed method for mean velocity (2.13a) and shear stress (2.13b) profiles from Placidi and Ganapathisubramani[61] LEGO® block geometry LP2 at $Re_\tau = 7642$. Blue circles (●) are measured data, and red diamonds (♦) are fitted data. Some data points were removed for clarity. Fit to equation (2.4) performed on data between $0.07 < \psi_{(k)} < 0.15$, and fit to equation (2.3) performed on data between $0.15 < \psi_{(k)} < 0.30$. Green lines show equation (2.4) in figure 2.13a and equation (2.3) in figure 2.13b. Dotted or dashed line styles show components of equation (2.3): brown dash-dot line is $1 - I$, cyan dashed line is $1 - I - II$, and magenta dotted line is $1 - I - II + III$. Equation (2.3) is calculated with K from table 2.5.

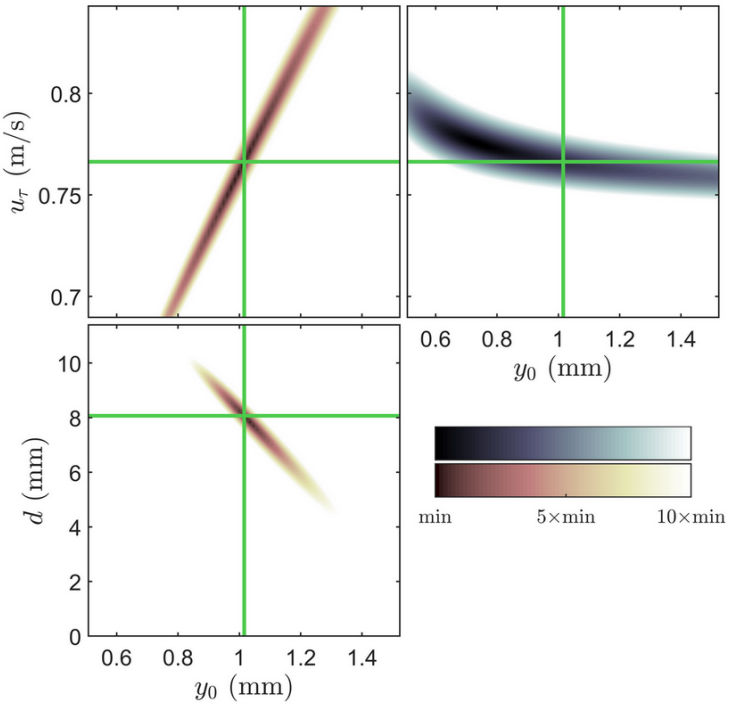

Figure 2.14: Contour plots of RMS errors of fits to experimental data for boundary layer flow from Placidi and Ganapathisubramani[61] LEGO® block geometry LP2. Left plots show the mean velocity RMS errors between equation (2.4) and experimental data in the range $0.07 < \psi_{(k)} < 0.15$ calculated as shown in equation (2.21). The upper right plot shows the RMS error between equation (2.3) and experimental data in the range $0.15 < \psi_{(k)} < 0.30$ calculated as shown in equation (2.20). The green lines show the converged values for u_τ, y_0, and d on the plots.

Case	Drag balance (m/s)	Present method with ZPG (m/s)	Percent difference (ZPG)	Present method with FPG (m/s)	Percent difference (FPG)	K $\times 10^{-8}$
LP1	0.81	0.81	-0.4%	0.82	1.3%	1.2
LP2	0.78	0.72	-7.9%	0.77	-1.8%	4.3
LP3	0.71	0.68	-3.9%	0.71	-0.1%	2.9
LP4	0.67	0.65	-2.8%	0.69	3.7%	4.3
LP5	0.66	0.62	-5.9%	0.66	0.3%	4.2
LP6	0.67	0.55	-18.4%	0.56	-16.8%	1.2

Table 2.5: Differences between Placidi and Ganapathisubramani[61] published drag balance friction velocity and the present method's calculated friction velocities by fitting data between $0.15 < \psi_{(k)} < 0.30$ to equation (2.3) and fitting data between $0.07 < \psi_{(k)} < 0.15$ to equation (2.4). Acceleration parameters, K, obtained from Placidi and Ganapathisubramani[63].

2.5. The present method's result was consistently lower than the drag balance measurement when a ZPG was assumed but was close to the experimental uncertainty of the drag balance for five of the six cases when the reported K (for the small FPG) was utilized. Case LP6, which differed by -19% or -17%, remains as an outlier for which the present fluid dynamic measurements alone do not agree with the drag balance measurement.

Placidi and Ganapathisubramani[61] reported that it was necessary to increase u_τ determined from traditional total shear stress methods by 12% in order to obtain agreement within 5% of the drag balance results for all cases. The present method does not need a correction factor and achieves considerably better results both assuming a ZPG and small FPG. Utilizing the reported K for the small FPG leads to results that are near the uncertainty of the study's drag

balance in a tunnel similar to the one in Cheng and Castro[12]. These results give strong evidence that the small FPG explains the often cited friction velocity discrepancy from Cheng and Castro[12].

2.3.5 Friction velocity sensitivity

The comprehensive shear stress method assumes κ, the fitting range for the log-law equation (2.3), and the fitting range for the extended Volino and Schultz equation (2.4) when solving for u_τ, y_0, and d. A trivariate sensitivity analysis was performed on surface geometry LP2 from Placidi and Ganapathisubramani[61]. Converged values of u_τ, y_0, and d were calculated for all 150 combinations of κ, fitting range to equation (2.3), and fitting range to equation (2.4) from table 2.6. Figure 2.15 shows scatter plots of the results projected onto the three planes created by u_τ, y_0, and d. Friction velocity results show low sensitivity to the assumed parameters with u_τ bounded within $\pm 2\%$ of the results from section 2.3.4.

While friction velocity showed low sensitivity, results for y_0 ranged from 38% below to 5% above the results from section 2.3.4. Also, results for d included nearly the entire upper $1/3$ of the roughness height. These variances were primarily from the high sensitivity inherent in the fitting the log-law equation, (2.4). The present method shares this limitation with other methods that rely on two-parameter fits to the log-law equation. However, the selected log-law

κ	Fitting range for (2.3)	Fitting range for (2.4)
0.38	$0.10 < \psi_{(k)} < 0.25$	$0.00 < \psi_{(k)} < 0.15$
[0.384]	$0.15 < \psi_{(k)} < 0.25$	$\left[\, 0.07 < \psi_{(k)} < 0.15 \,\right]$
0.39	$0.10 < \psi_{(k)} < 0.30$	$0.10 < \psi_{(k)} < 0.15$
0.40	$\left[\, 0.15 < \psi_{(k)} < 0.30 \,\right]$	$0.00 < \psi_{(k)} < 0.19$
0.41	$0.20 < \psi_{(k)} < 0.30$	$0.07 < \psi_{(k)} < 0.19$
		$0.10 < \psi_{(k)} < 0.19$

Table 2.6: Parameter variations for univariate and trivariate sensitivity analysis for Placidi and Ganapathisubramani[61]. Bracketed parameters indicate the initial assumptions from section 2.3.4.

fitting range does not greatly affect the friction velocity result.

A univariate analysis was also performed for all cases with constant frontal density from Placidi and Ganapathisubramani[61] excluding the outlier, LP6. In each plot of figure 2.16, one of the three assumed parameters was allowed to vary with the values listed in table 2.6 while maintaining the initial assumptions from section 2.3.4 in the other two parameters. The varying parameter is labeled on the horizontal axis with the vertical axis showing the maximum positive and negative percent difference to the u_τ reported in table 2.5 for each case. The figure shows that each of the three assumptions individually affect the friction velocity result by less than $\pm 1\%$.

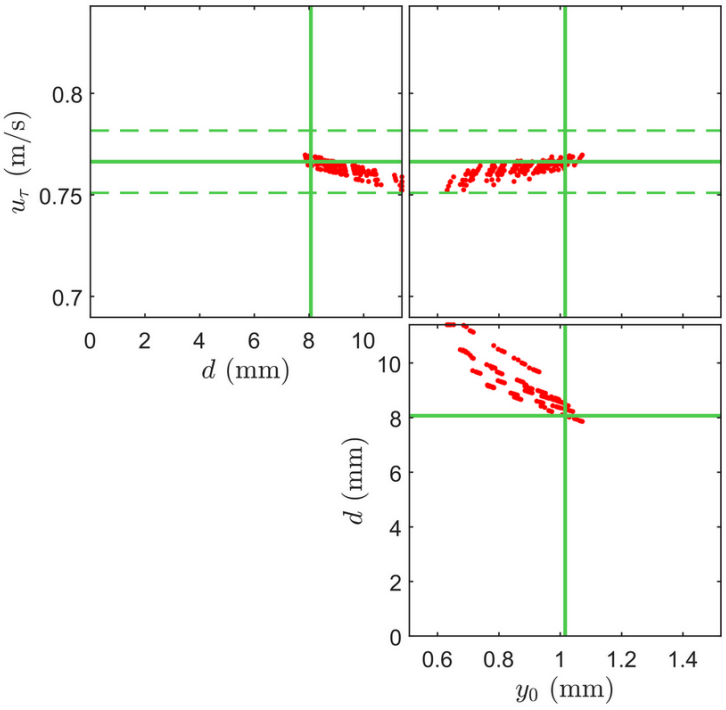

Figure 2.15: Scatter plots showing u_τ, y_0, and d trivariate sensitivity to assumptions of κ, fitting range for equation (2.3), and fitting range for equation (2.4) applied to data from Placidi and Ganapathisubramani[61] LEGO® block geometry LP2. The solid green lines show the converged values plotted in figure 2.14. The dashed green lines show $u_\tau \pm 2\%$.

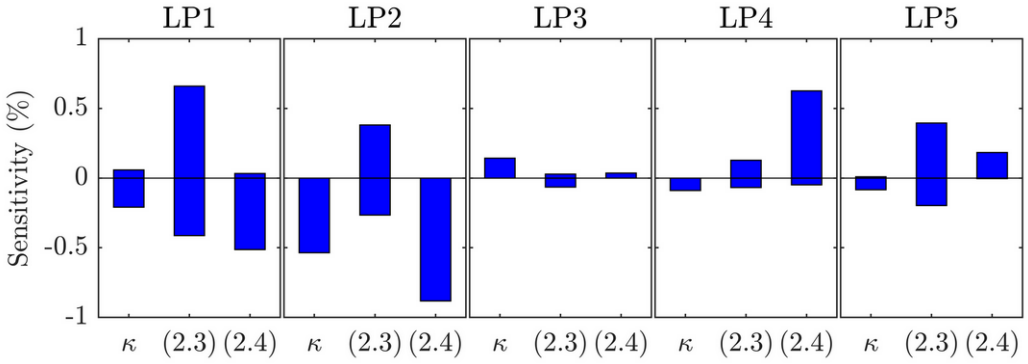

Figure 2.16: Bar plots showing univariate sensitivity of u_τ to assumptions of κ, fitting range for equation (2.3), and fitting range for equation (2.4) applied to data from Placidi and Ganapathisubramani[61]. Percent sensitivity bars show the maximum positive and negative percent differences to the u_τ reported in table 2.5 for each case.

2.4 Summary

2.4.1 Key assumptions

Several key assumptions were included in the derivation and application of the present method and are reviewed here. First, simplification of the integral form of the Reynolds-averaged and spatially-averaged streamwise momentum equation assumed that Reynolds normal stresses were negligible and the flow was two-dimensional. Second, the derivation assumed that the skin friction law, (2.10), was applicable. There were several assumptions embedded in the skin friction law which were discussed in section 2.2.1.1, but the skin friction law was shown to have robust applicability both in section 2.2.1.1 and Castro[9]. Third, the friction velocity gradient used the ZPG MIE. However, it was noted that Castro[9] applied the ZPG MIE to nominally ZPG boundary layers with good agreement. Also, results from section 2.3 imply that this was a valid assumption for $K \lesssim 5 \times 10^{-8}$. Fourth, the velocity gradient profile derivation assumed that velocity profiles would collapse in outer-scaling over a streamwise distance. This condition implies that $\partial\Pi/\partial x \approx 0$, W scales with δ, and $\partial\delta/\partial\theta \approx \delta/\theta$ and is also sensitive to pressure gradient (and probably other parameters). However, the velocity gradient profile only appears in term IV of equation (2.3) which was not significant for $\psi < 0.3$ in most cases. Thus, it can be more easily avoided by choosing an appropriate fitting range.

2.4.2 Results and comparisons with other methods

Figure 2.17 compares published measured friction velocity for rough-wall cases and the published composite fit friction velocity for smooth cases to traditional total shear stress methods and to the present method. Red points for the present method fall close to the 45-degree line indicating excellent agreement with the published friction velocities. The one outlier is from surface LP6 from Placidi and Ganapathisubramani[61] as discussed in section 2.3.4. It is noted that no other method provided results within 11% of the measured friction velocity for this case. Other approaches are shown on the figure with blue, green, and grey symbols, showing larger scatter and a downward bias. The dotted line shows the total shear stress friction velocity for which a 12% correction would equal the drag balance friction velocity. It can be seen why it may be appropriate to utilize the 12% empirical correction for some cases from Placidi and Ganapathisubramani[61] utilizing all Reynolds shear stress data from the roughness sublayer and inertial sublayer. However, other methods utilizing the plateau in the Reynolds shear stress and peak Reynolds shear stress provided results closer to the solid line. All total shear stress methods performed comparably for the smooth- and rough-wall cases from Morrill-Winter et al.[51] and Squire et al.[80].

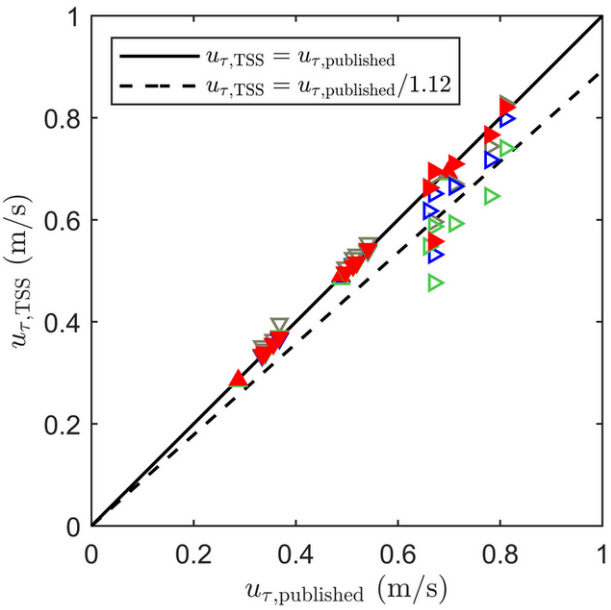

Figure 2.17: Friction velocities determined using different total shear stress (TSS) approaches, plotted against published friction velocities. Red symbols utilize the present comprehensive shear stress method. Open blue symbols utilize Reynolds shear stress points in the plateau region. Open green symbols utilize Reynolds shear stress points in the Roughness Sublayer and Inertial Sublayer (RS+IS). Open grey symbols utilize the peak Reynolds shear stress. Up triangle (▲) data are from Squire et al.[80]. Down triangle (▼) data are from Morrill-Winter et al.[51]. Right triangle (►) data are from Placidi and Ganapathisubramani[61].

Overall, no other total shear stress method performed as consistently well as the present method across all data sets considered. Besides one outlier, all cases utilizing the present method were within $\pm 4\%$ of the friction velocity measured with the drag balance.

2.5 Conclusions

A detailed analysis of several terms entering in the mean momentum balance of turbulent boundary layers was performed. The results were useful in formulating a new comprehensive shear stress method for determining friction velocity. The approach is based on measured profiles of mean velocity and turbulent shear stress at a single downstream location and can be used for analyzing nominally zero pressure gradient turbulent boundary layers. The approach extends an equation from Volino and Schultz[88] to include spatial averaging and to calculate streamwise gradients from a single streamwise location. Two key elements are necessary to indirectly calculate streamwise gradients from a single two-component velocity profile. The first key element is the replacement of the streamwise gradient of friction velocity with an assumption of the skin friction law and momentum integral equation. The second key element is the assumption that the wake function scales with boundary layer thickness and can be connected to the streamwise gradient through the momentum integral

equation. Application of the extended Volino and Schultz equation to various data sets showed the equation models turbulent shear stress data throughout the boundary layer. An iterative procedure combining fitting of the extended Volino and Schultz equation to the turbulent shear stress profile and fitting of the log-law equation to the mean velocity profile was proposed and implemented. Applications to various flows illustrated that the proposed method achieves similar friction velocity results as force balance measurements but only requires mean velocity and turbulent shear stress profiles. Results also demonstrated that even small pressure gradients, which can arise in fixed cross-section facilities, can have a significant (and often neglected) effect on turbulent shear stresses and may account for 10% or more in friction velocity discrepancy with force balance measurements. The comprehensive shear stress method presented can account for this discrepancy in nominally zero pressure gradient facilities, leading to improved accuracy when determining friction velocity and skin friction drag in boundary layer experiments with commonly available profile data.

An interactive graphical user interface (GUI) software is available for download as part of the supplementary materials provided at `http://pages.jh.edu/~cmeneve1/datasets.html`.

Chapter 3

Turbulent boundary layers over truncated cone roughness

3.1 Introduction

As already highlighted in prior chapters, rough-wall turbulent boundary layers have been studied extensively for nearly the last century[57;17;71;36], however reliable surface drag prediction remains a challenge. Initially the focus of study was drag prediction in pipe flows which was an important topic for engineering systems of the 1930s. However, in the 1950s attention turned toward turbulent boundary layers and the search for universal scaling laws, allowing the collapse of a streamwise mean velocity profile onto a single function. That universal function has become known as the log-law equation.

After over 50 years of rough-wall boundary layer research, Castro[9] noted remarkable universality in the ability of the log-law equation to describe the turbulent boundary layer velocity profile across a wide range of rough surfaces. There are two immediate consequences of turbulent boundary layer universality. First, how can it be utilized to build practical engineering models? Second, what are the limits of universality? Both of these questions have been explored in recent years.

For the first question, turbulent boundary layer universality has given hope for the possibility of robust topographic drag prediction models. However, the essential element is understanding how rough surface topography affects roughness length, y_0, or equivalently the roughness function, ΔU^+, or also equivalent sand-grain roughness, k_s. Chung et al.[13] provides a recent review of studies contributing to this ongoing effort. Most studies have postulated or examined drag prediction algorithms successfully within a small parameter space, however Chung et al.[13] highlights that further datasets are required for wider applicability and reduced uncertainty. Specifically, they note the need for an aggregation of systematic studies that sweep through the parameter space or test its limits (`http://roughnessdatabase.org/`).

For the second question, these drag prediction models, as well as many reduced-order wall-bounded numerical models, implicitly rely on a level of turbulent boundary layer universality. Therefore, knowing the limits of the

equation's applicability is vital for high reliability engineering applications. One important theory of turbulent boundary layer universality is Townsend's wall similarity hypothesis. Townsend's wall similarity hypothesis states that boundary layer turbulence outside of a small roughness layer is independent of the specific surface morphology and statistically similar when appropriately scaled[83]. This hypothesis implies what is known as outer-layer similarity[65]. Numerous studies have investigated this hypothesis and found significant supporting evidence[65;73;86;20], however other studies have exhibited roughness effects well into the outer-layer[39;38;87;62].

These studies give evidence that, at least under certain circumstances, Townsend's hypothesis does not hold. Researchers are actively working to identify universal criteria for which Townsend's hypothesis holds[34;73;21;97;2;62]. The lack of universal criteria which predicts outer-layer similarity highlights a lack of understanding of the physics which link surface characteristics to boundary layer statistics. This link is of fundamental scientific and engineering importance due to the prevalence of rough-wall boundary layers and may inform the construction or known limitations of future drag prediction models.

Very few studies have investigated the effect of regularly and irregularly arranged roughness elements on the turbulent boundary layer. Researchers have generally focused on systematic arrangements because it is easier to isolate important surface statistics or easier to manufacture surfaces. However, it is

not clear if the conclusions drawn from these studies are applicable to flow over random roughness. Irregular or random arrangements are very common in both engineering and nature. Mountains in the atmospheric boundary layer and barnacles in a ship hull boundary layer are both roughness types that do not appear in the regular arrangements normally investigated. Even engineered systems contain irregularity. The realistic turbine blade in Bons[7] has been studied extensively[97;98;49;50;5;58] but with little roughness parametric variation except Mejia-Alvarez and Christensen[49]. Wind farm inflow often develops over irregular terrain[82] and turbine arrangements often require irregularity due to topography or land use restrictions[77;81]. Research is just beginning to address these limitations. Forooghi et al.[23] recently conducted a direct numerical simulation parametric study with randomly distributed roughness elements but was limited to low Reynolds number due to computational costs. Experimental data at higher Reynolds number is insufficient and remains a current limitation in the understanding of rough wall turbulent boundary layer behavior.

In recent years, quite a few studies have focused on secondary flows as a way in which turbulent boundary layer universality breaks down. Secondary flows are mean flow features which manifest in the wall-normal spanwise plane (perpendicular to the dominant streamwise flow direction) and have long been studied in non-circular ducts[56;31;29;30]. Secondary flows were perhaps first noted

as a universality concern in rough-wall turbulent boundary layer wind tunnel experiments by Reynolds et al.[66], who observed spanwise-periodic velocity and turbulence intensity variations in measurements recorded at similar wall-normal distances over staggered cube surfaces. Further inspection revealed that the periodic variation was caused by secondary-flow counter-rotating vortical structures that seemed to correlate with periodic features on the rough surface below. These observations were used to caution about experimental studies with periodic surface features[66]. Studies which were to have widely applicable results should try to avoid the presence of such seemingly rare flow features.

It was implicitly assumed, though, that an irregular or random surface would not generate or sustain secondary flows. However, Mejia-Alvarez and Christensen[50] observed what they described as high momentum pathways (HMPs) and low momentum pathways (LMPs) over an multi-scale irregular surface generated from a scaled replica of a damaged turbine blade. They believed that the surface roughness promoted preferential pathways for flow structures that were detectable in the mean flow statistics. Later, Barros and Christensen[5] showed extensive stereo particle image velocimetry (PIV) plots of the structures in the wall-normal spanwise plane. They observed HMPs and LMPs in the mean streamwise velocity, reduced and enhanced Reynolds shear stress and turbulent kinetic energy in the HMPs and LMPs respectively, and counter-rotating vortical structures in the signed swirl strength. Barros and

Christensen further correlated these flow structures with relatively high and low upstream topography in the upstream fetch from the measurement plane. The Barros and Christensen[5] study prompted some important questions for rough-wall turbulence.

Anderson et al.[3] provided a possible explanation of the fundamental fluid dynamic mechanisms responsible for generating and sustaining the secondary flows within the turbulent boundary layer. In doing so, they were able to draw on the long history of research into non-circular duct secondary flows[29;30]. Anderson et al.[3] used the Reynolds-averaged turbulent kinetic energy balance equation to show that differences in the roughness across the span create spanwise regions that produce more and less turbulent kinetic energy. This turbulent kinetic energy imbalance, then, induces a secondary flow as the system attempts to reach mechanical energy stability. Their simulations show that HMP and LMP sustainment occurs when the spanwise heterogeneous wall roughness below is streamwise aligned.

Many other researchers have provided some answers to the question of what surface roughness conditions cause secondary flows to form and have probed their outer limits[93;3;84;45;99;91]. They have primarily looked at spanwise heterogeneity either in the form of elevated or recessed streamwise-aligned terrain or streamwise-aligned strips of alternating higher and lower drag-producing roughness. Parametric studies have probed the limits of the parameter space

and found that, in general, turbulent boundary layer secondary flows occur when spanwise heterogeneous feature spacing is between approximately $\delta/2$ and 2δ. When spanwise spacing is smaller, the features act as homogeneous roughness with effects confined to the roughness sublayer; and when spanwise spacing is larger, the features act as isolated flow perturbations[84;91;13].

The aim of this study is to examine the turbulent boundary layer over varying planform densities of staggered and random roughness elements, with particular focus on outer similarity and the occurrence and properties of secondary flow structures. Eight planform densities of truncated cone roughness elements in a square staggered pattern were investigated and varied between 10% and 78% density. The same planform densities were also investigated with random arrangements of truncated cones. The effect of increasing density on the turbulent boundary layer is determined for both regular and irregular morphologies. No additional spanwise heterogeneity was imposed but is locally present within the random distribution of truncated cones. The irregular random morphology is of special interest due to the prevalence of irregular roughness features occurring in nature and fouled engineering components and due to the limited availability of studies with irregular topographies.

Section 3.2 describes the experimental facility, roughness morphology, and flow measuring equipment utilized. Section 3.3 reports spatially-averaged results for both the staggered and random test series at all densities. A few

differences in turbulent boundary layer parameters are highlighted and examined. Section 3.4 presents measurements of HMPs and LMPs observed over the irregular arrangements of truncated cones that were not present over the regular staggered arrangements. HMP and LMP correlations with roughness topography are explored, and generation and sustainment mechanisms are postulated. In addition, HMP and LMP turbulent boundary layer parameters and statistics not previously reported in the literature are discussed. Conclusions are presented in section 3.5.

3.2 Experimental details

The experimental approach utilizes a boundary layer water tunnel which is described in section 3.2.1. Sixteen test surfaces of staggered and randomly-arranged truncated cones are described in section 3.2.2. Lastly, fluid velocity data were measured with a laser Doppler velocimetry system described in section 3.2.3 and a stereo particle image velocimetry system described in section 3.2.4.

3.2.1 Facility

Experiments were conducted at the Hydromechanics Laboratory at the United States Naval Academy in a recirculating boundary layer water tunnel.

The test section is nominally 2.00 m long with a 0.20 m wide by 0.10 m tall cross-section at the inlet. The upper wall was adjusted to set a zero pressure gradient, and the resulting acceleration parameter, $K = (\nu/U_e^2)[dU_e/dx]$, was less than 5×10^{-9} throughout the length of the test section for each test. All tests were conducted at a free-stream velocity of $U_e = 1.25$ m/s. In this study, (x, y, z) were the streamwise, wall-normal, and spanwise directions respectively. $y = 0$ was located on the lower surface to which the roughness elements were attached, and $z = 0$ was located at the center of the spanwise cross-section. Test surfaces were mounted on the lower wall of the tunnel. A 0.8 mm diameter wire trip was located 0.20 m from the tunnel inlet and served as the streamwise origin, $x = 0$. The roughness field began 0.78 m from the boundary layer trip, and velocity measurements were recorded nominally 1.50 m from the trip which was approximately 18δ from the start of the roughness. A heat pump system controlled fluid temperature to $20 \pm 1\,^{\circ}$C during tests, which in some cases lasted over 50 hours.

3.2.2 Roughness morphology

Sixteen test surfaces were constructed using high resolution additive manufacturing with a Stratasys Objet30 Pro 3D printer. Examples of all sixteen surfaces with their designated names are shown in figure 3.1. Eight cases had varying planform densities of truncated cone elements in a square staggered

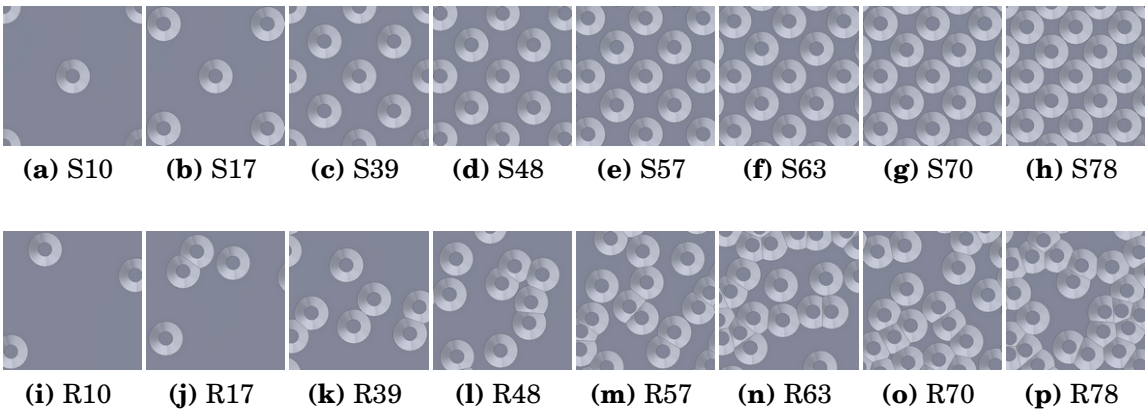

(a) S10 **(b)** S17 **(c)** S39 **(d)** S48 **(e)** S57 **(f)** S63 **(g)** S70 **(h)** S78

(i) R10 **(j)** R17 **(k)** R39 **(l)** R48 **(m)** R57 **(n)** R63 **(o)** R70 **(p)** R78

Figure 3.1: Test surfaces

pattern (figure 3.1(a)-(h)). In the most dense case, the truncated cone elements were touching but not overlapping at the base. The same eight planform densities were manufactured with random arrangements of the truncated cone elements (figure 3.1(i)-(p)). In the random cases, the elements were allowed to overlap but a minimum of 0.5 mm was maintained between the elements' upper plateaus. Cases were named with an S for staggered or R for random and then two digit percentage for the planform density.

Selected surface statistics for all sixteen test cases are documented in table 3.1. Variable $h(x, z)$ is the local surface height. The table provides values for planform density (λ_p), frontal density (λ_f), effective slope, mean height $\langle h \rangle$, height standard deviation (σ_h), height skewness (s_k), and height flatness.

Figure 3.2 illustrates the calculation of planform and frontal density. Planform density is best illustrated in the figure 3.2(a) and (c) top views. Planform density is calculated from the sum of all truncated cone faces (red, green, and

blue) projected on the base plane then divided by the base lot area, $\lambda_p = A_p/A_0$. Frontal density is calculated by the sum of all windward facing surfaces (red and green) projected on a plane normal to the streamwise direction then divided by the base lot area, $\lambda_f = A_f/A_0$. There are no differences between the red and green surfaces, the green surfaces were simply chosen to illustrate the area projection. Selected truncated cone windward facing surfaces in green illustrate the projection on the plane normal to flow in the figure 3.2(b) and (d) isometric views. All windward facing surfaces, regardless of whether it may be sheltered by upstream elements, are included in the frontal density calculation. As seen in 3.2(d) for random plates, truncated cones were allowed to overlap on the base lot area. This causes a solid-surface occlusion of the front face of the leeward overlapping truncated cone. The occluded area is not included in the frontal density calculation as seen in the projection.

All truncated cone elements were identical, with geometry documented in figure 3.3. Truncated cone dimensions were selected to idealize a single barnacle. Understanding boundary layers over barnacle roughness is important for informing drag prediction models and understanding ship propulsion requirements. However, these truncated cone elements may also be a proxy for low mountainous terrain in the atmospheric boundary layer. Specific truncated cone ratios were selected based on detailed barnacle statistics from Spivey[79]. The ratio of height to base diameter is lower than the average reported by

Case	λ_p	λ_f	Effective slope	Mean, $\langle h \rangle$ (mm)	Standard deviation, σ_h (mm)	Skewness, s_k	Flatness
S10	0.098	0.040	0.079	0.16	0.59	3.956	18.0
S17	0.175	0.070	0.141	0.29	0.76	2.756	9.46
S39	0.393	0.159	0.317	0.64	1.03	1.409	3.52
S48	0.485	0.196	0.391	0.79	1.09	1.095	2.70
S57	0.565	0.228	0.457	0.93	1.13	0.869	2.26
S63	0.631	0.255	0.509	1.03	1.15	0.709	2.01
S70	0.698	0.282	0.564	1.14	1.15	0.561	1.84
S78	0.785	0.317	0.634	1.29	1.14	0.393	1.71
R10	0.098	0.040	0.079	0.16	0.59	3.921	17.7
R17	0.174	0.070	0.140	0.29	0.77	2.709	9.15
R39	0.392	0.155	0.310	0.68	1.07	1.311	3.20
R48	0.484	0.190	0.379	0.86	1.14	0.960	2.36
R57	0.565	0.220	0.440	1.03	1.18	0.690	1.91
R63	0.630	0.243	0.486	1.16	1.20	0.498	1.69
R70	0.697	0.266	0.532	1.31	1.21	0.294	1.54
R78	0.785	0.296	0.591	1.53	1.19	0.035	1.51

Table 3.1: Test surface statistics

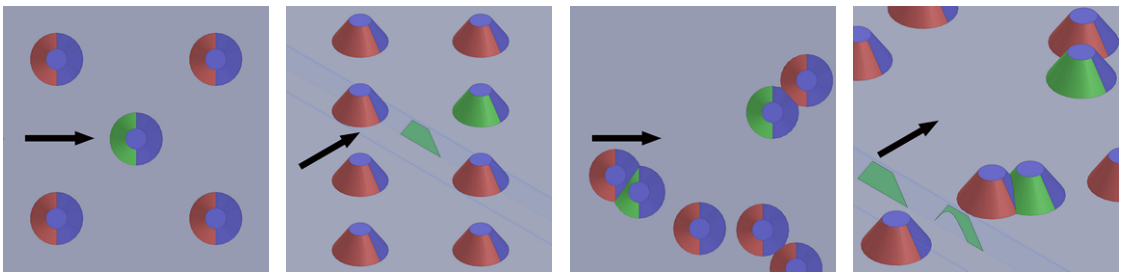

(a) **(b)** **(c)** **(d)**

Figure 3.2: Figures illustrate the planform and frontal density calculations in (a) a staggered surface top view, (b) a staggered surface isometric view, (c) a random surface top view, and (d) a random surface isometric view. Black arrows indicate the streamwise direction. Red and green highlight windward facing surfaces that are all included in the frontal area calculation. The green surfaces were selected to illustrate the frontal area projection, A_f, and have corresponding green projections that illustrate A_f. The blue highlights wall-normal and leeward surfaces that are included in the planform area, A_p, but not the frontal area, A_f.

Spivey[79] but still falls within the standard deviation. Also, experimental and computational fluid dynamic studies which focused on barnacle elements were reported by Schultz et al.[76] and Sadique[69]. These studies measured barnacles with an average of $k = 0.49D$ and $k = 0.37D$ respectively, where D is the base diameter and $k = \max(h)$ is the uniform height of the roughness crests. The ratio studied here falls between these two values.

3.2.3 Laser Doppler velocimetry measurements

Detailed boundary layer velocity statistics were recorded with a TSI FSA3500 two-component laser Doppler velocimetry (LDV) system. A custom beam displacer and beam expander produce ellipsoidal measurement volumes that have a

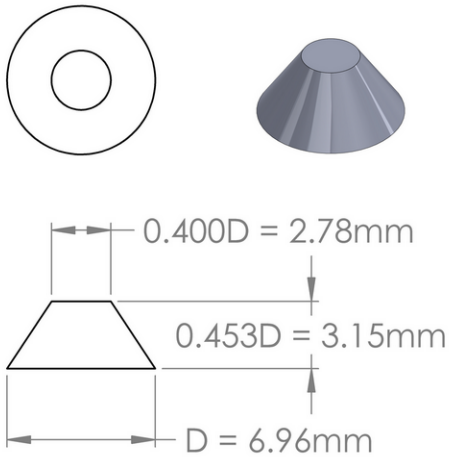

Figure 3.3: Truncated cone dimensions

beam waist of $45\,\mu$m. The flow was seeded with $2\,\mu$m diameter silver coated glass spheres. For the square staggered cases, wall-normal profiles were recorded at nine locations over a repeating unit as seen in figure 3.4. Each profile contained 50 sampling locations in the wall-normal direction where velocity data were recorded for 180 seconds. The nine locations were representative of the entire repeating unit by utilizing mirroring and translation. Then, an area-weighting was used to create a spatial-averaged profile for all time-averaged statistics. For the random cases, 12 wall-normal profiles were recorded and spaced at $1.5D$ across the span of the tunnel. The red profiles in figure 3.5 show these 12 locations. The spacing and number of profiles allowed independent profiles and well-converged spatial averages across the span. Additional wall-normal profiles were performed for the R17 and R39 cases with 23 profiles spaced at $0.75D$ since these cases appeared less well-converged when using 12 profiles.

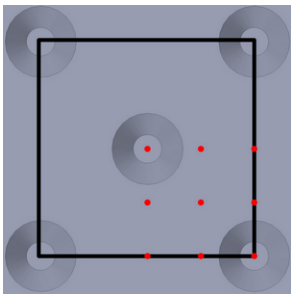

Figure 3.4: Profile locations over the staggered surface repeating unit. Red dots indicate profile locations. The black box indicates the repeating unit. Flow is from left to right.

The additional 11 profiles for these test cases are depicted in blue on figure 3.5. Each of the 12 or 23 profiles contained 50 sampling locations in the wall-normal direction where velocity data were recorded for 150 seconds. All time-average statistics were calculated using a virtual saturable-detector scheme. Due to the amount of data sampled, all of these tests were over 24 hours in duration.

3.2.4 Stereoscopic particle image velocimetry measurements

In order to investigate mean flow structures indicated in the LDV measurements, stereoscopic particle image velocimetry (PIV) measurements were employed in the wall-normal spanwise (y, z) plane at roughly the same downstream location as the LDV measurements. Measurements were recorded over the least dense and most dense cases for both staggered and random surfaces (S10, S78, R10, R78).

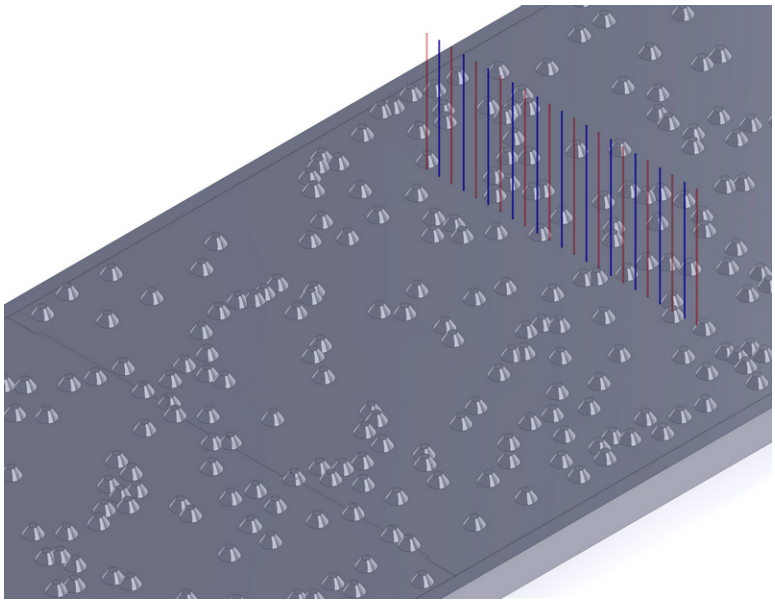

Figure 3.5: Profile locations over the random surfaces. Red profiles were recorded on all random surfaces. Blue profiles were also recorded over the R17 and R39 surfaces. Flow is from left to right.

For each surface, a wall-normal spanwise plane was acquired centered at the spanwise center of the test section. The flow was seeded with the same particles used in the LDV measurements. For each plane, 1000 image pairs were acquired using two CCD cameras with 3320 $\times$ 2496 pixel arrays. Velocity vectors were obtained with TSI Insight 4G software using 32 pixel square windows with 50% overlap. The field of view was 81 mm$\times$ 40 mm in the spanwise and wall-normal directions respectively.

3.3 Spatial-averaged results

This section presents spatial-averaged results over all staggered and random truncated cone surfaces. Spatial averaging is computed over the basic repeating tile for the staggered cases and in the spanwise direction for the random cases. Friction velocity, roughness length, and zero-plane displacement are determined through the planform density parameter space and trends are discussed. Two *a priori* drag prediction models are evaluated against the results, which should also inform future drag prediction algorithms. The section concludes by highlighting differences between turbulent boundary layer profiles and parameters between the staggered and random surfaces which indicated a breakdown in outer-layer similarity.

3.3.1 Spatial-averaged boundary layer profile results

Spatial-averaged experimental boundary layer profiles were analyzed with the comprehensive shear stress (CSS) method described in Womack et al.[96]. The comprehensive shear stress method calculates several important turbulent boundary layer parameters appearing in the log-law equation, which allow comparison between the boundary layers over rough surfaces. The log-law

equation with the wake function is

$$U^+ \equiv \frac{U}{u_\tau} = \frac{1}{\kappa} \ln\left(\frac{y-d}{y_0}\right) + \frac{\Pi}{\kappa} W\left(\frac{y}{\delta}\right). \tag{3.1}$$

In this equation, U is the mean streamwise velocity. The velocity scaling parameter is the friction velocity, u_τ, and the $+$ superscript indicates normalization by u_τ. $\kappa = 0.384$ is the Kármán constant used throughout this study with corresponding smooth-wall intercept, $A = 4.17$. Zero-plane displacement, d, is a shift in the effective origin of the log-law due to roughness. y_0 is known as the the roughness length and is related to the roughness function by $\Delta U^+ = A + (1/\kappa)\ln(y_0 u_\tau/\nu)$ or to equivalent sand-grain roughness by $k_s = y_0 e^{8.5\kappa}$ [34;9;13]. Friction velocity (u_τ), wall shear stress (τ_w), and skin friction (c_f), will all be used interchangeably based on application and are related by definition $u_\tau \equiv \sqrt{\tau_w/\rho} \equiv U_e\sqrt{c_f/2}$, where U_e is the free stream velocity and ρ is the fluid density.

The wake function, $W(y/\delta)$, models the outer-region deviation from the log-law and scales with the boundary layer thickness. This study will use the most common definition of the boundary layer thickness, δ, namely the wall-normal distance where velocity reaches 99% of the free stream velocity (so that $U(\delta) = 0.99U_e$). The wake strength parameter, Π, measures the strength of the deviation by $\Pi = \frac{\kappa}{2}\max[U^+(y) - \frac{1}{\kappa}\ln(y/y_0)]$.

The extended Volino and Schultz equation is a reformulated total shear

stress balance and was fit in the range of $0.15 < (y-d)/(\delta-d) < 0.30$ to determine u_τ, and the log-law equation was fit in the range of $0.07 < y/\delta < 0.15$ to determine y_0 and d in each iteration[88;96]. An iterative solution process is required since both equations have dependencies in all three variables. The convergence criteria for each profile were three significant digits in u_τ, y_0, and d or 10 iterations. Table 3.2 contains results from the comprehensive shear stress method as well as other relevant profile parameters for each surface's average profile. Displacement thickness, δ^*, and momentum thickness, θ, were calculated assuming a no slip condition at the wall ($u|_{y=0} = 0$) which adds an data point for the trapezoidal-rule numerical integration.

Friction velocity is one of the most important parameters to determine. The comprehensive shear stress method determines friction velocity indirectly, so it is prudent to check results against expectations. Figure 3.6 shows the spatial-averaged LDV results for skin friction plotted against the skin friction law first derived by Clauser[15] and Rotta[68] from the log-law equation. The skin friction law can be written, as in Castro[9], as

$$\sqrt{\frac{2}{c_f}} = -\frac{1}{\kappa}\ln\left(\frac{1}{H}\sqrt{\frac{c_f}{2}}\right) + \frac{1}{\kappa}\ln\left(\frac{\theta}{y_0}\right) + \frac{2\Pi}{\kappa} - \frac{1}{\kappa}\ln\left(\frac{1+\Pi}{\kappa}\right) \tag{3.2}$$

and provides a relationship between skin friction and the momentum thickness normalized by roughness length. H is the shape factor defined as $H = \delta^*/\theta$.

Case	Re_τ	U_e (m/s)	u_τ (m/s)	δ (mm)	δ^* (mm)	θ (mm)	$\frac{d}{k}$	$\frac{y_0}{k}$	$\frac{k}{\delta - d}$	k_s^+	Π
S10	2090	1.253	0.068	32.1	8.6	4.5	0.40	0.027	0.102	151	0.53
S17	2410	1.251	0.072	34.8	9.9	5.1	0.36	0.048	0.094	286	0.60
S39	2780	1.255	0.075	38.3	11.7	5.8	0.29	0.094	0.084	578	0.75
S48	2750	1.254	0.076	38.0	11.7	5.8	0.44	0.091	0.086	563	0.73
S57	2680	1.251	0.076	37.7	11.6	5.6	0.58	0.081	0.088	500	0.68
S63	2640	1.256	0.074	37.8	11.8	5.7	0.59	0.080	0.088	484	0.74
S70	2490	1.253	0.073	37.0	11.6	5.6	0.66	0.070	0.090	410	0.73
S78	2490	1.249	0.073	36.5	11.8	5.6	0.62	0.081	0.091	481	0.79
R10	2110	1.258	0.069	32.1	8.3	4.5	0.40	0.026	0.102	145	0.51
R17	2420	1.255	0.074	33.7	9.4	4.9	0.16	0.054	0.095	327	0.61
R39	3050	1.253	0.082	38.5	11.1	5.7	0.23	0.098	0.083	654	0.52
R48	2830	1.252	0.078	37.7	11.4	5.6	0.44	0.091	0.087	582	0.62
R57	2800	1.252	0.078	38.1	11.5	5.6	0.59	0.082	0.087	524	0.59
R63	2840	1.254	0.079	37.8	11.5	5.7	0.53	0.083	0.087	538	0.56
R70	2730	1.253	0.078	36.5	11.4	5.5	0.46	0.094	0.090	602	0.66
R78	2680	1.258	0.075	37.8	11.3	5.6	0.58	0.068	0.088	419	0.62

Table 3.2: Experimental profile parameters for spatial-averaged LDV measurements

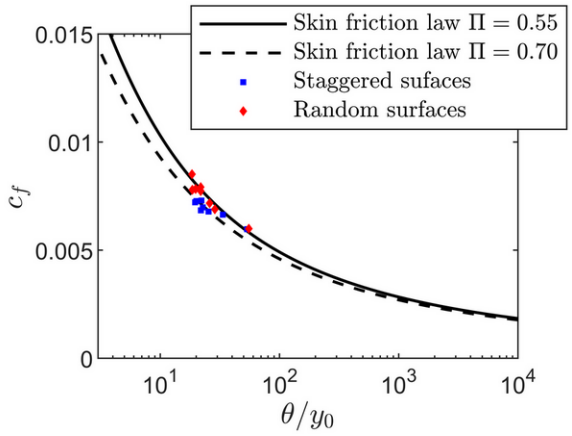

Figure 3.6: c_f as a function of θ/y_0 for all surfaces

The two plotted curves, one with $\Pi = 0.55$ and one with $\Pi = 0.70$, require an assumed wake function to solve for shape factor and are described in detail in Castro[9] and Womack et al.[96]. The random cases' results are observed to be closer to the $\Pi = 0.55$ curve, and the staggered cases' results tend to lie closer to the $\Pi = 0.70$ curve. This is consistent with the wake strength results found in table 3.2 which shows the random cases tend to have results near $\Pi = 0.55$ and the staggered cases tend to have higher wake strengths in the spatial-averaged profiles.

Inner-normalized spatial-averaged mean streamwise velocity profiles are plotted in figure 3.7. Figure 3.7(a) shows the staggered cases, and figure 3.7(b) shows the random cases. The dashed black line shows the smooth wall log-law. All profiles show the expected downward shift due to roughness effects. The S10, R10, S17, and R17 cases have clearly less downward shift than the other cases, which plot together more closely. All sixteen average profiles exhibit a log-linear

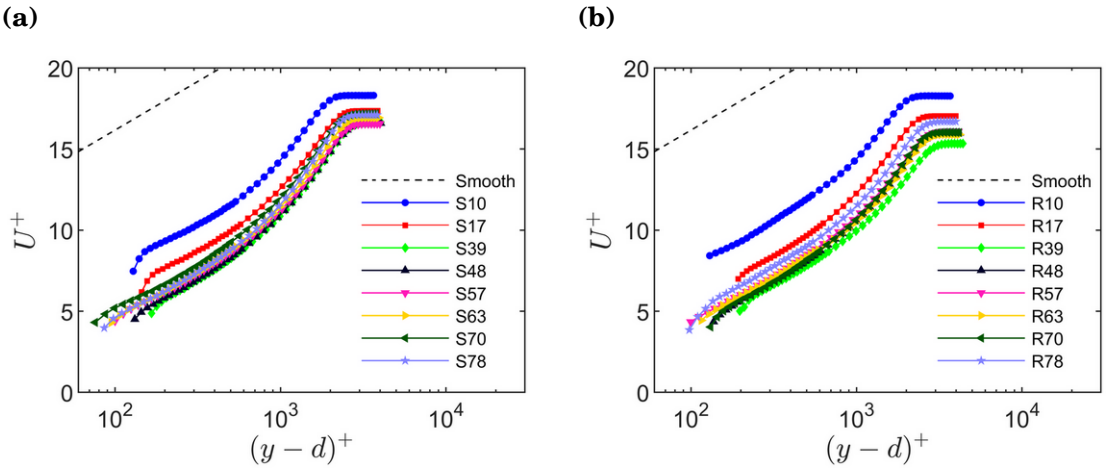

Figure 3.7: Mean streamwise velocity profiles in inner scaling for (a) staggered surface profiles and (b) random surface profiles.

region with slope of about $1/\kappa$ between approximately $0.07 < y/\delta < 0.15$. The existence of a linear region in the spatial-averaged profile with this roughness height to boundary layer thickness ratio or larger has been seen in other recent studies such as Cheng and Castro[12], Placidi and Ganapathisubramani[61,62], and Yang et al.[100] among others. The process for solving y_0 and d assumed this linear region existed, however the extent of such a region is not necessarily guaranteed in all cases.

Figure 3.8 shows inner-normalized spatial-averaged mean Reynolds shear stress profiles for all sixteen cases. Staggered cases are in figure 3.8(a), and random cases are in figure 3.8(b). The profiles appear consistent with data from other rough surfaces such as Cheng and Castro[12], Flack et al.[22], Flack and Schultz[20], and Placidi and Ganapathisubramani[61,62]. However, there are notable differences between the cases in the near-wall region, $(y-d)/(\delta-d) <$

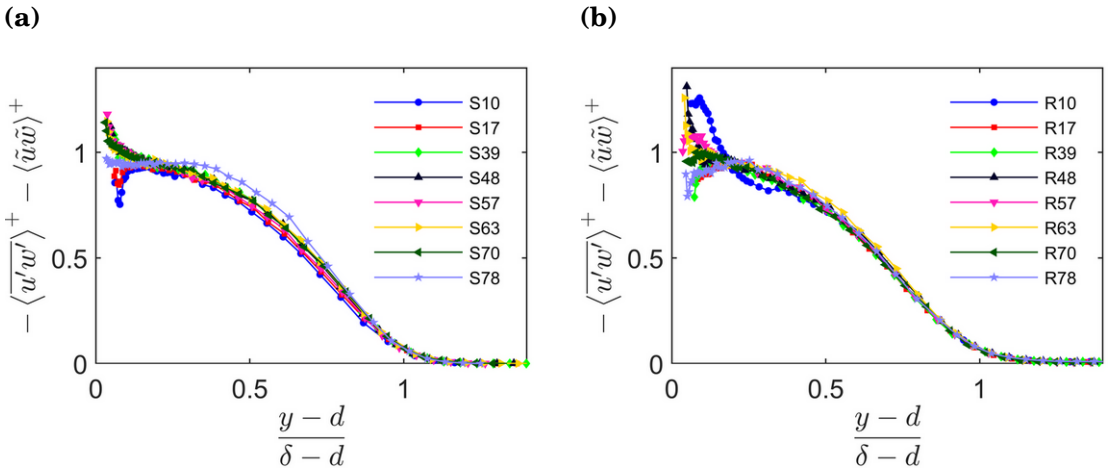

Figure 3.8: Turbulent shear stress profiles in inner scaling for (a) staggered surface profiles and (b) random surface profiles.

0.15. This is attributed to the significant spatial-heterogeneity found in this turbulence statistic in the roughness sublayer defined as the region where local Reynolds shear stresses differ by greater than 10%. Flack et al.[22] and Placidi and Ganapathisubramani[61] both report that the roughness sublayer in their experiments extended up to $y \approx 5k$. It is likely that the nine profiles of the staggered cases and twelve (or 23) profiles of the random cases do not provide a fine enough resolution to capture a well-converged spatial-averaged Reynolds shear stress in this region. The comprehensive shear stress method, which was used to calculate u_τ, y_0, and d, avoids uncertainty in the region by only fitting the extended Volino and Schultz equation to Reynolds shear stress and dispersive shear stress in the range of $0.15 < (y-d)/(\delta-d) < 0.30$.

Reynolds number independence of the rough surface drag was not checked directly, however several important reviews consider roughness results Reynolds

number independent when $k_s^+ \gtrsim 100$[65;34;21]. Table 3.2 shows that all cases from this study are at least 45% greater than this threshold, so Reynolds number independence is expected and y_0 and k_s are solely a function of the surface roughness.

Normalized roughness length, y_0/k, as a function of planform density, λ_p, was investigated and results are plotted in figure 3.9. Normalized roughness length for staggered and random cases at equivalent planform densities plot closely together for all but one density, $\lambda_p = 0.70$. Specific selection of the linear range used to fit the log-law equation is the largest source of error for determination of these average profile parameters. Therefore, error bars were generated by varying the region in which the linear regression was fit to the log-law during iteration in the comprehensive shear stress method. Those assumed linear regions also fit in the comprehensive shear stress method were: $0 < y/\delta < 0.15$, $0.10 < y/\delta < 0.15$, $0 < y/\delta < 0.19$, $0.07 < y/\delta < 0.19$, and $0.10 < y/\delta < 0.19$. As noted by Placidi and Ganapathisubramani [61] and Womack et al. [96], fitting of equation 3.1 for y_0 and d carries significant uncertainty, however it is still common to use a fitting procedure due to lack of a better alternative. Additionally, using a consistent fitting procedure allows for comparison among cases which provides valuable insight into roughness length trends. Varying the region in which the extended Volino and Schultz equation was fitted had a much smaller effect and was not included in the results presented here.

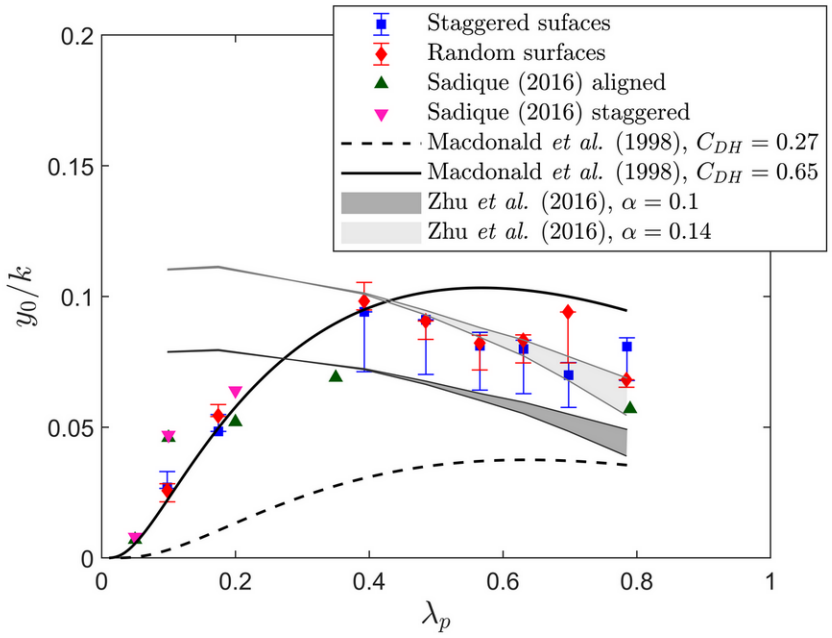

Figure 3.9: Normalized roughness length, y_0/k, as a function of λ_p. Data from Sadique[69] are obtained from table 3.6 in section 3.2.2.2 of the thesis.

Since staggered and random cases plot so close together, the results suggest that normalized roughness length is more a function of the density and element shape rather than their particular arrangement. This may be due to relatively comparable average distances between elements at each density in the staggered and random configurations. The correlation could break down if there was significant element clustering at the same density. Truncated cone surfaces tested in this study show increasing normalized roughness length between $0 < \lambda_p \lesssim 0.4$. Then a gradual decrease above $\lambda_p \gtrsim 0.4$. To the authors' knowledge, the only truncated cone data that provide comparison over a range of planform densities are found in Sadique[69]. He conducted large eddy simulations over staggered and aligned truncated cones at several planform densities. The

comparison study's repeating truncated cone had height, $k = 0.5D$, and plateau diameter, $0.5D$, making it slightly taller and wider than the truncated cone in this study. The results compare well with the present study given the differences in truncated cone shape. The normalized roughness length magnitudes are generally consistent, and if a curve where drawn though these points, it would seem to indicate a peak normalized roughness length around $\lambda_p \approx 0.4$ as the current experimental data suggest.

Most other studies which have systematically varied planform density have used cubes, rectangular prisms, or rectangular LEGO® blocks including Hall et al.[27], Cheng et al.[11], Hagishima et al.[26], Placidi and Ganapathisubramani[61], [62], Yang et al.[100], and Zhu et al.[101]. Most of these studies suggest a peak drag at a density of $\lambda_p \approx 0.15$ and marked drop in drag at higher densities, so the curve shape is not similar to the results reported here or in Sadique[69]. Additionally, most *a priori* analytical models were designed and evaluated against these rectangular prism surface morphologies (often called urban-like roughness) and were not found to be easily adaptable to truncated cone surface elements.

A roughness length model in Macdonald et al.[44], however, was found to be adaptable to the truncated cone shape when provided an *a priori* estimate for the coefficient of drag, C_{DH}, and zero-plane displacement height, d. Two relevant coefficient of drag measurements were found in a literature survey. Sadique[69] reports $C_D = 0.23$ from DNS on truncated cones in a laminar boundary layer. C_D

corresponds with $C_{DH} = 0.27$ when using the Blasius laminar profile solution to estimate velocity at the roughness crests, U_H, from reported simulation details. Additionally, Schultz et al.[76] reported a coefficient of drag of $C_D = 0.52$ for natural barnacle specimens in a turbulent boundary layer. C_D corresponds with $C_{DH} = 0.65$ when using reported information to estimate U_H in a turbulent boundary layer. Details on the adaption of the Macdonald et al.[44] model and *a priori* estimation of d for truncated cones are included in appendix A.

Results for these two values of C_{DH} are shown in figure 3.9. The curve which utilizes $C_{DH} = 0.65$ performs well below $\lambda_p \approx 0.4$ but does not peak there as the experimental data suggest. Instead, it seems to calculate a fairly flat peak around $\lambda_p \approx 0.55$ which is above the measurements and outside of their uncertainty. The curve which utilizes $C_{DH} = 0.27$ consistently plots below the experimental results. This confirms that the model is sensitive to an accurate estimate of an individual element's coefficient of drag and limits the *a priori* reliability of the model on many surface morphologies where the coefficient of drag is not known well or roughness shapes are not consistent.

Surface statistical models provide another possible *a priori* prediction of normalized roughness length. These types of models have the advantage of not requiring estimation of surface parameters like C_{DH} and d. Zhu et al.[101] provides an explicit expression for y_0 as a function of the surface standard

deviation and skewness,

$$y_0\left(\sigma_h,\, s_k\right) = \begin{cases} \alpha\sigma_h\left(1+\beta s_k\right), & \sigma_h/\left\langle h\right\rangle < 1.15 \\ \\ \alpha\sigma_h\left(1+s_k\right)^{\beta}, & \sigma_h/\left\langle h\right\rangle \geq 1.15 \end{cases}, \tag{3.3}$$

where constants α and β are 0.1 and 0.9 respectively. The truncated cone surfaces tested in this study have a slightly different standard deviation and skewness at each density due to the overlapping truncated cones on the random plates. Therefore, this model produces a range of results for the planform densities tested. This range is plotted in figure 3.9 as the dark grey shaded area. Zhu et al.[101]'s equation seems to match the slope of the current experiments but underestimates normalized roughness length above $\lambda_p \gtrsim 0.4$. It also does not seem to capture the shape of the curve well and overestimates the normalized roughness length below $\lambda_p \lesssim 0.4$. For sparse distributions of individual elements, a simple calculation in the limit $\lambda_p \to 0$ shows that $\sigma^2 \to k^2\lambda_p$ while $s_k \sim \lambda_p^{-1/2}$. Thus the predicted y_0 based on the skewness s_k does not tend to zero when $\lambda_p \to 0$ but to a constant of the order k (for $\beta = 1$), consistent with the Zhu et al. results shown in Fig. 3.9.

Since equation 3.3 seems to match the shape of the profile and Zhu et al.[101] reports $\alpha \approx 0.1$, it seems reasonable to attempt to tune α for a better fit. Additionally, Zhu et al.[101] cites several studies where $0.1 < \alpha < 0.17$ bounds the reported values. Equation 3.3 yields a good fit to the data above $\lambda \gtrsim 0.4$ when

$\alpha = 0.14$ as seen by the light grey shaded area in figure 3.9.

Given the success of the Macdonald et al. and Zhu et al. models in different surface densities and their different underlying assumptions, it is reasonable to postulate that the truncated cone surface is exhibiting two different flow regimes. The Macdonald et al. model assumes a coefficient of drag for individual elements while the Zhu et al. attempts to characterize the surface with surface statistics. Below $\lambda_p \lesssim 0.4$ the flow is characteristic of flow around isolated elements, while above $\lambda_p \gtrsim 0.4$ the flow is characteristic of skimming flow over a rough surface with the transition happening at the point of peak drag. Such a transition was expected as this type of behavior has been observed before in other studies such as Grimmond and Oke[25] and Placidi and Ganapathisubramani[61]. However, proposed flow regime prediction parameters such as ratios of roughness height to average distance between elements are difficult to apply to truncated cones. The is due to their varying cross-section with height which gives rise to different flow behaviour as $\lambda_p \to 1$. Cubes tend to a smooth wall as $\lambda_p \to 1$ leading to skimming behavior whereas truncated cones remain a dense surface with evidence of limited sheltering at the tested dimensional ratios.

Normalized zero-plane displacement height, d/k, is plotted in figure 3.10. Based on flow physics and previous studies, it is expected that d/k increases with planform density Grimmond and Oke[25]. Such a trend is visible at larger λ_p while the trend is somewhat noisy at $\lambda_p < 0.4$.

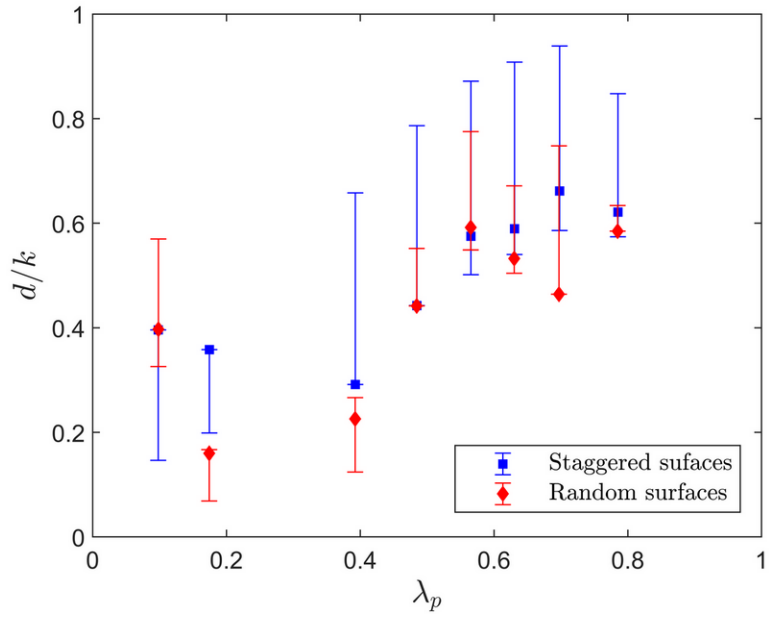

Figure 3.10: Normalized zero-plane displacement, d/k, as a function of λ_p

3.3.2 Differences in spatial-averaged staggered and random surface profiles

Local outer-normalized mean streamwise velocity profiles for the S78 staggered case are plotted in figure 3.11(a), and local outer-normalized mean streamwise velocity profiles for the R78 random case are plotted in figure 3.11(b). The spatial average is plotted with a thick black line. It is clear from figure 3.11(a) that the various S78 local profiles converge within one roughness height, k, above the roughness crests. Reynolds shear stress profiles (not shown) converge within $2k$ above the roughness crests. This is the result for all staggered cases and consistent with other studies that report convergence above $y > 5k$[22;61]. In

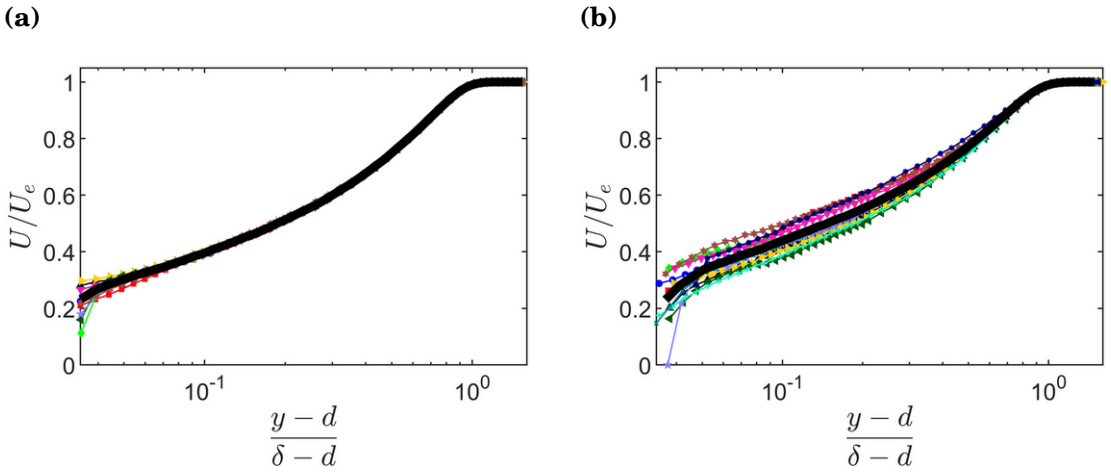

Figure 3.11: All outer-normalized (a) S78 local profiles and (b) R78 local profiles plotted in color. The thick black line is the spatial-average profile for the case.

contrast, figure 3.11(b) shows visual differences in the local profiles all the way to the edge of the boundary layer.

Inner-normalized mean streamwise velocity profiles in defect form are included for all staggered cases in figure 3.12(a) and for all random cases in figure 3.12(b). DNS at $\mathrm{Re}_\tau \approx 2000$ from Sillero et al.[78] is included as the thick black dotted line for reference in both plots. It can be observed that all staggered cases except S10 plot above the DNS reference in figure 3.12(a), and all random cases plot near the DNS reference in figure 3.12(b). Additionally, there is a greater visual spread in the profiles at low $(y-d)/(\delta-d)$ for the staggered cases when compared to the random cases.

Further evidence of the differences seen in figure 3.12 is seen in the column of Π values in table 3.2. For the staggered cases, wake strength ranges from $\Pi = 0.53 - 0.79$ compared with $\Pi = 0.51 - 0.66$ for the random cases, and the

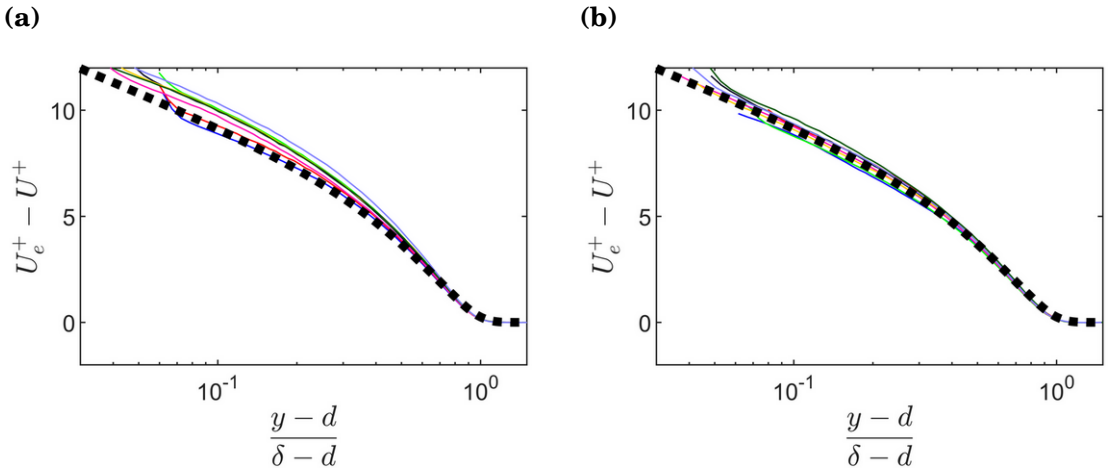

Figure 3.12: (a) Staggered surface profiles and (b) random surface profiles shown in inner-normalized mean streamwise velocity defect form. The thick dotted black line is the smooth-wall DNS result at $\mathrm{Re}_\tau \approx 2000$ from Sillero et al.[78].

differences in wake strength are largely outside of the experimental uncertainty when compared at similar λ_p as seen in figure 3.13(a). Additional comparison with other surface morphologies such as the mesh, cubes, rectangular blocks, and sand-grain surfaces from Castro[9] in figure 3.13(b) reveals that the staggered cases seem to show wake strengths commensurate with the roughness function. However, the random cases appear to have reduced wake strength by comparison.

Notably, the observations in figures 3.12 and 3.13 were formed on spatial-averaged profiles. However, there was significant spatial variation across the horizontal tunnel span (z-direction) on all random surface cases that was illustrated by the R78 case in figure 3.11(b). In contrast, the staggered surface cases, as shown in the S78 case in figure 3.11(a), showed variation only in the

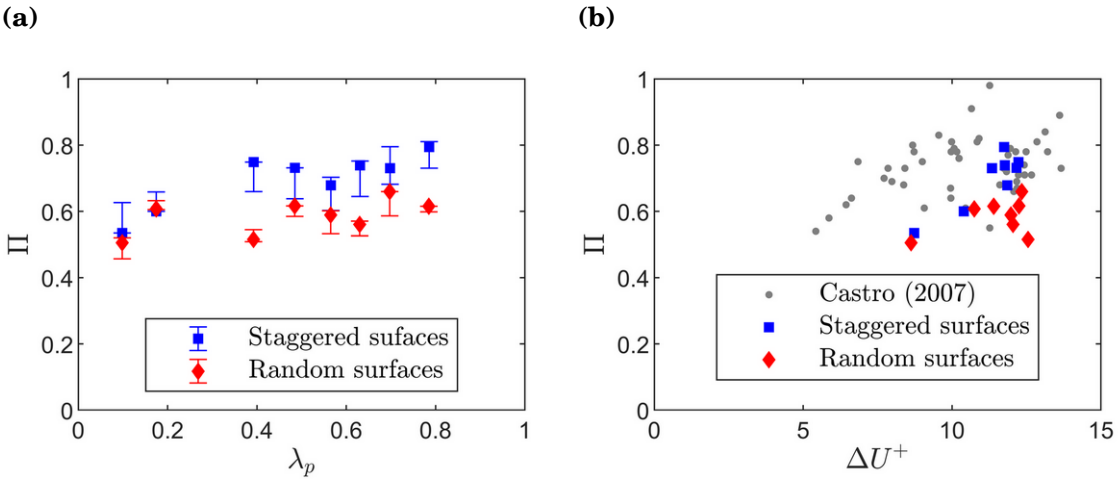

Figure 3.13: Plots of wake strength, Π, as a function of (a) planform density, λ_p, and (b) roughness function, ΔU^+, for staggered and random surfaces

near wall region consistent with other studies[65;34;21;2]. The lack of collapse of the profiles in figure 3.11(b) outside of the inner layer is striking given that all of these profiles were recorded over a similar surface at the same Reynolds number, $\mathrm{Re}_x = U_e x/\nu$. Taken together, these observations indicate a breakdown in outer-layer similarity warranting further analysis. In section 3.4, it will be shown that these differences can be attributed to secondary flows which create high momentum pathways and low momentum pathways and disrupt outer-layer similarity.

3.4 Secondary flow structures and their characteristics

This section presents an analysis of the deviations from outer-layer similarity and the secondary flow structures that generate high and low momentum pathways observed to occur over the random truncated cone surfaces. Section 3.4.1 shows evidence of HMPs and LMPs over the present random surfaces, consistent with observations from previous studies. However, evidence for HMPs and LMPs appears much weaker for flow over the staggered surfaces. This stands in contrast to previous studies where spanwise flow heterogeneity is normally observed over surfaces with spanwise roughness periodicity. Section 3.4.2 attempts to correlate local surface elevation with the momentum pathways. Section 3.4.3 discusses the relationship between present observations and prior theories of sustainment of momentum pathways and posits a mechanism of sustainment based on spanwise flow heterogeneity instead of surface roughness heterogeneity. Section 3.4.4 compares local turbulent boundary layer profiles with measures of turbulent boundary layer universality. Lastly, section 3.4.5 examines turbulent shear stress differences in HMPs and LMPs through quadrant analysis and compares with other reported data.

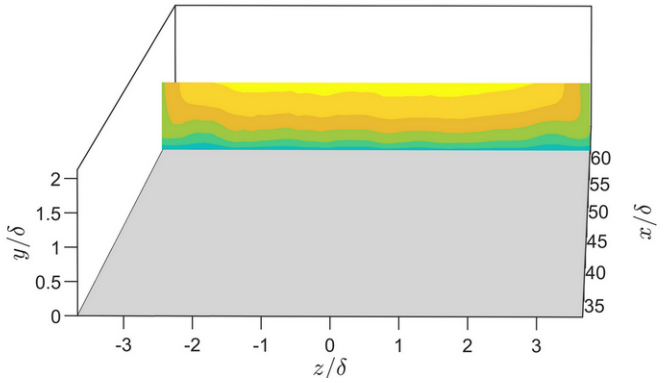

Figure 3.14: Mean streamwise velocity contour plot of the wall-normal spanwise plane at the measurement location on a smooth wall surface

3.4.1 Evidence of secondary flow structures

Figures 3.14 and 3.15 show the wall-normal spanwise plane of mean streamwise velocity at $x = 1.50\,\text{m}$ surveyed with the LDV. Figure 3.15(a)-(g) shows contour plots created from the 12 or 23 profiles described in section 3.2.3 and shown in figure 3.5, and plots in figures 3.14 and 3.15(h) show surveys of the entire tunnel span with linear grid spacings in the wall-normal and spanwise directions.

The smooth wall survey in figure 3.14 displays a typical smooth wall boundary layer developing in a rectangular tunnel. There are notable distortions in the corners as expected due to the square tunnel corners and a slight (1-2 mm or $\pm 0.04\delta$) thickening of the boundary layer near the middle of the span[55;56;64;31;29;30]. These are due to small tunnel-scale secondary flows typical of a tunnel with these dimensions and are generally considered negligible for most boundary

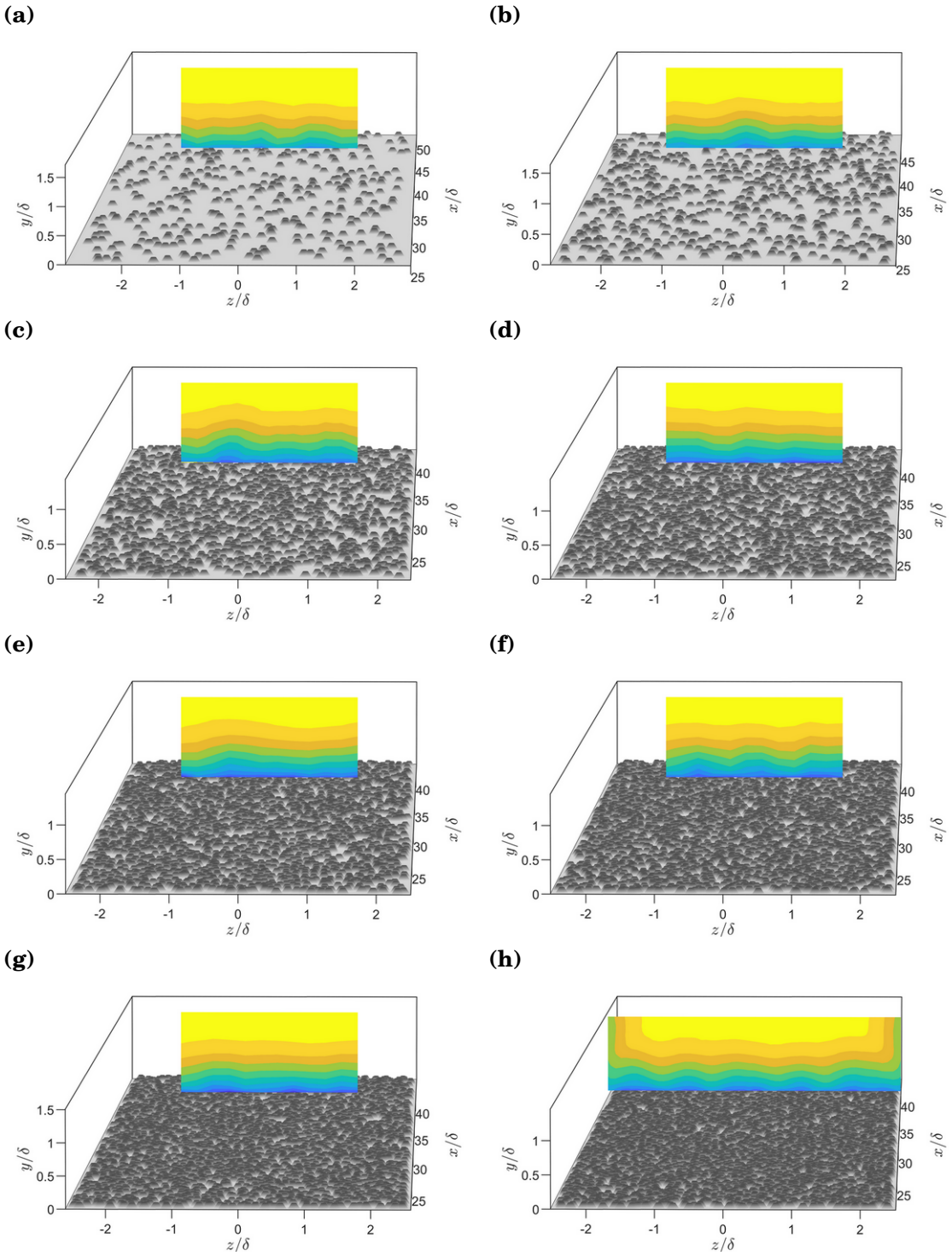

Figure 3.15: Mean streamwise velocity contour plots of the wall-normal spanwise plane at the measurement location over (a) R10, (b) R17, (c) R39, (d) R48, (e) R57, (f) R63, (g) R70, and (h) R78 surfaces.

layer results.

In contrast, all random cases shown in figure 3.15 display mean streamwise velocity heterogeneity across the tunnel span. The spanwise heterogeneity consists of alternating high momentum pathways and low momentum pathways. High momentum pathways and low momentum pathways exist in the time-averaged streamwise velocity and are different than high momentum regions and low momentum regions which are instantaneous flow features[50;5].

For further evidence of the marked difference in spanwise heterogeneity, figure 3.16 shows the standard deviation of U/U_e at $y/\delta = 0.25$ for all random cases and the smooth wall. The standard deviation is computed based on the differences between the local mean streamwise velocity and the spatial averaged mean velocity at the fixed height $y/\delta = 0.25$ and represents a quantitative measure of the spatial variability. It is essentially the square-root of the streamwise component of the dispersive stress. It is readily seen that the mean streamwise velocity standard deviation is an order of magnitude higher across the span for the random cases (figure 3.15) when compared with the smooth wall (figure 3.14). Also included is the standard deviation for the 9 profiles of each staggered case. These 9 profiles were not across the span but shows the difference in standard deviation across all truncated cone cases (i.e quantifies the difference between figure 3.11(a) and (b)). Finally, it is notable that there is no trend with respect to density evident in the standard deviation, which appears consistent

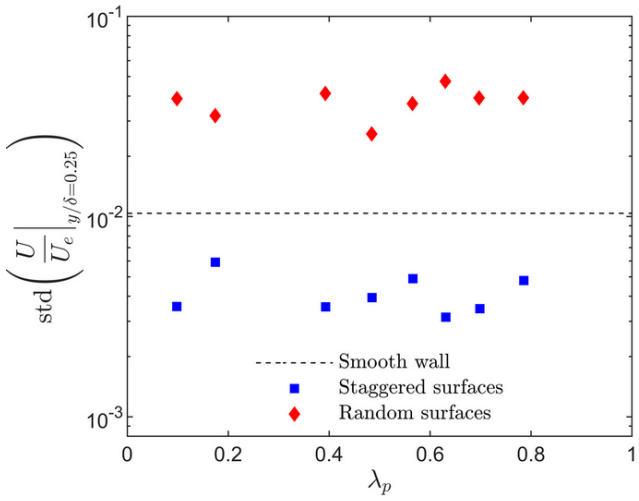

Figure 3.16: Mean streamwise velocity standard deviation at wall-normal distance $y/\delta = 0.25$.

with figure 3.15.

There are a few unique observations that can be gained from LDV measurements over these surfaces. Figure 3.17 shows three planes of mean streamwise velocity data for the R78 case. Each of these planes contains six profiles spaced $1.5D$ in the z-direction and centered in the span. The middle plane is located at $x = 1.50\,\mathrm{m}$ and is co-located with other wall-normal spanwise measurements. The upstream and downstream planes are located $\pm 8\,\mathrm{cm}$, approximately 2δ, from the center plane. The three planes show similar contours which indicates that these HMPs and LMPs exist over a streamwise distance of more than 4δ. It is noted that Mejia-Alvarez and Christensen[50] measured 1δ sustainment over their irregular surface. This indicates that the secondary flow structures creating the HMPs and LMPs are longer-standing than previously reported over

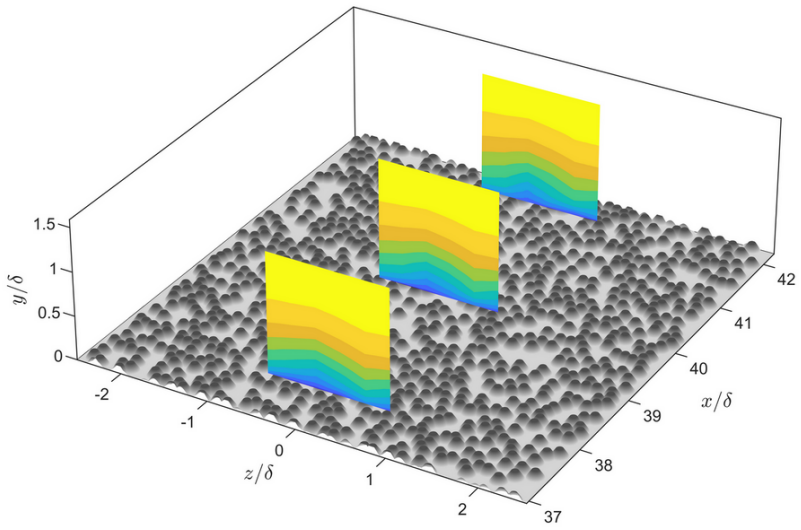

Figure 3.17: R78 mean streamwise velocity contour plot of three wall-normal spanwise planes in an isometric view. The center plane is at the normal measurement location, $x = 1.50\,\text{m}$. The windward and leeward planes are $\pm 8\,\text{cm}$, approximately $\pm 2\delta$, from the normal measurement location.

an irregular or random surface.

In figure 3.18(a), the repeatability of the results is examined by comparing results from different experiments over the same surface. The R78 case full-span linearly-spaced mean streamwise velocity from figure 3.15(h) is shown again in 2D in the upper plot. Overlaid in black is the R78 test which measured independently the 12 profiles also shown in figure 3.5. Overlaid in red on this figure are data contours from the co-located middle plane in figure 3.17 from yet a different experiment. This plot highlights the location repeatability of the HMPs and LMPs over these surfaces by showing that the HMPs and LMPs appear in the same locations on independent test runs.

Figure 3.18(b) shows the R78 case full-span Reynolds shear stress data. This

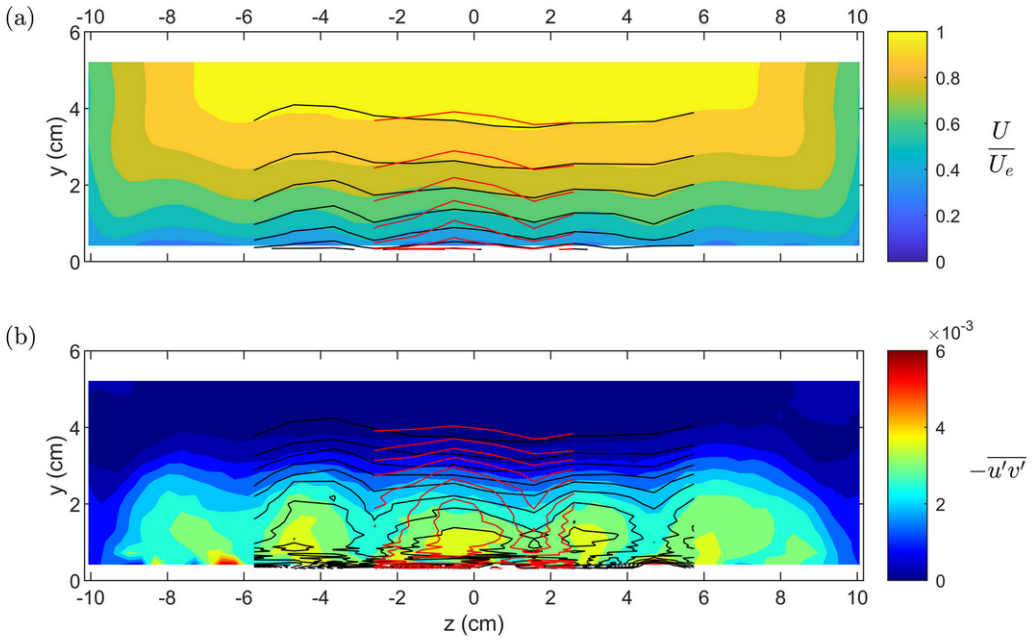

Figure 3.18: R78 surface (a) mean streamwise velocity and (b) Reynolds shear stress contour plots from three independent test runs at $x = 1.5\,\text{m}$.

plot gives further evidence of HMPs and LMPs since it demonstrates depressed and elevated levels of Reynolds shear stress coincident with HMPs and LMPs respectively as was shown in both Barros and Christensen[5] and Anderson et al.[3]. Again, the 12 profile test and the 6 profile test at $x = 1.50\,\mathrm{m}$ were overlaid in black and red respectively, and the elevated and depressed levels of Reynolds shear stress were measured in the same spanwise locations. The location repeatability across independent test runs suggests some correlation with the surface roughness which will be discussed in section 3.4.2.

Further measurements were acquired with stereo PIV in order to measure all three velocity components and also to compare staggered test surfaces and random test surfaces with the same measurement system on a subset of roughness density cases. The least dense and most dense cases were selected for these measurements. Figure 3.19 shows contour plots of outer-normalized streamwise velocity (U/U_e), signed swirling strength ($\overline{\Lambda_{ci}}\,(\delta/U_e)$), Reynolds shear stress ($-\overline{u'v'}/U_e^2$), and turbulent kinetic energy (tke/U_e^2) from R10, R78, S10, and S78, respectively (turbulent kinetic energy is defined as $tke \equiv (1/2)\,(\overline{u'^2} + \overline{v'^2} + \overline{w'^2})$. Signed swirling strength, $\overline{\Lambda_{ci}}\,(\delta/U_e)$, is a ensemble-averaged quantity, where $\Lambda_{ci} = \lambda_{ci}\,(\omega_x/\,|\omega_x|)$ and λ_{ci} is the imaginary portion of the complex-conjugate eigenvalue of the instantaneous velocity gradient tensor and is a frame-independent measure of the local rotation[1;5;84;85]. It is noted that $\overline{\Lambda_{ci}}$ represents the average of a small-scale turbulence quantity that may not

always be representative of large-scale vortex structures. However, it is used because $\overline{\Lambda_{ci}}$ is expected to be less prone to PIV bias errors (compared to e.g. the mean streamwise vorticity) and also since it has been used in prior studies[84;85].

R10 and R78 streamwise velocity contours plotted in figures 3.19(a) and (b) clearly show similar spanwise variations that were observed previously now in stereo PIV measurements and indicate alternating HMPs and LMPs. In contrast, the streamwise velocity for the staggered (regular) S10 and S78 cases is far more homogeneous in the spanwise direction. For the S10 case, the spanwise standard deviation of the outer-normalized mean streamwise velocity at $y/\delta = 0.25$ between $-1.3 < z/\delta < 1.3$ is 3.8×10^{-2} for the random case (R10) while it is only 1.7×10^{-2} for the staggered case (S10). For the 78% cases, the standard deviation values are 4.1×10^{-2} for R78 and only 1.5×10^{-2} for S78.

The signed swirl strength measurements shown in figures 3.19(e) and (f) exhibit spanwise heterogeneous variations with its peak values between and its sign change in the HMPs and LMPs (dashed lines). This is indicative of the δ-scale secondary flows which rotate clockwise in majority red and counter-clockwise in majority blue regions. These counter-rotations sweep high momentum fluid from higher in the boundary layer downward in the HMPs and eject low momentum fluid from deep in the boundary layer upward[5;3]. While the swirl strength measurements are affected to some degree by experimental error of the stereo PIV system, the differences visible between the random and

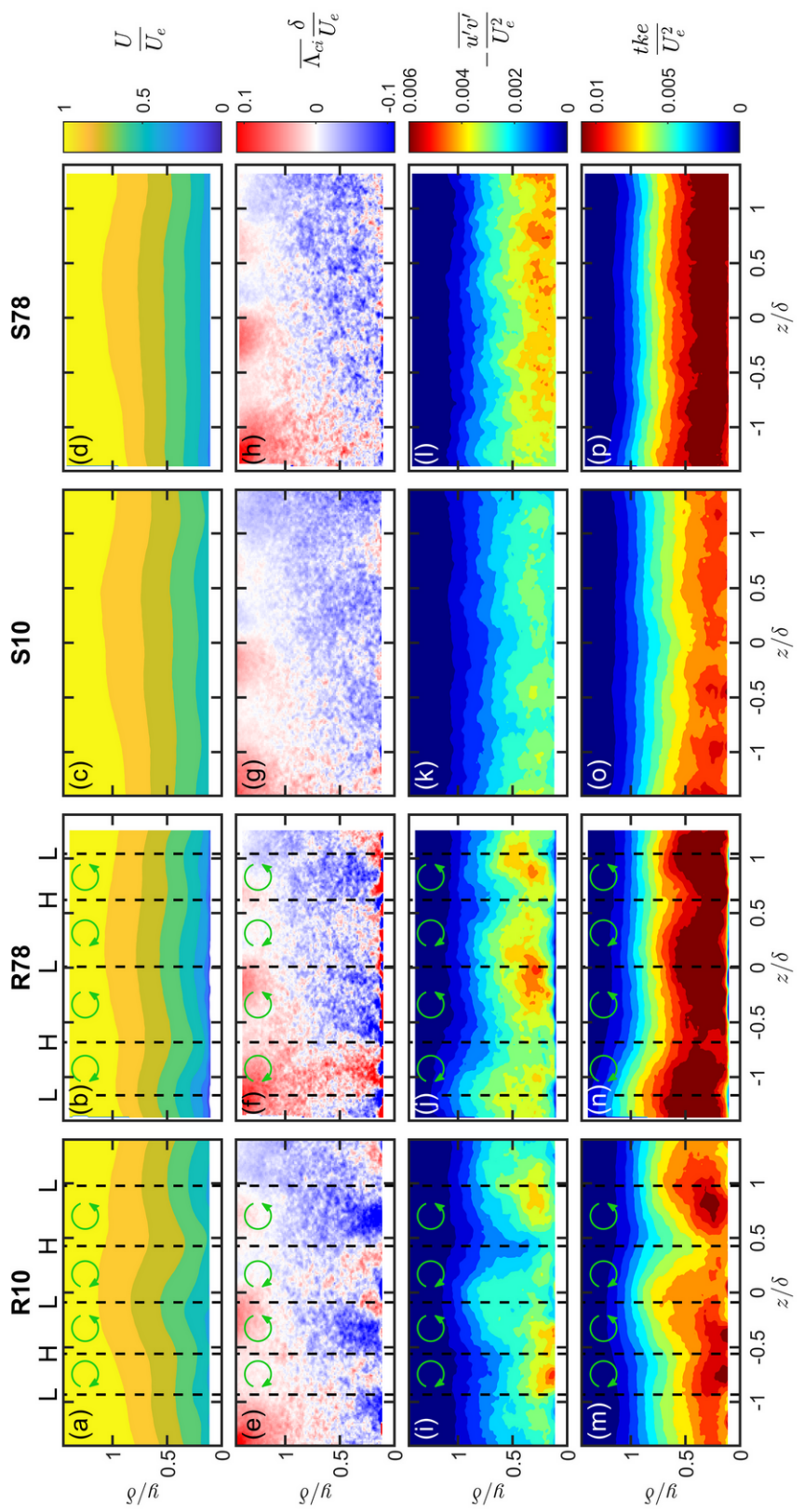

Figure 3.19: Stereo PIV data plots. Columns are (a,e,i,m) R10, (b,f,j,n) R78, (c,g,k,o) S10, and (d,h,l,p) S78 test surfaces. Rows are outer-normalized (a,b,c,d) streamwise velocity (U/U_e), (e,f,g,h) signed swirl strength ($\overline{\Lambda_{ci}}\,(\delta/U_e)$), (i,j,k,l) Reynolds shear stress ($-\overline{u'v'}/U_e^2$), and (m,n,o,p) turbulent kinetic energy (tke/U_e^2).

staggered cases are outside experimental error.

Lastly, Reynolds shear stress contour plots in figures 3.19(i) and (j) show reduced and enhanced Reynolds shear stress in the HMPs and LMPs respectively. And, turbulent kinetic energy contour plots in figures 3.19(m) and (n) show evidence of reduced tke and enhanced tke in the HMPs and LMPs respectively. Simulations in Anderson et al.[3] indicated that enhanced Reynolds shear stress and tke in the LMPs was a result of production at the surface (specifically below the HMPs) and advection into the LMPs rather than local production. As with the LDV results, the results based on present stereo PIV measurements are consistent with those of Barros and Christensen[5] and Anderson et al.[3].

3.4.2 Momentum pathway surface roughness correlations

One of the major topics concerning rough-wall boundary layer secondary flows and their resulting HMPs and LMPs has been their locations with respect to the underlying surface morphology. There is now a sizable set of parametric studies exploring these rough-wall boundary layer secondary flows over systematically-varied heterogeneous roughness. Chung et al.[13] provided a recent review of the findings with respect to spanwise spacing of roughness, and Medjnoun et al.[46] provided a recent review with respect to upwash and

downwash locations.

Surfaces with repeating roughness features have long been suspected of generating secondary flows which correlate with surface topography. However, in the present tests, the surfaces with repeating units (staggered) do not show evidence of δ-scale secondary flows. Recent parametric studies find that a minimum distance of $\delta/2$ was required for significant secondary flows to be generated[84;13]. Here the S10 case had staggered truncated cones spaced at $2D \approx 0.4\delta$ in the spanwise direction, and for the denser cases the spacing was smaller. Thus, the lack of observed secondary flows on the staggered cases is not inconsistent with results of Vanderwel and Ganapathisubramani[84].

Less commonly, secondary flows have been observed in a turbulent boundary layer over more complex roughness. A series of experiments were performed over a replicated turbine-blade damaged by deposition of foreign materials, and HMPs and LMPs were identified[97;98;49;50;5;58]. The surface studied by Christensen and colleagues was highly irregular. However, Barros and Christensen[5] identified that HMPs and LMPs appeared to form over relatively elevated and recessed terrain in the 1δ upstream fetch respectively. The surface correlation indicated that there was still δ-scale spanwise surface heterogeneity despite the complexity of the surface.

In an attempt to correlate HMPs and LMPs with upstream topography in this study, figure 3.21 shows HMP and LMP correlations with upstream topography

statistics for all random surfaces. Pane (*i*) in each subfigure 3.21(a)-(h) shows the outer-normalized streamwise velocity (U/U_e). HMPs and LMPs are indicated with red dashed lines in all panes. Below the streamwise velocity are graphical depictions of the upstream topography and spanwise surface height statistics from these topographies. Pane (*ii*) shows the outer-normalized low-pass-filtered spanwise roughness profile, η/δ, in blue for direct comparison with the findings of Barros and Christensen[5]. η is calculated by averaging the heights from a δ-long upstream fetch and then applying a Fourier cut-off filter at 0.125δ on the spanwise vector. Barros and Christensen[5] found HMPs and LMPs correlated with regions of relatively elevated and recessed upstream terrain respectively as indicated by the filtered height, η. Pane (*ii*) in each of figures 3.21(a)-(h) does not appear to show a consistent correlation with this statistic over these surfaces.

An alternate method of achieving a spanwise-smoothed plot of terrain elevation is to use a centered moving average with carefully chosen box widths. Pane (*iii*) shows the streamwise average height, h_x, of 1δ upstream fetch $x_0-\delta < x < x_0$ which is then spanwise-smoothed with both a moving average of $2D$ width, $\widetilde{h}_x$ (black), and $6D$ width, $\widehat{\widetilde{h}}_x$ (grey). Relatively high terrain is evident when $\widetilde{h}_x-\widehat{\widetilde{h}}_x > 0$ (black over grey), and relatively low terrain is evident when $\widetilde{h}_x-\widehat{\widetilde{h}}_x < 0$ (grey over black). Again, no consistent correlation of HMP and LMPs with terrain height appears.

It is not surprising that these statistics from δ-long upstream fetch do not correlate with HMPs and LMPs. In figure 3.17, it was noted that HMPs and LMPs remained in approximately the same spanwise locations for a 4δ fetch. This indicates that it is unlikely that statistics from only a 1δ fetch would be capable of generating and sustaining these turbulent boundary layer features. The R78 surface shows HMPs and LMPs but with little statistical variation across the span when averaging 4δ of upstream fetch (not shown). This suggests that these HMPs and LMPs are independent of the local upstream surface statistics. The remainder of this section will posit a possible initiation mechanism at the leading edge of the roughness, and section 3.4.3 will discuss a possible sustainment mechanism.

The leading edge of the roughness may provide a heterogeneous initiation mechanism independent of the more homogeneous spanwise surface statistics. The R10 plate in figure 3.21(a) gives an example of how this might occur in pane (*vi*) where flow is from bottom to top. As can be seen from the dashed red lines, HMPs appear to be aligned with the first truncated cones that the developing boundary layer encounters at the leading edge of the roughness, and the LMPs appear to aligned with flat topography for a longer fetch. This could initiate HMPs and LMPs by leading truncated cones shedding vortical structures when k is of $\mathcal{O}(\delta)$ or by generating locally higher tke as in Anderson et al.[3].

In order to quantify leading edge topography, pane (*v*) contains plots of $\widetilde{h}_x$

and $\widehat{\widetilde{h}}_x$ where, here, the h_x represents initial streamwise averaging of surface height in the first D/λ_p of leading roughness fetch ($x_r < x < x_r + D/\lambda_p$). The averaging length, D/λ_p, normalizes the area averaged to a similar number of truncated cones in each random case. The difference $[\widetilde{h}_x - \widehat{\widetilde{h}}_x]_{x_r<x<x_r+D/\lambda_p}$ is then a measure of leading edge roughness across the span in pane (v) on all cases.

Figure 3.20 shows the correlation coefficient between leading edge topography and U/U_e at $y/\delta = 0.25$ in blue circles. Also shown for comparison in red triangles is the correlation coefficient between 1δ upstream topography and U/U_e at $y/\delta = 0.25$. A positive correlation coefficient represents positive correlation between HMPs and relatively elevated terrain and LMPs and relatively recessed terrain. Figure 3.20 indicates that many test surfaces show little correlation with these measures. However, three surfaces, R10, R57, and R78, display a significant (above 0.5) positive correlation with leading edge topography above the threshold set by the other 13 correlations. While hardly definitive evidence, it is surprising that there would be any correlation at approximately 18δ downstream. Additionally, but anecdotally, it appears as though there may have been some drifting left or right on a few of the test surfaces yielding negligible statistical correlation even though the qualitative agreement is visually noticeable.

It is important to point out that experiments in Barros and Christensen[5] and the current experiments both employed a smooth-wall development length

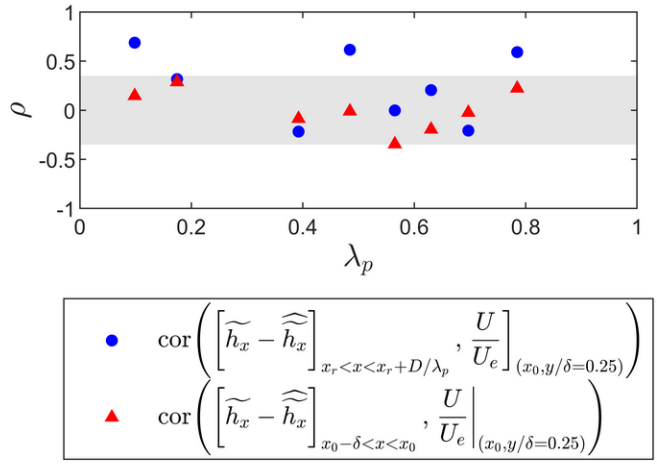

Figure 3.20: Correlation coefficients between streamwise velocity, U/U_e at $y/\delta = 0.25$, and leading edge topography in blue circles and 1δ immediate upstream fetch in red triangles.

for the boundary layer prior to the leading edge of the roughness. The current experimental series required 48 printed surfaces which required over 16 days of 3D printer usage. The smooth-wall development length was an attempt to mitigate the costs. Wu and Christensen[97], and presumably Barros and Christensen[5], attempted to mitigate the effect of the leading edge of the roughness by placing the mean height of the roughness at the same vertical level of the smooth-wall. That was not done in the present test series and the smooth-wall development was aligned with the truncated cone base plate. This may have played a role in HMP and LMP initiation in both studies.

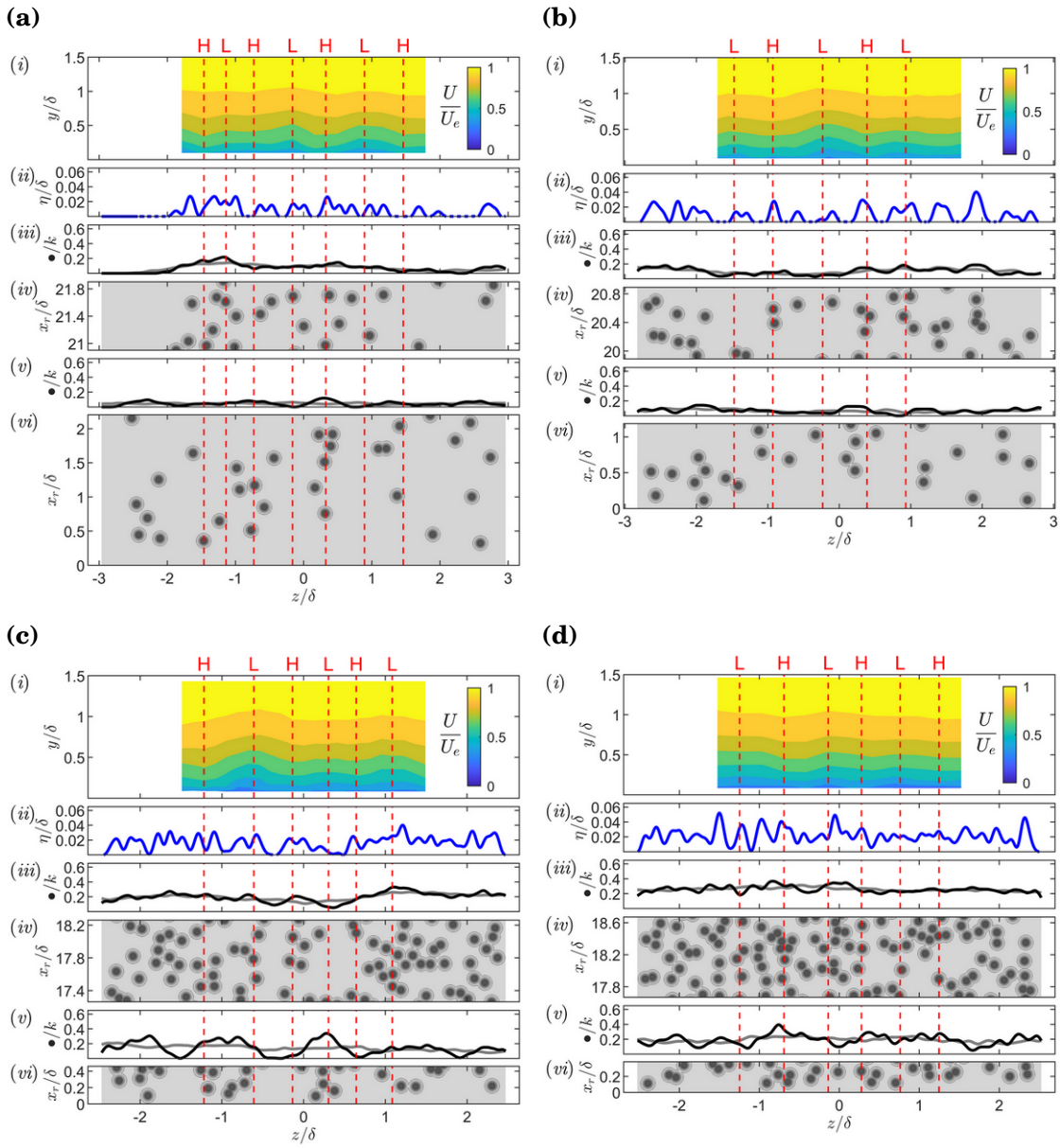

Figure 3.21: (a) R10, (b) R17, (c) R39, (d) R48, (e) R57, (f) R63, (g) R70, and (h) R78 surface correlations with HMPs and LMPs (continued on the next page). See the caption on the next page for a comprehensive figure description.

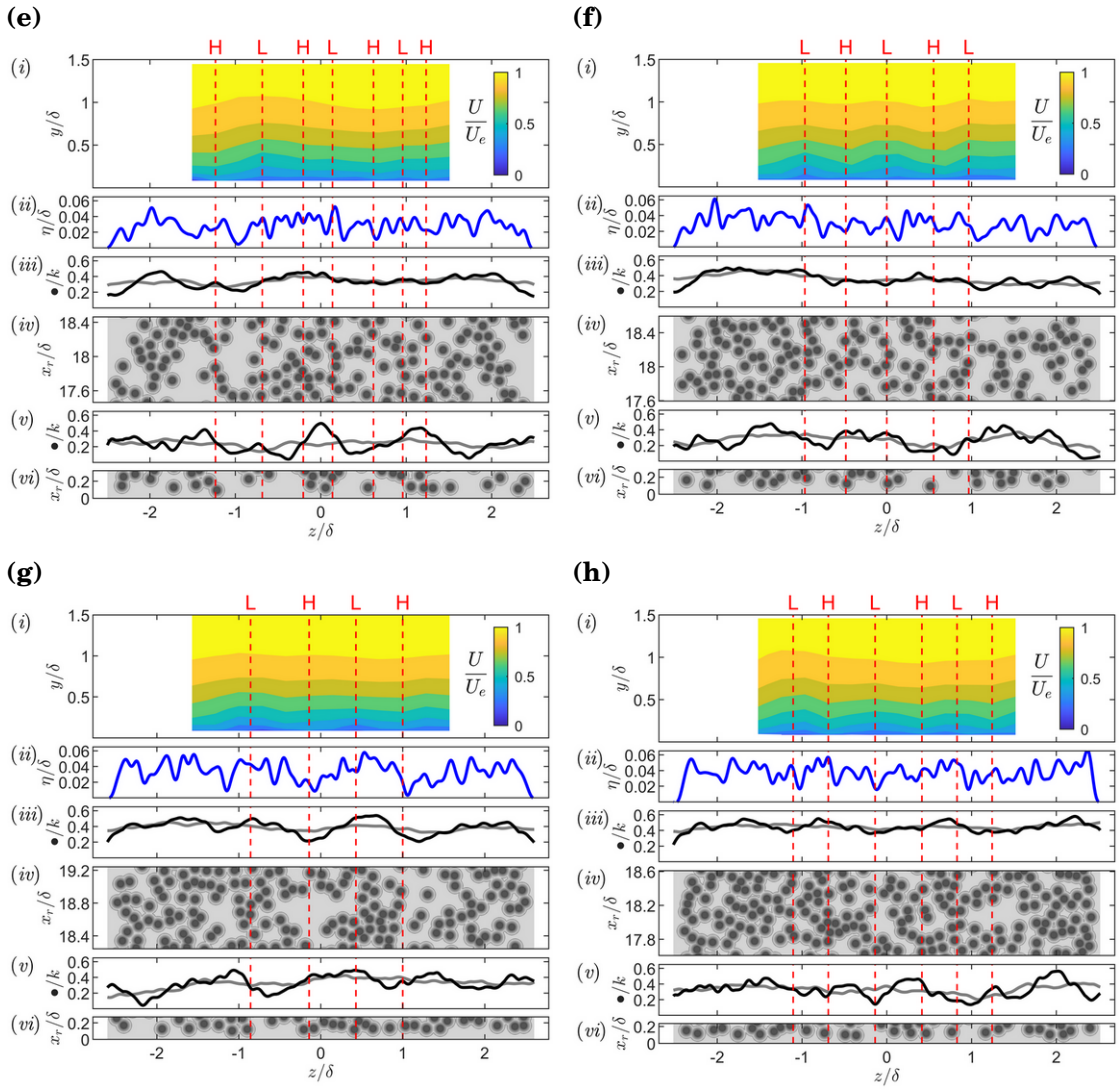

Figure 3.21: (a) R10, (b) R17, (c) R39, (d) R48, (e) R57, (f) R63, (g) R70, and (h) R78 surface correlations with HMPs and LMPs (continued from the previous page). Red dashed lines mark high and low momentum pathways with 'H' and 'L' respectively above the top pane. Plots are: (*i*) Outer-normalized streamwise velocity (U/U_e); (*ii*) Outer-normalized low-pass-filtered spanwise roughness profile, η/δ, in blue line; (*iii*) $\widetilde{h}_x/k|_{x_0-\delta<x<x_0}$ in black line and $\widehat{\widetilde{h}}_x/k|_{x_0-\delta<x<x_0}$ in grey line; (*iv*) Graphical depiction of the topography 1δ upstream of the measurement plane, $x_0 - \delta < x < x_0$; (*v*) $\widetilde{h}_x/k|_{x_r<x<x_r+D/\lambda_p}$ in black line and $\widehat{\widetilde{h}}_x/k|_{x_r<x<x_r+D/\lambda_p}$ in grey line; and (*vi*) Graphical depiction of the leading roughness topography from $x_r < x < x_r + D/\lambda_p$. x_0 is the location of the measurement plane, and x_r is the upstream start of the roughness field. Streamwise flow is from bottom to top over the graphical depictions of the surface.

3.4.3 Momentum pathway sustainment

The previous sections have established the presence of HMPs and LMPs over the random truncated cone surfaces and discussed correlation of those momentum pathways with the surface morphology. Section 3.4.2 suggested that these HMPs and LMPs were initiated at the leading edge of the roughness. However, the HMPs and LMPs were measured at an approximately 18δ fetch downstream of the roughness onset and developed over a surface with approximately spanwise homogeneous statistics over that long fetch. Some sustainment (or prolongation) mechanism must be at play to explain the observed HMPs and LMPs far downstream of the location of their initiation near the leading edge.

Studies by Hinze[29],[30] and Anderson et al.[3] have previously explained a mechanism that could be at work here although it was presented in a different context. In their derivations, Hinze[29] and Anderson et al.[3] both show that imbalances in tke production and dissipation near the wall in a turbulent boundary layer generate secondary flows. More precisely, when tke production exceeds dissipation in a localized region of a turbulent boundary layer, a secondary current of turbulence 'poor' fluid is induced that flows toward the high tke-production region. And, a secondary current of turbulence 'rich' fluid is induced out of the region[29] complying with the continuity equation. While it is known that tke production exceeds dissipation everywhere across the span near the wall, in their simulation data and the Barros and Christensen[5] experimental data, Anderson

et al.[3] show that the higher drag roughness generates relatively more tke. Thus the highest tke production-dissipation imbalance exists over the higher drag roughness. This imbalance induces a downward mean flow of turbulence 'poor' fluid into this location from above (along the highest tke gradient), and then a lateral mean flow of turbulence 'rich' fluid outward. Therefore, this is the localized mechanism which advects high momentum fluid from higher in the turbulent boundary layer downward creating a localized HMP and advects low momentum fluid from lower in the turbulent boundary layer upward creating adjacent LMPs. Both Hinze[29] and Anderson et al.[3] provide arguments based on the governing equations for this mechanism that need not be repeated here since the physical understanding is sufficient for the present study.

In the present study, there is no identifiable spanwise region of higher drag producing roughness (*i.e.* higher y_0 or k_s), but a spanwise gradient of streamwise velocity is imposed from the upstream condition instead. In this case, the spanwise regions of higher momentum fluid will tend to interact more strongly with the truncated cone roughness crests and create spanwise regions of locally higher form drag (skin friction, see section 3.4.4) and tke production. The previous studies have demonstrated that this would induce a mean secondary flow toward the wall in the HMPs and an outflow away from the wall in the LMPs, thus serving as a self-prolonging mechanism.

The plots in figures 3.19(m)-(p) are consistent with this physical under-

standing showing the highest wall-normal gradients of tke are in the HMPs (recognizing that the highest local tke above the roughness crests could not be resolved since they occur very near the crests (e.g. Sadique[69])).

3.4.4 Momentum pathway local boundary layer parameters and statistics

It is insightful to analyze the local profiles within a single random truncated cone test surface to observe the deviation from universality caused by the secondary flows. For this purpose, the comprehensive shear stress method[96] was applied to each local R78 profile individually to solve for local friction velocity, $u_{\tau,\mathrm{TSS}}$. The subscript 'TSS' indicates that the friction velocity was calculated from the local turbulent shear stress. For consistency, the zero-plane displacement, d, was fixed at the value calculated from the spanwise average (see table 3.2) during the CSS method iterative process.

Figure 3.22 shows each random surface's streamwise velocity contour plot (*i*) together with the friction velocity obtained (*ii*). It is readily apparent that the CSS method calculated lower and higher local friction velocities, $u_{\tau,\mathrm{TSS}}$, in the HMPs and LMPs respectively. Because the CSS method is heavily influenced by turbulent shear stress measurements, the calculated friction velocity is positively correlated with the enhanced and depressed local Reynolds shear

stress. However, this result is contrary to expectation. Fluid-dynamic drag imposed by the high k_s^+ truncated cone surface is expected to be largely form drag[12;34]. The higher velocity fluid in the HMPs would then be expected to transfer more momentum to the surface as it interacts with the roughness crests than the lower velocity fluid in the LMPs, leading to higher local friction velocity in the HMPs.

One might expect this to cast some doubt on the application of the CSS method in section 3.3, however the total wall stress is measured reasonably well in the spanwise average leading to an accurate result. Womack et al.[96] demonstrates that the spatial averaging of the streamwise momentum equation requires a dispersive stress term. Given the spanwise size of the measurement plane (including multiple HMPs and LMPs), the number of profiles in the spatial average, and the inclusion of the dispersive stress term, the additional error in the friction velocity calculation is expected to be small.

In order to investigate this issue further, an alternative method for calculating local friction velocity was also employed. The surfaces are statistically homogeneous, and many experiments have shown that the roughness length is characteristic of a particular surface[16;80;52]. Since the CSS method allowed accurate determination of surface roughness characteristics from the spanwise average profile in section 3.3, roughness length and zero-plane displacement from table 3.2 are assumed to be universal properties of the surface in this

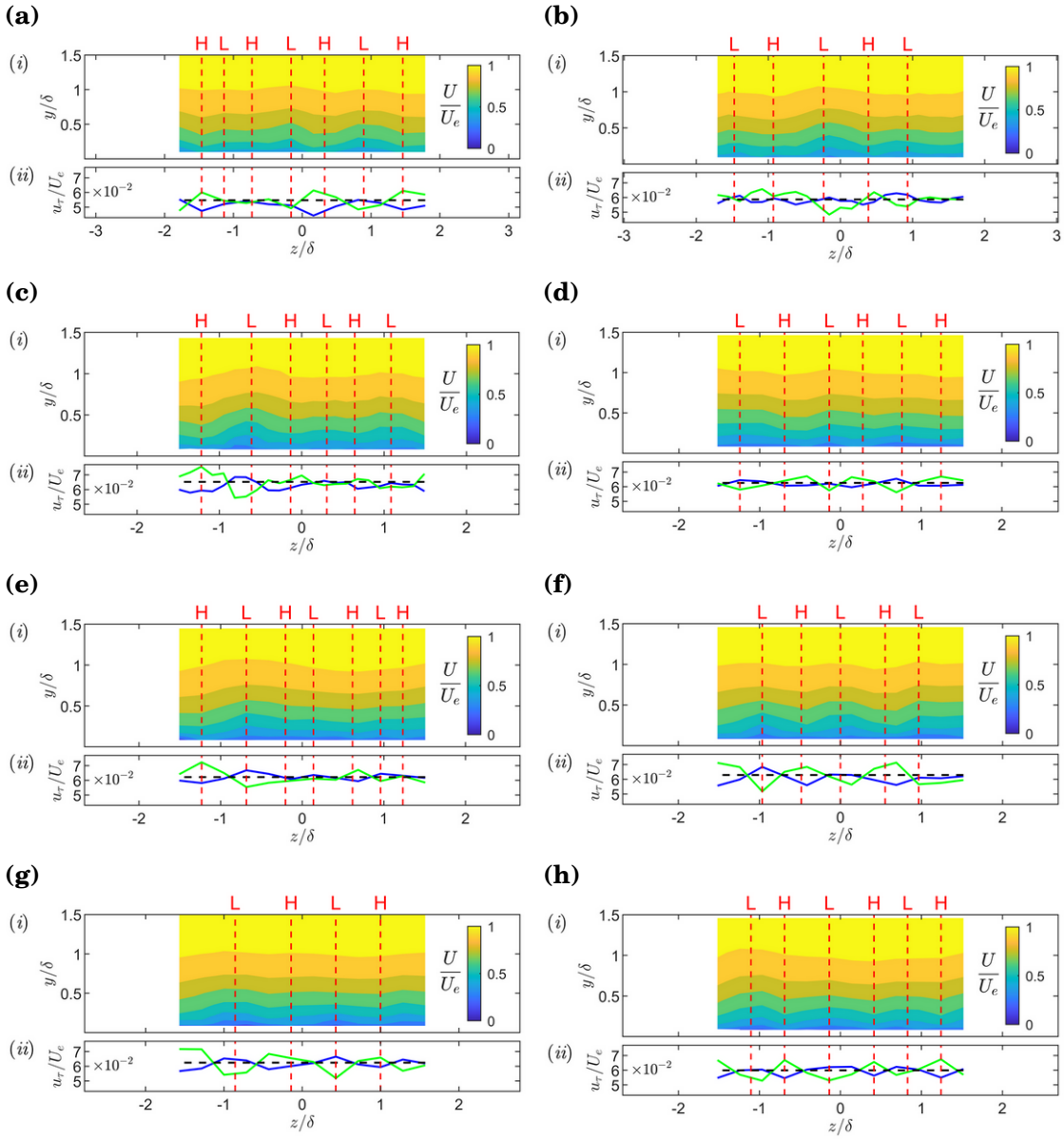

Figure 3.22: (a) R10, (b) R17, (c) R39, (d) R48, (e) R57, (f) R63, (g) R70, and (h) R78 local friction velocity correlations with HMPs and LMPs. Red dashed lines mark high and low momentum pathways with 'H' and 'L' respectively. Panes show outer-normalized (*i*) streamwise velocity, U/U_e, and (*ii*) local friction velocity, u_τ/U_e. The blue line is $u_{\tau,\mathrm{TSS}}/U_e$, and the green line is $u_{\tau,\mathrm{wall}}/U_e$. The black dashed line is u_τ from table 3.2.

alternative method. This is equivalent to assuming that equivalent sand-grain roughness, k_s, and wall offset, ϵ, are fixed. Holding y_0 and d fixed, the local friction velocity, $u_{\tau,\text{wall}}$, is then determined from a fit to the log-law equation between $0.10 < y/\delta < 0.19$. Figure 3.22 also shows the outer-normalized friction velocity results of this modified Clauser method. Now, it can be clearly seen that the $u_{\tau,\text{wall}}$ results conform with expectation from form drag. The subscript 'wall' indicates that the friction velocity was derived from the rough-wall form drag.

Local profile comparisons with other turbulent boundary layer profiles are now possible with local friction velocity scaling using either friction velocity $u_{\tau,\text{wall}}$ or $u_{\tau,\text{TSS}}$. It is readily seen in figure 3.23 that profiles scaled with $u_{\tau,\text{wall}}$ do not display outer-layer similarity. Also figures 3.23(b)-(d) all indicate a clear lack of collapse of the turbulent shear stresses under scaling with $u_{\tau,\text{wall}}$. In figure 3.23(a), the inner-normalized local profiles generally collapse in the log-law region with slight variation due to differences in local $u_{\tau,\text{wall}}$. In the wake region, the lack of collapse is not surprising. Each local profile had modified mean vertical velocity and varying local boundary layer thickness, and these differences manifest as different wake strengths since the profiles were forced to collapse in the log-law region.

Figure 3.23(f), in particular, highlights that the wake strength deviates considerably from the Castro[9] rough-wall data set especially in the HMPs where Π is lower. Profiles with high Π correspond with LMPs, and profiles

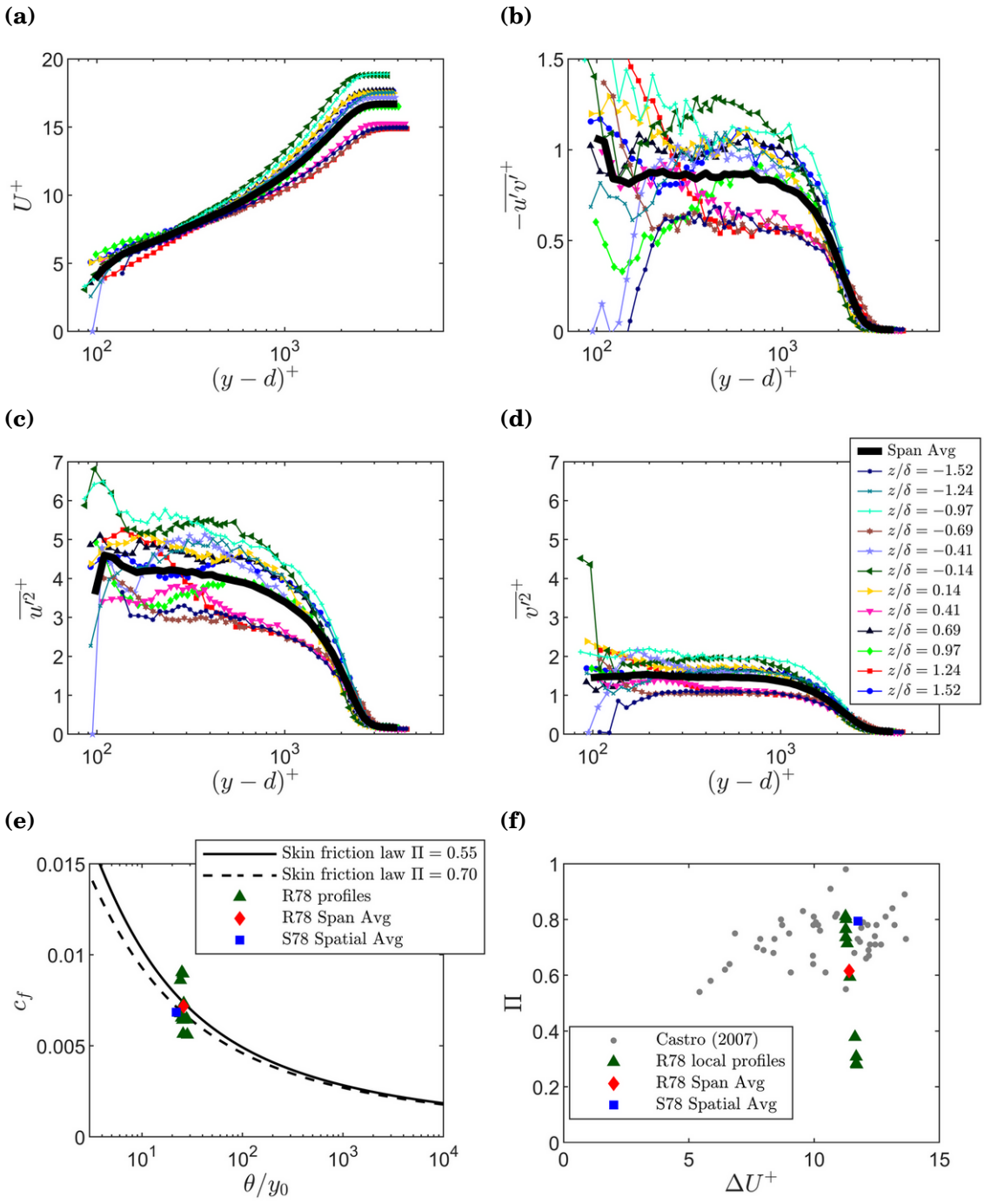

Figure 3.23: Inner-normalized (a) mean streamwise velocity, (b) Reynolds shear stress, (c) streamwise velocity variance, and (d) wall-normal velocity variance plotted for all local R78 profiles. Variation of Π as a function of (e) θ/y_0 and (f) roughness function, ΔU^+, plotted for all local R78 profiles. Local $u_{\tau,\text{wall}}$ was used for inner scaling and is representative of the local wall shear stress.

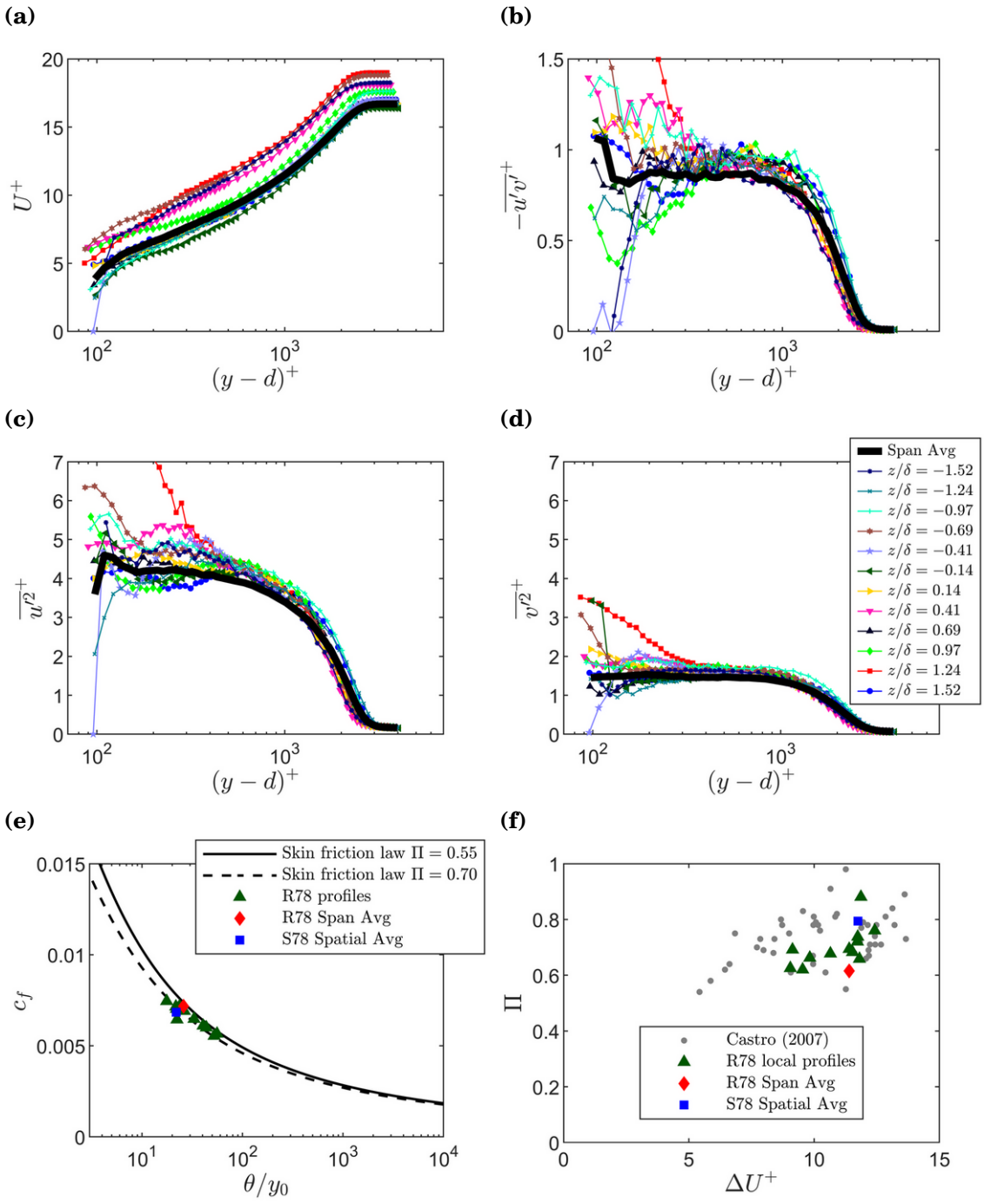

Figure 3.24: Inner-normalized (a) mean streamwise velocity, (b) Reynolds shear stress, (c) streamwise velocity variance, and (d) wall-normal velocity variance plotted for all local R78 profiles. Variation of Π as a function of (e) θ/y_0 and (f) roughness function, ΔU^+, plotted for all local R78 profiles. Local $u_{\tau,\mathrm{TSS}}$ was used for inner scaling and is representative of the local turbulent shear stress.

with low Π correspond with HMPs. This is contrary to Medjnoun et al.[45], who reported higher wake strength in the HMPs and lower wake strength in the LMPs. This difference can be explained by the difference in surface morphology. Medjnoun et al.[45] utilized infinitely long streamwise-aligned smooth rectangular strips with different spacing. In such a morphology, the LMPs exist over the rectangular strips and HMPs in the valleys between the strips. Medjnoun et al.[45] was able to directly measure friction velocity with oil-film interferometry and found that the highest friction velocity occurred over the strips. This means that the lowest wake strengths occurred over the highest measured friction velocity, which is consistent with the current finding.

Finally, local profile results are compared with the skin friction law[15;68;9;96]. A developing boundary layer over a homogeneous surface will tend to move from left to right on the curve. Figure 3.23(e) reveals that this development process has been locally altered across the span in the present data.

Figure 3.24 show the same series of plots with scaling by $u_{\tau,\mathrm{TSS}}$ which is representative of the local turbulent shear stress. The difference under this scaling is clear, and the plots for the Reynolds stresses appear to collapse better. Taken together the plots in figures 3.23 and 3.24 indicate that the turbulent boundary layer above has been decoupled from scaling with the actual local wall shear stress directly below by the lateral advection of turbulent stress. Instead, the turbulence stresses appear to scale more closely with the local turbulent

shear stress measured above the roughness canopy, while the mean velocity profile shows significant scatter.

This finding has significance for experiments where fluid dynamic total shear stress methods are used for indirectly determining the wall shear stress. All total shear stress methods rely on a 2D assumption which simplifies the streamwise momentum equation. The 2D assumption physically means that all turbulent shear stresses are expected to originate from the surface directly below and are representative of the local wall shear stress. However, when secondary flows are present, this may not be the case. A single profile normalized with $u_{\tau,\mathrm{TSS}}$ would look like any single profile from figure 3.24 with little evidence of significant deviation from universality. This may lead to erroneous findings for the test. Laterally-averaged profiles must be used to obtain good results for flows in which secondary flow structures are present.

3.4.5 Momentum pathway Reynolds shear stress quadrant analysis

The LDV measurements from these tests provide a unique opportunity to explore the differences in the turbulence structure within the HMPs and LMPs. A useful technique for investigating changes in turbulence structure is quadrant analysis, first introduced by Wallace et al.[90]. Quadrant analysis

consists of conditional averaging of Reynolds shear stress contributions in each of the four quadrants on a plot of v' versus u' velocity fluctuations: Q1 outward interactions ($+u'$,$+v'$), Q2 ejections ($-u'$,$+v'$), Q3 inward interactions ($-u'$,$-v'$), and Q4 sweeps ($+u'$,$-v'$). Q2 ejections and Q4 sweeps events are the largest contributors to Reynolds shear stress and deserve special attention. They represent the transport of low momentum fluid away from the wall and high momentum fluid toward the wall which has been a major topic of this study. Willmarth and Lu [94] expanded the capability of quadrant analysis with the addition of the hyperbolic hole size, H, which further allows conditional sampling of the most significant quadrant events. Here, the quadrant analysis utilizes the hyperbolic hole technique employed by Lu and Willmarth [43] among others.

Reynolds shear stress quadrant analysis was performed on the LDV data from these experiments. Each quadrant contribution is computed as

$$\overline{u'v'}_{\mathrm{Q}} = \frac{1}{N_c} \sum_{i=1}^{N_Q} (u'v')_{\mathrm{Q,i}} \, I_{\mathrm{Q,i}}, \tag{3.4}$$

where $I_{\mathrm{Q}}(t)$ is an indicator function defined as

$$I_{\mathrm{Q}} = \begin{cases} 1 & \text{when } |u'v'|_{\mathrm{Q}} \geq H(\overline{u'^2})^{1/2}(\overline{v'^2})^{1/2} \\ 0 & \text{otherwise,} \end{cases} \tag{3.5}$$

N_c is the number of coincident LDV u and v velocity realizations, and N_Q is the number of coincident realizations in the quadrant. The saturable-detector scheme yields nearly even-time velocity samples for LDV statistics in this study and makes the summation of equation 3.4 nearly equivalent to the time integral utilized by other studies.

Figure 3.25 presents Q2 and Q4 quadrant data from the least dense and most dense random test plates computed with hole sizes of $H = 0$ and $H = 1$. The following qualitative analysis focuses on entire cross-stream contours rather than specific vertical LMP or HMP profiles. Because there is a lack of imposed periodicity or symmetries (as would be the case for regular roughness element arrangements), choosing specific LMP or HMP profiles for direct comparison would involve arbitrary selection. Instead, the contour plots allow several overall trends to be discerned more clearly.

In the top row of figures 3.25(a)-(d), reduced and enhanced Reynolds shear stress in the HMPs and LMPs, respectively, is clearly identifiable. In the lower four rows, figures 3.25(e)-(t), quadrant contributions and ratios are shown for the lower half of the boundary layer where Reynolds shear stress is more significant, and the vertical aspect has been stretched to fill the plot when compared to the top row figures 3.25(a)-(d). In the second row figures 3.25(e)-(h), a clear trend is observed with higher relative percent contribution of Q2 events in the HMPs and lower relative contribution in the LMPs. In contrast, percent contribution

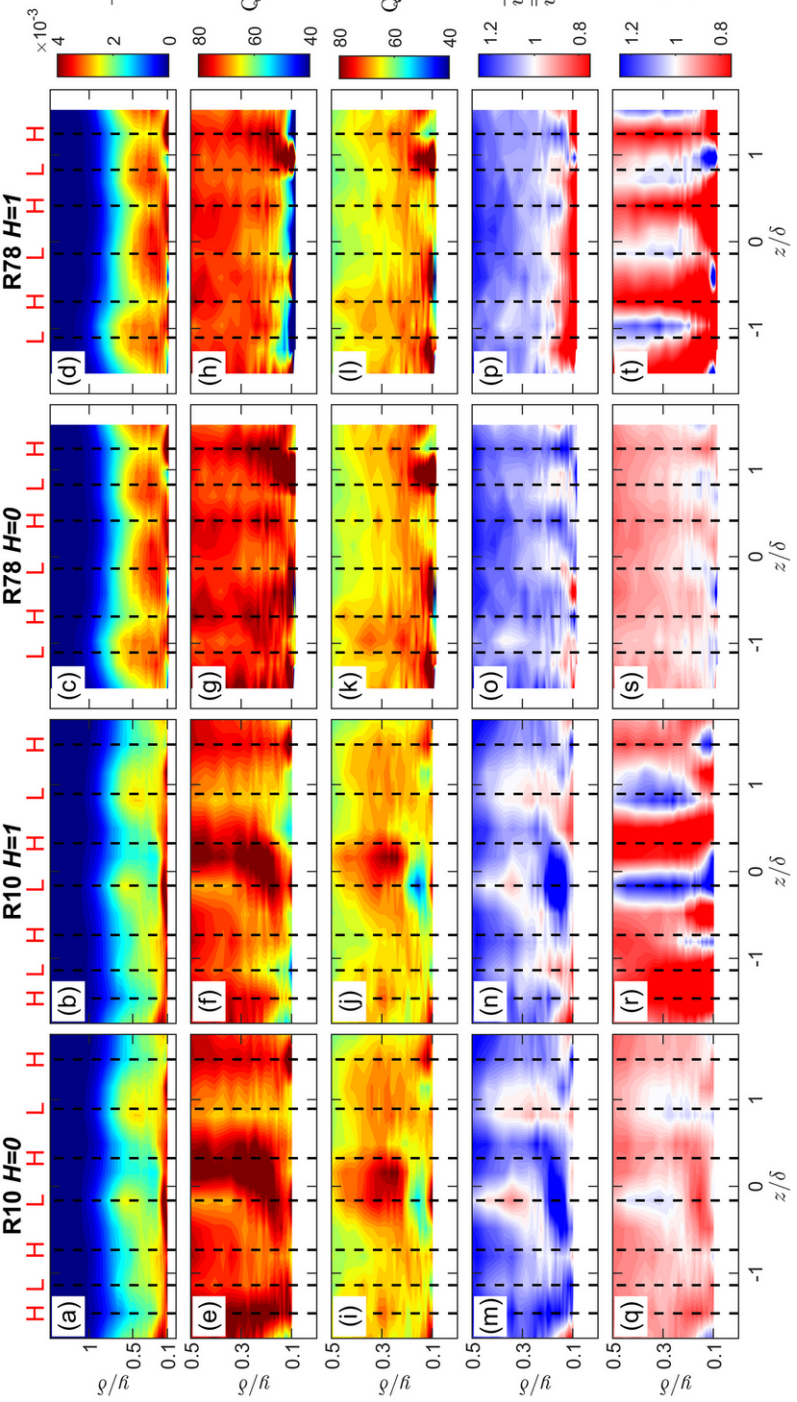

Figure 3.25: Contour plots of Reynolds shear stress quadrant data from LDV measurements. Rows are outer-normalized (a,b,c,d) Reynolds shear stress ($-\overline{u'v'}/U_e^2$), (e,f,g,h) Reynolds shear stress Q2 percentage contribution ($\mathrm{Q2}\,(\%) = 100\,\overline{\mathrm{u'v'}}_{\mathrm{Q2}}/\overline{\mathrm{u'v'}}$), (i,j,k,l) Reynolds shear stress Q4 percentage contribution ($\mathrm{Q4}\,(\%) = 100\,\overline{\mathrm{u'v'}}_{\mathrm{Q4}}/\overline{\mathrm{u'v'}}$), (m,n,o,p) Reynolds shear stress Q2 over Q4 ratio ($\overline{u'v'}_{\mathrm{Q2}}/\overline{u'v'}_{\mathrm{Q4}}$), (m,n,o,p) ratio of Q2 events over Q4 events ($N_{\mathrm{Q2}}/N_{\mathrm{Q4}}$). Columns are data from (a,e,i,m,q) R10 with $H = 0$, (b,f,j,n,r) R10 with $H = 1$, (c,g,k,o,s) R78 with $H = 0$, and (d,h,l,p,t) R78 with $H = 1$. Vertical dashed black lines indicate approximate position of HMPs or LMPs with letter 'H' or 'L', respectively. In the lower four rows (e-p), the vertical aspect has been stretched to focus on the lower half of the boundary layer.

of Q4 events shows no clear trend with respect to HMPs and LMPs in the third row figures 3.25(i)-(l).

The contributions from Q2 events are compared to the contribution from Q4 events by taking their ratio ($\overline{u'v'}_{\mathrm{Q2}}/\overline{u'v'}_{\mathrm{Q4}}$). The fourth row of contour plots in figures 3.25(m)-(p) presents contour plots of this ratio. In HMPs, Q2 contributions are up to 20% larger than Q4 as seen in blue from $0.1 \lesssim y/\delta \lesssim 0.5$. This is consistent with other studies over honed-pipe, sand-grain, and wire mesh surfaces for boundary layers where secondary flows were not evident[39;74;52]. In LMPs, the white (to light red) stands in contrast to the blue and indicates approximate parity in the Q2 and Q4 contributions. This appears to be a clear modification of the turbulence structure in the LMPs with respect to other rough-wall boundary layers.

A final comparison can be made between the number of Q2 and Q4 events occurring in HMPs and LMPs. The number of events is a proxy for time fractions because the virtual saturable-detector scheme provides nearly even-time sampling. Figures 3.25(q) and (s) show ratios of the total number of Q2 events over the total number of Q4 events ($N_{\mathrm{Q2}}/N_{\mathrm{Q4}}$) for R10 and R78 respectively. The plots appear light red to white signifying a ratio of just below one to one. This is consistent with Morrill-Winter et al.[52] who appears to be one of the only rough-wall data sets that presents time fractions. Perhaps the most striking difference observed in figure 3.25 is presented in the ratio of

strong Q2 ejection events to strong Q4 sweep events. It is clear from figures 3.25(r) and (t) that the number of strong sweeps is dominant in the HMPs and the number of strong ejections is dominant in the LMPs. This stands in contrast to measurements from Morrill-Winter et al.[52] which show a time ratio of approximately 1.1 for strong ($H = 1$) ejections over sweeps in this region which would appear light blue in figures 3.25(r) and (t). This indicates that the turbulence structure has changed in the HMPs with strong sweep events occurring more frequently than on other rough-walls. However, the current observations appear congruent with the present momentum pathways because they indicate that time spent strongly ejecting low momentum fluid upward in the boundary layer dominates in LMPs while time spent strongly sweeping high momentum fluid downward in the boundary layer dominates in HMPs.

3.5 Conclusions

Turbulent boundary layer measurements over regular and irregular truncated cone roughness, covering a wide range of planform densities, were presented and compared with other rough-wall data from the literature. Eight planform densities ranging from 10% to 78% were tested in both square staggered and random distributions to determine trends as a function of density and contrast the behaviors of irregular versus regular roughness distributions.

Important turbulent boundary layer parameters such as friction velocity, thickness, roughness length, and zero-plane displacement, showed only minor differences between the regular and random arrangements when determined using well-resolved spatial-averaged profiles, i.e. averaged over the span or a representative tile of horizontal heterogeneity. Roughness length y_0, in particular, showed close agreement between regular and random surface cases at the same density, suggesting that fluid dynamic drag is more a function of the roughness density and element shape than its particular arrangement. Peak roughness length occurred at approximately 40% planform density. The Macdonald et al.[44] morphometric drag model predicted roughness length well at densities below the peak, and the Zhu et al.[101] model predicted roughness length well above the peak. However, both models required adjusting model coefficients within reported ranges, suggesting more data are needed for accurate drag prediction and more refined models which should be valid over the entire λ_p range.

Multiple profiles were recorded over all regular and irregular arrangements. Local profiles over staggered arrangements differed only within the roughness sublayer which extended less than $2k$ above the roughness crests. In contrast, local profiles over random arrangements showed differences throughout the entire boundary layer, indicating a breakdown in outer-layer similarity that was not observed over the regular roughness. Wall-normal spanwise LDV and stereo PIV measurement planes showed that secondary flows were responsible for

this breakdown and were associated with high and low momentum pathways. The HMPs and LMPs were consistent with other studies' observations of these flow structures in measurements of streamwise velocity, signed swirl strength, Reynolds shear stress, and turbulent kinetic energy.

The HMPs and LMPs did not appear to be correlated with local surface topography but may be correlated with topography at the random roughness leading edge. It was suggested that spanwise flow heterogeneity, inducing skin-friction heterogeneity, may be self-prolonging over the random truncated cone surfaces and not require further spanwise roughness heterogeneity for sustainment downstream of the initiation. Two methods were used to calculate local friction velocity across the span on the random cases. Results confirmed skin-friction heterogeneity but provided opposing, anti-correlated results. Differences in the methods' results and their ability to universally scale the turbulent boundary layer profiles were explored, and results were consistent with the view that the secondary flows disassociate local scaling of the turbulent boundary layer profile with local wall shear stress due to the lateral advection of turbulent stresses.

Reynolds shear stress quadrant analysis revealed that the turbulence structure in the HMPs was modified, specifically the time fraction of strong sweeps was much greater than strong ejections in the lower half of the boundary layer. Such behavior was not observed in LMPs or in earlier data from the literature on flows over sand-grain roughness. Additionally, LMPs showed approximate

parity of Reynolds shear stress contributions from ejection and sweep events in the lower half of the boundary layer. Conversely, a variety of other rough surfaces in the literature have shown ejections typically contribute 10% to 20% more.

An important conclusion from this study of regular and irregular truncated cones is that full-scale drag prediction may be less arduous than expected. Regular and irregular arrangements of truncated cones show little difference in fluid dynamic drag measurements which suggests that there may be less need to explore both regular and irregular arrangements of a particular roughness morphology for drag prediction data (excepting roughness clustering not considered here). Additionally, the secondary flows had little effect on the overall surface drag which indicates that the observed breakdown in outer-layer similarity may not affect drag significantly. These are welcome findings for the advancement of drag prediction.

However, despite these findings for drag prediction, many open questions remain concerning secondary flows over rough surfaces. First, it is important to understand the specific conditions and fluid dynamic mechanisms generating secondary flows. If spanwise irregularity at the leading edge of roughness can cause sustained secondary flows, there are implications in other contexts. Second, it is important to better understand secondary flow sustainment over irregular roughness. Turbulence measurements within the roughness canopy

could provide further evidence for the sustainment mechanism posited in this study. Lastly, it remains to be seen how these secondary flows develop without identified surface features to influence their behavior. Measurements from multiple streamwise fetch locations are needed to explore such effects. Without definite answers to these questions, this study shows that investigators must ensure representative profiles are utilized for evaluating drag and other flow properties by either verifying the absence of secondary flows or by sufficient spatial-averaging.

Chapter 4

Conclusions

This work has presented an experimental data set for turbulent boundary layer flow over truncated cone roughness. The turbulent boundary layer data were analyzed with a novel comprehensive shear stress analysis technique which provides better friction velocity accuracy than other available methods[96]. Two current drag prediction models were tested against the truncated cone roughness morphology with some success. However, the data can continue to be used used to test, refine, and develop future drag prediction models through the roughness database[13] (`http://roughnessdatabase.org/`). For example, roughness drag results presented here have already been used to inform United States Navy ship hull cleaning procedures[32]. The data were also used to improve understanding of the differences in flow over random and regular roughness arrangements and to identify high and low momentum

pathways with characteristics that were contrary to expectation given currently available literature.

Further studies in truncated cone roughness flow prediction should focus on clustering of roughness elements and studying flow with a smaller ratio of roughness height to the boundary layer thickness. Finally, observation of high and low momentum pathways over this irregular roughness topography and differences with expected trends should motivate further inquiries into the generation, sustainment, and evolution of secondary flows in turbulent boundary layers. Flow statistics at multiple streamwise development locations and within the roughness canopy over irregular surfaces with secondary flows would help inform these open topics.

Appendix A

Adaption of the Macdonald et al.[44] model to truncated cones

The final roughness length, y_0, expression in Macdonald et al.[44] in notation from this study is

$$\frac{y_0}{k} = \left(1 - \frac{d}{k}\right) \exp\left[-\left(\frac{\beta}{2}\frac{C_{DH}}{\kappa^2}\left(1 - \frac{d}{k}\right)\lambda_f\right)^{-\frac{1}{2}}\right]. \tag{A.1}$$

k is the height of the roughness, d is the zero-plane displacement, and β is a correction factor. C_{DH} is the coefficient of drag with respect to the mean velocity at the roughness crest, U_H, and λ_f is the frontal density. This study assumes no empirical correction factor, so $\beta = 1$.

In (A.1), the quantity $(1 - d/k)\lambda_f$ is a substitution for the frontal density

above d, $\lambda_f^* = A_f^*/A_0$, where A_f^* is the frontal area above d and A_0 is the lot area. It assumes a constant roughness cross-sectional area with respect to height which is not appropriate for truncated cones, so the more general expression A_f^*/A_0 is substituted

$$\frac{y_0}{k} = \left(1 - \frac{d}{k}\right) \exp\left[-\left(\frac{\beta}{2}\frac{C_{DH}}{\kappa^2}\frac{A_f^*}{A_0}\right)^{-\frac{1}{2}}\right]. \tag{A.2}$$

In order to solve the equation for truncated cones, morphometric expressions are required for d and A_f^*. While acknowledging its limitations, Macdonald et al.[44] suggests that a minimum estimate for d can be obtained by solving the height formed by distributing the aggregate volume of obstacles over the lot area. The staggered truncated cone repeating unit, in figures 3.1(a)-(h), contained two truncated cones on the lot area. Also, for a truncated cone with base diameter, D, and diameter at height k, D_k, an equation for varying diameter with height is $D_h(h) = D - h/k\,(D - D_k)$. Thus, an expression for d with two truncated cones on lot area, A_0, is

$$\begin{aligned} d = \frac{2V}{A_0} = \frac{2}{A_0}\int_0^k \frac{\pi}{4}\left[D - \frac{h}{k}(D - D_k)\right]^2 \mathrm{d}h \\ = \frac{\pi k}{2A_0}\left[D^2 + D(D_k - D) + \frac{1}{3}(D_k - D)^2\right], \end{aligned} \tag{A.3}$$

and an expression for the frontal area of two truncated cones above d, is

$$A_f^* = 2\frac{1}{2}\left(k-d\right)\left(D_k + D_h\left(d\right)\right) = \left(k-d\right)\left(D_k + D - \frac{d}{k}\left(D - D_k\right)\right). \tag{A.4}$$

For the plot in figure 3.9, (A.2) and $\lambda_p = \pi D^2/(2A_0)$ are solved explicitly by adjusting A_0 in the desired range with the substitutions for (A.3) and (A.4). It should be noted that this derivation assumes no overlapping of truncated cones. In a square staggered arrangement, this means that minimum $A_0 = 2D^2$.

Bibliography

[1] R. J. Adrian, K. T. Christensen, and Z.-C. Liu. Analysis and interpretation of instantaneous turbulent velocity fields. *Experiments in Fluids*, 29(3): 275–290, Sep 2000. ISSN 1432-1114. doi: 10.1007/s003489900087.

[2] M. Amir and I. P. Castro. Turbulence in rough-wall boundary layers: Universality issues. *Experiments in Fluids*, 51(2):313–326, Aug 2011. ISSN 1432-1114. doi: 10.1007/s00348-011-1049-7.

[3] W. Anderson, J. M. Barros, K. T. Christensen, and A. Awasthi. Numerical and experimental study of mechanisms responsible for turbulent secondary flows in boundary layer flows over spanwise heterogeneous roughness. *Journal of Fluid Mechanics*, 768:316–347, 2015. ISSN 0022-1120. doi: 10.1017/jfm.2015.91.

[4] W. J. Baars, D. T. Squire, K. M. Talluru, M. R. Abbassi, N. Hutchins, and I. Marusic. Wall-drag measurements of smooth- and rough-wall turbulent

boundary layers using a floating element. *Experiments in Fluids*, 57(5): 90, May 2016. ISSN 1432-1114. doi: 10.1007/s00348-016-2168-y.

[5] J. M. Barros and K. T. Christensen. Observations of turbulent secondary flows in a rough-wall boundary layer. *Journal of Fluid Mechanics*, 748: R1, 2014. doi: 10.1017/jfm.2014.218.

[6] A. K. Betts, J. H. Ball, A. C. M. Beljaars, M. J. Miller, and P. A. Viterbo. The land surface-atmosphere interaction: A review based on observational and global modeling perspectives. *Journal of Geophysical Research: Atmospheres*, 101(D3):7209–7225, 1996. doi: doi.org/10.1029/95JD02135.

[7] J. P. Bons. St and c_f augmentation for real turbine roughness with elevated freestream turbulence. *Journal of Turbomachinery*, 124(4):632–644, Nov 2002. ISSN 0889-504X. doi: 10.1115/1.1505851.

[8] B. Brzek, R. B. Cal, G. Johansson, and L. Castillo. Inner and outer scalings in rough surface zero pressure gradient turbulent boundary layers. *Physics of Fluids*, 19(6):065101, 2007. doi: 10.1063/1.2732439.

[9] I. P. Castro. Rough-wall boundary layers: Mean flow universality. *Journal of Fluid Mechanics*, 585:469–485, 2007. doi: 10.1017/S0022112007006921.

[10] K. A. Chauhan, P. A. Monkewitz, and H. M. Nagib. Criteria for assessing

experiments in zero pressure gradient boundary layers. *Fluid Dynamics Research*, 41(2):021404, Mar 2009. doi: 10.1088/0169-5983/41/2/021404.

[11] H. Cheng, P. Hayden, A. G. Robins, and I. P. Castro. Flow over cube arrays of different packing densities. *Journal of Wind Engineering and Industrial Aerodynamics*, 95(8):715–740, 2007. ISSN 0167-6105. doi: doi.org/10.1016/j.jweia.2007.01.004.

[12] H. Cheng and I. P. Castro. Near wall flow over urban-like roughness. *Boundary-Layer Meteorology*, 104:229–259, 2002. ISSN 00068314. doi: 10.1023/A:1016060103448.

[13] D. Chung, N. Hutchins, M. P. Schultz, and K. A. Flack. Predicting the drag of rough surfaces. *Annual Review of Fluid Mechanics*, 53(1):439–471, 2021. doi: 10.1146/annurev-fluid-062520-115127.

[14] J. Claus, P.-A. Krogstad, and I. P. Castro. Some measurements of surface drag in urban-type boundary layers at various wind angles. *Boundary-Layer Meteorology*, 145(3):407–422, Dec 2012. ISSN 1573-1472. doi: 10.1007/s10546-012-9736-3.

[15] F. H. Clauser. Turbulent boundary layers in adverse pressure gradients. *Journal of the Aeronautical Sciences*, 21(2):91–108, 1954. doi: 10.2514/8.2938.

[16] F. H. Clauser. The turbulent boundary layer. In H. Dryden and T. von Kármán, editors, *Advances in Applied Mechanics*, volume 4, pages 1 – 51. Elsevier, 1956. doi: https://doi.org/10.1016/S0065-2156(08)70370-3.

[17] C. F. Colebrook and C. M. White. Experiments with fluid friction in roughened pipes. *Proceedings of the Royal Society of London A: Mathematical, Physical and Engineering Sciences*, 161(906):367–381, 1937. ISSN 0080-4630. doi: 10.1098/rspa.1937.0150.

[18] D. Coles. The law of the wake in the turbulent boundary layer. *Journal of Fluid Mechanics*, 1(2):191–226, 1956. ISSN 0022-1120. doi: 10.1017/S0022112056000135.

[19] M. A. Ferreira, E. Rodriguez-Lopez, and B. Ganapathisubramani. An alternative floating element design for skin-friction measurement of turbulent wall flows. *Experiments in Fluids*, 59(10):155, Sep 2018. ISSN 1432-1114. doi: 10.1007/s00348-018-2612-2.

[20] K. A. Flack and M. P. Schultz. Roughness effects on wall-bounded turbulent flows. *Physics of Fluids*, 26:101305, 2014. ISSN 1070-6631. doi: 10.1063/1.4896280.

[21] K. A. Flack, M. P. Schultz, and T. A. Shapiro. Experimental support for Townsend's Reynolds number similarity hypothesis on rough walls. *Physics of Fluids*, 17(3):035102, 2005. doi: 10.1063/1.1843135.

BIBLIOGRAPHY

[22] K. A. Flack, M. P. Schultz, and J. S. Connelly. Examination of a critical roughness height for outer layer similarity. *Physics of Fluids*, 19:095104, 2007. doi: 10.1063/1.2757708.

[23] P. Forooghi, A. Stroh, P. Schlatter, and B. Frohnapfel. Direct numerical simulation of flow over dissimilar, randomly distributed roughness elements: A systematic study on the effect of surface morphology on turbulence. *Physical Review Fluids*, 3:044605, Apr 2018. doi: 10.1103/PhysRevFluids.3.044605.

[24] K. Fukagata, K. Iwamoto, and N. Kasagi. Contribution of Reynolds stress distribution to the skin friction in wall-bounded flows. *Physics of Fluids*, 14(11):L73–L76, 2002. doi: 10.1063/1.1516779.

[25] C. S. B. Grimmond and T. R. Oke. Aerodynamic properties of urban areas derived from analysis of surface form. *Journal of Applied Meteorology*, 38(9):1262 – 1292, Sep 1999. doi: 10.1175/1520-0450(1999)038⟨1262:APOUAD⟩2.0.CO;2.

[26] A. Hagishima, J. Tanimoto, K. Nagayama, and S. Meno. Aerodynamic parameters of regular arrays of rectangular blocks with various geometries. *Boundary-Layer Meteorology*, 132(2):315–337, Aug 2009. ISSN 1573-1472. doi: 10.1007/s10546-009-9403-5.

[27] D. J. Hall, R. Macdonald, and S. Walker. Measurements of dispersion

within simulated urban arrays: A small scale wind tunnel study. Technical report, Building Research Establishment Client Rep. 178/96, Garston, Watford, UK, 1996.

[28] J. H. Haritonidis. The measurement of wall shear stress. In *Advances in Fluid Mechanics Measurements*, pages 229–261. Springer, 1989. ISBN 0387511369.

[29] J. O. Hinze. Secondary currents in wall turbulence. *The Physics of Fluids*, 10(9):S122–S125, 1967. doi: 10.1063/1.1762429.

[30] J. O. Hinze. Experimental investigation on secondary currents in the turbulent flow through a straight conduit. *Applied Scientific Research*, 28 (1):453–465, 1973. doi: 10.1007/BF00413083.

[31] L. C. Hoagland. *Fully Developed Turbulent Flow in Straight Rectangular Ducts: Secondary Flow, Its Cause and Effect on the Primary Flow*. PhD thesis, Massachusetts Institute of Technology, 1962.

[32] E. R. Holm, M. P. Schultz, K. Lieberman, W. D. Gottwald IV, E. G. Haslbeck, and T. P. McCue. A revised scale for rating biofouling of US Navy vessels. Technical Memorandum NSWCCD-61-TR-2019/1, Naval Surface Warfare Center Carderock Division, May 2019.

[33] P. S. Jackson. On the displacement height in the logarithmic velocity

profile. *Journal of Fluid Mechanics*, 111:15–25, 1981. doi: 10.1017/S0022112081002279.

[34] J. Jiménez. Turbulent flows over rough walls. *Annual Review of Fluid Mechanics*, 36(1):173–196, 2004. doi: 10.1146/annurev.fluid.36.050802.122103.

[35] L. Keirsbulck, L. Labraga, A. Mazouz, and C. Tournier. Surface roughness effects on turbulent boundary layer structures. *Journal of Fluids Engineering*, 124:127–135, 2002. ISSN 00982202. doi: 10.1115/1.1445141.

[36] I. G. Kempf. On the effect of roughness on the resistance of ships. In *Spring Meetings of the Seventy-eighth Session of the Institution of Naval Architects*, pages 109–119, 1937.

[37] J. C. Klewicki, W. S. Saric, I. Marusic, and J. K. Eaton. *Springer Handbook of Experimental Fluid Mechanics*, chapter Wall-bounded Flows, pages 871–907. Springer, Berlin, 2007. doi: 10.1007/978-3-540-30299-5.

[38] P. A. Krogstad and R. A. Antonia. Surface roughness effects in turbulent boundary layers. *Experiments in fluids*, 27:450–460, 1999. ISSN 0723-4864. doi: 10.1007/s003480050370.

[39] P. A. Krogstad, R. A. Antonia, and L. W. B. Browne. Comparison between

rough- and smooth-wall turbulent boundary layers. *Journal of Fluid Mechanics*, 245:599–617, 1992. doi: 10.1017/S0022112092000594.

[40] P.-A. Krogstad and V. Efros. Rough wall skin friction measurements using a high resolution surface balance. *International Journal of Heat and Fluid Flow*, 31(3):429–433, 2010. ISSN 0142-727X. doi: doi.org/10.1016/j.ijheatfluidflow.2009.11.007. Sixth International Symposium on Turbulence and Shear Flow Phenomena.

[41] S. Leonardi and I. P. Castro. Channel flow over large cube roughness: A direct numerical simulation study. *Journal of Fluid Mechanics*, 651: 519–539, 2010. ISSN 00221120. doi: 10.1017/S002211200999423X.

[42] J. D. Li, S. M. Henbest, and A. E. Perry. The difficulties in the measurements of Reynolds stresses in smooth- and in rough-wall turbulent boundary layers. In *9th Australasian Fluid Mechanics Conference*, pages 456–459, Auckland, New Zealand, Dec 1986.

[43] S. S. Lu and W. W. Willmarth. Measurements of the structure of the Reynolds stress in a turbulent boundary layer. *Journal of Fluid Mechanics*, 60(3):481–511, 1973. doi: 10.1017/S0022112073000315.

[44] R. W. Macdonald, R. F. Griffiths, and D. J. Hall. An improved method for the estimation of surface roughness of obstacle arrays. *Atmospheric*

Environment, 32:1857–1864, 1998. ISSN 13522310. doi: 10.1016/S1352-2310(97)00403-2.

[45] T. Medjnoun, C. Vanderwel, and B. Ganapathisubramani. Characteristics of turbulent boundary layers over smooth surfaces with spanwise heterogeneities. *Journal of Fluid Mechanics*, 838:516–543, 2018. doi: 10.1017/jfm.2017.849.

[46] T. Medjnoun, C. Vanderwel, and B. Ganapathisubramani. Effects of heterogeneous surface geometry on secondary flows in turbulent boundary layers. *Journal of Fluid Mechanics*, 886:A31, 2020. doi: 10.1017/jfm.2019.1014.

[47] F. Mehdi and C. M. White. Integral form of the skin friction coefficient suitable for experimental data. *Experiments in Fluids*, 50(1):43–51, Jan 2011. ISSN 1432-1114. doi: 10.1007/s00348-010-0893-1.

[48] F. Mehdi, T. G. Johansson, C. M. White, and J. W. Naughton. On determining wall shear stress in spatially developing two-dimensional wall-bounded flows. *Experiments in Fluids*, 55(1):1656, 2014. ISSN 1432-1114. doi: 10.1007/s00348-013-1656-6.

[49] R. Mejia-Alvarez and K. T. Christensen. Low-order representations of irregular surface roughness and their impact on a turbulent boundary layer. *Physics of Fluids*, 22(1):015106, 2010. doi: 10.1063/1.3291076.

[50] R. Mejia-Alvarez and K. T. Christensen. Wall-parallel stereo particle-image velocimetry measurements in the roughness sublayer of turbulent flow overlying highly irregular roughness. *Physics of Fluids*, 25(11): 115109, 2013. doi: 10.1063/1.4832377.

[51] C. Morrill-Winter, J. Klewicki, R. Baidya, and I. Marusic. Temporally optimized spanwise vorticity sensor measurements in turbulent boundary layers. *Experiments in Fluids*, 56(12):216, Nov 2015. ISSN 1432-1114. doi: 10.1007/s00348-015-2084-6.

[52] C. Morrill-Winter, D. T. Squire, J. C. Klewicki, N. Hutchins, M. P. Schultz, and I. Marusic. Reynolds number and roughness effects on turbulent stresses in sandpaper roughness boundary layers. *Physical Review Fluids*, 2:054608, May 2017. doi: 10.1103/PhysRevFluids.2.054608.

[53] S. Nakagawa and T. J. Hanratty. Particle image velocimetry measurements of flow over a wavy wall. *Physics of Fluids*, 13(11):3504–3507, 2001. doi: 10.1063/1.1399291.

[54] Naval Ships' Technical Manual. *Waterbourne Underwater Hull Cleaning of Navy Ships*, chapter 081. S9086-CQ-STM-010. Naval Sea Systems Command, Oct 2006.

[55] J. Nikuradse. *Untersuehungen über die Gesdiwindigkeitsverteilung*

in Turbulenten Strömungen. PhD thesis, University of Göttingen, VDI—Forschungsheft 281, Berlin, 1926.

[56] J. Nikuradse. Untersuchungen über turbulente strömungen in nicht kreisförmigen rohren. *Ingenieur-archiv*, 1(3):306–332, 1930.

[57] J. Nikuradse. Laws of flow in rough pipes. Technical Memorandum 1292, National Advisory Committee for Aeronautics, Washington, Jul/Aug 1933.

[58] G. Pathikonda and K. T. Christensen. Inner-outer interactions in a turbulent boundary layer overlying complex roughness. *Physical Review Fluids*, 2:1–21, 2017. ISSN 2469990X. doi: 10.1103/PhysRevFluids.2.044603.

[59] A. E. Perry and P. N. Joubert. Rough-wall boundary layers in adverse pressure gradients. *Journal of Fluid Mechanics*, 17(2):193–211, 1963. doi: 10.1017/S0022112063001245.

[60] A. E. Perry and J. D. Li. Experimental support for the attached-eddy hypothesis in zero-pressure-gradient turbulent boundary layers. *Journal of Fluid Mechanics*, 218:405–438, 1990. ISSN 14697645. doi: 10.1017/S0022112090001057.

[61] M. Placidi and B. Ganapathisubramani. Effects of frontal and plan solidities on aerodynamic parameters and the roughness sublayer in turbulent

boundary layers. *Journal of Fluid Mechanics*, 782:541–566, 2015. ISSN 0022-1120. doi: 10.1017/jfm.2015.552.

[62] M. Placidi and B. Ganapathisubramani. Turbulent flow over large roughness elements: Effect of frontal and plan solidity on turbulence statistics and structure. *Boundary-Layer Meteorology*, 167(1):99–121, Apr 2018. ISSN 1573-1472. doi: 10.1007/s10546-017-0317-3.

[63] M. Placidi and B. Ganapathisubramani. Velocity statistics for rough-wall turbulent boundary layer flow over lego roughness elements in different layouts. University of Southampton, Mar 2019. doi: dx.doi.org/10.5258/SOTON/D0829.

[64] L. Prandtl. Turbulent flow. Technical Memorandum 435, National Advisory Committee for Aeronautics, Washington, Oct 1927.

[65] M. R. Raupach, R. A. Antonia, and S. Rajagopalan. Rough-wall turbulent boundary layers. *Applied Mechanics Reviews*, 44:1–25, 1991. ISSN 0003-6900. doi: 10.1115/1.3119492.

[66] R. T. Reynolds, P. Hayden, I. P. Castro, and A. G. Robins. Spanwise variations in nominally two-dimensional rough-wall boundary layers. *Experiments in Fluids*, 42(2):311–320, Feb 2007. ISSN 1432-1114. doi: 10.1007/s00348-006-0243-5.

[67] R. T. Reynolds and I. P. Castro. Measurements in an urban-type boundary layer. *Experiments in Fluids*, 45:141–156, 2008. ISSN 07234864. doi: 10.1007/s00348-008-0470-z.

[68] J. Rotta. Turbulent boundary layers in incompressible flow. *Progress in Aerospace Sciences*, 2(1):1–95, 1962. ISSN 0376-0421. doi: doi.org/10.1016/0376-0421(62)90014-3.

[69] J. Sadique. *Turbulent Flows over Macro-Scale Roughness Elements - From Biofouling Barnacles to Urban Canopies*. PhD thesis, The Johns Hopkins University, Jun 2016.

[70] B. Sadler. *2021 Index of U.S. Military Strength*, chapter U.S. Navy, pages 381–410. The Heritage Foundation, Washington, DC, 2020.

[71] H. Schlichting. Experimental investigation of the problem of surface roughness. Technical Memorandum 823, National Advisory Committee for Aeronautics, Washington, Apr 1937.

[72] H. Schlichting. *Boundary Layer Theory*. McGraw-Hill, New York, 7th edition, 1979. ISBN 0-07-055334-3.

[73] M. P. Schultz and K. A. Flack. Outer layer similarity in fully rough turbulent boundary layers. *Experiments in Fluids*, 38:328–340, 2005. ISSN 07234864. doi: 10.1007/s00348-004-0903-2.

[74] M. P. Schultz and K. A. Flack. The rough-wall turbulent boundary layer from the hydraulically smooth to the fully rough regime. *Journal of Fluid Mechanics*, 580:381–405, 2007. ISSN 00221120. doi: 10.1017/S0022112007005502.

[75] M. P. Schultz, J. A. Bendick, E. R. Holm, and W. M. Hertel. Economic impact of biofouling on a naval surface ship. *Biofouling*, 27(1):87–98, 2011. doi: 10.1080/08927014.2010.542809. PMID: 21161774.

[76] M. P. Schultz, C. J. Kavanagh, and G. W. Swain. Hydrodynamic forces on barnacles: Implications on detachment from fouling-release surfaces. *Biofouling*, 13:323–335, 1999. ISSN 0892-7014. doi: 10.1080/08927019909378388.

[77] C. R. Shapiro, G. M. Starke, C. Meneveau, and D. F. Gayme. A wake modeling paradigm for wind farm design and control. *Energies*, 12(15): 2956, Aug 2019. doi: 10.3390/en12152956.

[78] J. A. Sillero, J. Jiménez, and R. D. Moser. One-point statistics for turbulent wall-bounded flows at Reynolds numbers up to $\delta^+ \approx 2000$. *Physics of Fluids*, 25:105102, 2013. ISSN 10706631. doi: 10.1063/1.4823831.

[79] H. R. Spivey. Shell morphometry in barnacles: Quantification of shape and shape change in *Balanus*. *Journal of Zoology*, 216(2):265–294, 1988. doi: doi.org/10.1111/j.1469-7998.1988.tb02430.x.

BIBLIOGRAPHY

[80] D. T. Squire, C. Morrill-Winter, N. Hutchins, M. P. Schultz, J. C. Klewicki, and I. Marusic. Comparison of turbulent boundary layers over smooth and rough surfaces up to high Reynolds numbers. *Journal of Fluid Mechanics*, 795:210–240, 2016. doi: 10.1017/jfm.2016.196.

[81] G. M. Starke, C. Meneveau, J. R. King, and D. F. Gayme. The area localized coupled model for analytical mean flow prediction in arbitrary wind farm geometries. arXiv:2009.13666, Oct 2020.

[82] R. J. Stevens and C. Meneveau. Flow structure and turbulence in wind farms. *Annual Review of Fluid Mechanics*, 49(1):311–339, 2017. doi: 10.1146/annurev-fluid-010816-060206.

[83] A. A. Townsend. *The Structure of Turbulent Shear Flow*. Cambridge University Press, Cambridge, 2nd edition, 1976. ISBN 052120710X.

[84] C. Vanderwel and B. Ganapathisubramani. Effects of spanwise spacing on large-scale secondary flows in rough-wall turbulent boundary layers. *Journal of Fluid Mechanics*, 774:R2, 2015. ISSN 0022-1120. doi: 10.1017/jfm.2015.292.

[85] C. Vanderwel, A. Stroh, J. Kriegseis, B. Frohnapfel, and B. Ganapathisubramani. The instantaneous structure of secondary flows in turbulent boundary layers. *Journal of Fluid Mechanics*, 862:845–870, 2019. doi: 10.1017/jfm.2018.955.

[86] R. J. Volino, M. P. Schultz, and K. A. Flack. Turbulence structure in rough- and smooth-wall boundary layers. *Journal of Fluid Mechanics*, 592:263–293, 2007. ISSN 00221120. doi: 10.1017/S0022112007008518.

[87] R. J. Volino, M. P. Schultz, and K. A. Flack. Turbulence structure in boundary layers over periodic two- and three-dimensional roughness. *Journal of Fluid Mechanics*, 676:172–190, 2011. doi: 10.1017/S0022112011000383.

[88] R. J. Volino and M. P. Schultz. Determination of wall shear stress from mean velocity and Reynolds shear stress profiles. *Physical Review Fluids*, 3:034606, Mar 2018. doi: 10.1103/PhysRevFluids.3.034606.

[89] J. M. Walker. The application of wall similarity techniques to determine wall shear velocity in smooth and rough wall turbulent boundary layers. *Journal of Fluids Engineering*, 136(5):051204, 2014. doi: 10.1115/1.4026512.

[90] J. M. Wallace, H. Eckelmann, and R. S. Brodkey. The wall region in turbulent shear flow. *Journal of Fluid Mechanics*, 54(1):39–48, 1972. doi: 10.1017/S0022112072000515.

[91] D. D. Wangsawijaya, R. Baidya, D. Chung, I. Marusic, and N. Hutchins. The effect of spanwise wavelength of surface heterogeneity on turbulent secondary flows. *Journal of Fluid Mechanics*, 894:A7, 2020. doi: 10.1017/jfm.2020.262.

[92] T. Wei, R. Schmidt, and P. McMurtry. Comment on the Clauser chart method for determining the friction velocity. *Experiments in Fluids*, 38(5): 695–699, May 2005. ISSN 1432-1114. doi: 10.1007/s00348-005-0934-3.

[93] D. Willingham, W. Anderson, K. T. Christensen, and J. M. Barros. Turbulent boundary layer flow over transverse aerodynamic roughness transitions: Induced mixing and flow characterization. *Physics of Fluids*, 26(2): 025111, 2014. doi: 10.1063/1.4864105.

[94] W. W. Willmarth and S. S. Lu. Structure of the Reynolds stress near the wall. *Journal of Fluid Mechanics*, 55(1):65–92, 1972. doi: 10.1017/S002211207200165X.

[95] K. Winter. An outline of the techniques available for the measurement of skin friction in turbulent boundary layers. *Progress in Aerospace Sciences*, 18:1–57, 1979. ISSN 0376-0421. doi: doi.org/10.1016/0376-0421(77)90002-1.

[96] K. M. Womack, C. Meneveau, and M. P. Schultz. Comprehensive shear stress analysis of turbulent boundary layer profiles. *Journal of Fluid Mechanics*, 879:360–389, 2019. doi: 10.1017/jfm.2019.673.

[97] Y. Wu and K. T. Christensen. Outer-layer similarity in the presence of a practical rough-wall topography. *Physics of Fluids*, 19(8):085108, 2007. doi: 10.1063/1.2741256.

[98] Y. Wu and K. T. Christensen. Spatial structure of a turbulent boundary layer with irregular surface roughness. *Journal of Fluid Mechanics*, 655: 380–418, 2010. doi: 10.1017/S0022112010000960.

[99] J. Yang and W. Anderson. Numerical study of turbulent channel flow over surfaces with variable spanwise heterogeneities: Topographically-driven secondary flows affect outer-layer similarity of turbulent length scales. *Flow, Turbulence and Combustion*, 100:1–17, 2018. ISSN 15731987. doi: 10.1007/s10494-017-9839-5.

[100] X. I. A. Yang, J. Sadique, R. Mittal, and C. Meneveau. Exponential roughness layer and analytical model for turbulent boundary layer flow over rectangular-prism roughness elements. *Journal of Fluid Mechanics*, 789:127–165, 2016. ISSN 14697645. doi: 10.1017/jfm.2015.687.

[101] X. Zhu, G. V. Iungo, S. Leonardi, and W. Anderson. Parametric study of urban-like topographic statistical moments relevant to *a priori* modelling of bulk aerodynamic parameters. *Boundary-Layer Meteorology*, 162(2): 231–253, Feb 2017. ISSN 1573-1472. doi: 10.1007/s10546-016-0198-x.

Vita

Kristofer Michal Womack was born in Dallas, Texas in 1984. He attended the United States Naval Academy and graduated with a Bachelor of Science degree and a commission in the United States Navy in 2006. As a Naval Academy Trident Scholar, he researched gas turbine engine film cooling. In 2008, he was awarded a Master of Science in Engineering degree from The University of Texas at Austin having completed research on electromagnetic launcher heat transfer. After this initial education, he served as a nuclear submarine officer aboard the USS West Virginia and USS Minnesota. In 2013, having completed sea duty, he began teaching at the United States Naval Academy in the Mechanical Engineering Department. In 2015, at the conclusion of his active duty service, he began doctoral study at Johns Hopkins University. During the course of study, he was recalled to active duty and deployed to east Africa for a year.

He married Bethany in 2009 and they have one daughter, Eleanor. He and his family reside in Annapolis, Maryland.